

2016

High Gain Pattern Reconfigurable Antenna Arrays for Portable and Body-Centric Wireless Applications

Nowrin Hasan Chamok
University of South Carolina

Follow this and additional works at: <http://scholarcommons.sc.edu/etd>

 Part of the [Electrical and Electronics Commons](#)

Recommended Citation

Chamok, N. H. (2016). *High Gain Pattern Reconfigurable Antenna Arrays for Portable and Body-Centric Wireless Applications*. (Doctoral dissertation). Retrieved from <http://scholarcommons.sc.edu/etd/3898>

This Open Access Dissertation is brought to you for free and open access by Scholar Commons. It has been accepted for inclusion in Theses and Dissertations by an authorized administrator of Scholar Commons. For more information, please contact SCHOLARC@mailbox.sc.edu.

HIGH GAIN PATTERN RECONFIGURABLE ANTENNA ARRAYS FOR PORTABLE
AND BODY-CENTRIC WIRELESS APPLICATIONS

by

Nowrin Hasan Chamok

Bachelor of Science
Bangladesh University of Engineering and Technology, 2009

Master of Engineering
University of South Carolina, 2014

Submitted in Partial Fulfillment of the Requirements
for the Degree of Doctor of Philosophy in
Electrical Engineering
College of Engineering and Computing
University of South Carolina
2016

Accepted by:

Mohammad Ali, Major Professor

Guoan Wang, Committee Member

Grigory Simin, Committee Member

Jamil A. Khan, Committee Member

Cheryl L. Addy, Vice Provost and Dean of the Graduate School

© Copyright by Nowrin Hasan Chamok, 2016
All Rights Reserved.

ACKNOWLEDGMENTS

I would like to express my deepest gratitude to my advisor Prof. Mohammad Ali for his continuous support throughout my PhD journey. I feel absolutely privileged to have such a mentor who has always guided me with his knowledge, time, motivation, and philosophical advices. I am also gratefully indebted to my doctoral committee members: Dr. Guoan Wang, Dr. Grigory Simin, and Prof. Jamil A. Khan for their valuable comments and advices to improve this dissertation.

My cordial thanks go to my coworkers in the Microwave Engineering Laboratory: Dr. Md. Rashidul Islam, Dr. Nazmul Alam, Paul Czeresko III, Michael Wright, and Dhruva Paduval, for their selfless assistance and suggestions. I am thankful to our office staff members Nat Paterson, Ashley Burt, David London, Hope Johnson, and Alicia Williams.

I would like to extend my gratitude to my friends and members of Bangladeshi community here, specially to Dr. Fazle Rabbi and Dr. Iftekhar Hossain, who provided me all the supports I needed to cope with a new environment far away from home.

This dissertation would not be possible without the constant encouragement, assistance, and sacrifice of my beloved wife, Firoza Binte Omar. At the time of writing we are expecting our first baby who is already an inspiration to me!

I would like to extend my sincerest appreciation to my parents, Ahsanul Haque and Nowrajish Ara Jahan, and my little sister, Kritiy Haque Charu, who have been constant sources of encouragement throughout my life. I would also like to acknowledge my grandparents and relatives in Bangladesh for their unconditional love and caring.

ABSTRACT

Wireless devices such as smartphones, tablet computers, smartwatches etc. have become ubiquitous. With that, the demand for high speed data has increased tremendously. Designing antennas for such applications is challenging because of limited availability of space, shadowing or blockage from the human body, and signal loss from multipath fading. Conventional broad, fixed beam low gain antennas result in poor reception, faster battery drainage, and low data rate. Compressed footprint high gain pattern reconfigurable antenna arrays can solve these problems which is the focus of this dissertation. Two innovative high gain pattern reconfiguration techniques, the switched beam parasitic array and the varactor controlled series-fed phased array are studied and developed.

First, by taking advantage of the controlled coupling between closely spaced driven and parasitic dipoles, a compressed footprint beam steering array is developed for handheld devices. By optimizing the interelement spacing and the ON/OFF states of the RF switches located at the input of the parasitic dipoles, beam steering in the azimuth plane is achieved. Furthermore, a collinear arrangement of subarrays allows narrow elevation plane beamwidth and gain of up to 11 dBi. By contrast, typical handheld device antennas have about 3 dBi gain and little or no steering ability. System level analysis shows about 59% improvement in signal-to-interference-plus-noise ratio level over traditional omnidirectional antennas.

Second, a high gain switched beam parasitic array is proposed based on fabric materials which can be integrated within the clothing or uniforms of first responders. Material sensitivity analyses considering various conductive and nonconductive fab-

rics are performed. Studies of the array near a multilayered human body phantom reveal that a minimum distance from the body is required for the array to allow beam steering and high gain. For example, with 10 mm spacing from the body -30° to 30° steering is achieved with 10 dBi peak gain which are excellent for high throughput communication.

Third, a novel concept to design ultrathin directional broadband antennas using a nonuniform aperiodic (NUA) metasurface is introduced. By employing a decreasing taper for both the metasurface patch and their interelement spacing, broad impedance and pattern bandwidths are attained. Experimental results show that, with a total thickness of 0.04 free-space wavelength at the lowest frequency of operation, an octave bandwidth can be obtained, which is significantly larger compared with existing designs on uniform mushroom electromagnetic band-gap structures. Based on the NUA metasurface, a thin switched beam (0° , 25° , and 335°) parasitic antenna array is presented which with a thickness of 0.04 wavelength can attain high gain (8.4 dBi) and very high front-to-back ratio.

Finally, to overcome the challenges of wide and overlapping beams with parasitic arrays, and the space constraint and circuit complexity required by phased arrays, a new varactor controlled series-fed phased array is proposed for wearable applications. At the center of the design is a varactor controlled phase shifter, where varactor capacitance is changed by applying different bias voltages which alters the progressive phase between series-fed antenna input currents and allows array pattern to be re-configured. Low return loss, high gain, and beam steering with nulls between two consecutive beams are achieved. It is observed that the choice of substrate and varactors are critical to minimize loss. While the works presented here reflect the 5 GHz frequency band the design and ideas are likely scalable and adaptable for next generation mm-wave systems operating at 28, 38, and 60 GHz.

TABLE OF CONTENTS

ACKNOWLEDGMENTS	iii
ABSTRACT	iv
LIST OF TABLES	ix
LIST OF FIGURES	x
CHAPTER 1 INTRODUCTION	1
1.1 Background and Motivation	1
1.2 Contributions	3
1.3 Outline	6
CHAPTER 2 BEAM STEERING TECHNIQUES	7
2.1 Introduction	7
2.2 Phased Arrays	7
2.3 Switched Beam Parasitic Arrays	9
2.4 Bidirectional Series-fed Phased Arrays	11
CHAPTER 3 HIGH GAIN PATTERN RECONFIGURABLE MIMO ANTENNA ARRAY FOR WIRELESS HANDHELD TERMINALS	15
3.1 Introduction	15
3.2 Array Configuration	18

3.3	Modeling Details and Simulation results	20
3.4	Experimental Results	28
3.5	System Level Performance Analysis	33
CHAPTER 4 HIGH GAIN BEAM STEERING ARRAYS FOR WEARABLE WIRELESS APPLICATIONS		38
4.1	Introduction	38
4.2	Materials for the Proposed Wearable Antenna	39
4.3	Proposed Array Configuration	41
4.4	Simulation Results	42
4.5	Experimental Results	45
CHAPTER 5 THIN SWITCHED BEAM PARASITIC ARRAY ON A NON- UNIFORM APERIODIC (NUA) METASURFACE		47
5.1	Introduction	47
5.2	Fat Strip Dipole Antenna on a Uniform Mushroom Type EBG	51
5.3	Broadband Dipole Antenna on A NUA MetaSurface	55
5.4	Experimental Results	67
5.5	Switched Beam Array on NUA EBG Surface	74
CHAPTER 6 LOW COST BIDIRECTIONAL SERIES-FED PHASED ARRAY FOR BODY-CENTRIC WIRELESS COMMUNICATIONS		80
6.1	Introduction	80
6.2	Proposed Array Configuration	81
6.3	Experimental Results	91

CHAPTER 7 CONCLUSION AND FUTURE WORK	97
7.1 Conclusion	97
7.2 Future Work	100
BIBLIOGRAPHY	103

LIST OF TABLES

Table 3.1	Geometry parameters for array on FR4	26
Table 3.2	Comparison of proposed array with available designs	33
Table 4.1	Dielectric properties of various non-conductive fabric materials. . .	39
Table 4.2	Electrical properties of various conductive fabrics.	40
Table 4.3	Gain variation with different types of fabrics.	44
Table 4.4	Human tissue properties at 5 GHz.	44
Table 5.1	Antenna realized gain on mushroom type EBG	54
Table 5.2	Patch width (in mm) and inter-element spacing (in mm).	58
Table 5.3	Patch width (in mm) and interelement spacing (in mm) for 20% decreasing taper for different number of elements.	58
Table 5.4	Simulated antenna realized gain and directivity on the proposed NUA metasurface	66
Table 6.1	Geometry parameters for the phase shifter (in mm).	87

LIST OF FIGURES

Figure 2.1	Beam steering in a phased array.	8
Figure 2.2	Concept of array multiplication showing a single element pattern, the array factor, and the total array pattern ($d = \lambda/4$, $\beta = 90^\circ$).	9
Figure 2.3	Principle of a two-element Yagi-Uda array.	10
Figure 2.4	Principle of a bidirectional series-fed phased array.	12
Figure 2.5	(a) Varactor controlled phase shifter network for series-fed array and (b) a single phase shifter.	13
Figure 3.1	(a) Conceptual drawings for the application domain of the proposed array: array at the top and side edges of the device, and (b) illustration of the working principle of the proposed pattern reconfigurable array.	17
Figure 3.2	(a) Proposed array geometry, (b) top view, and (c) front view of a single sub-array.	19
Figure 3.3	(a) Effects on S parameter with variation of d , (b) Effects on S parameter with variation of s when all switches are ON.	21
Figure 3.4	Simulated S parameters vs. frequency for array in free-space	23
Figure 3.5	Computed realized gain patterns in free-space in the (a) h-plane (xy) and (b) e-plane (xz).	24
Figure 3.6	Simulated S parameters vs. frequency for array on FR4.	25
Figure 3.7	Computed realized gain patterns on FR4 in the (a) h-plane (xy) and (b) e-plane (xz).	26
Figure 3.8	Configuration of the array with (a) a ground plane and (b) a ground plane and a dielectric housing (not drawn to scale).	27

Figure 3.9	(a) Photo of the built antenna prototype (a) The array components and control circuit, (b) side-view and (c) top view of the setup in anechoic chamber.	29
Figure 3.10	Selected measured S parameters vs. frequency for array on FR4.	30
Figure 3.11	Measured realized gain patterns in the h-plane at (a) 4.8 GHz, (b) 4.9 GHz, (c) 5 GHz, (d) 5.1 GHz, (e) 5.2 GHz, and (f) measured realized gain patterns in the e-plane at 5 GHz.	32
Figure 3.12	Envelope correlation coefficient from measured data.	34
Figure 3.13	Heterogeneous Network structure with PUs, SUs, Secondary Base Stations (SBS) within a primary cell with a Primary Base Station (PBS).	35
Figure 3.14	Comparison of the proposed array with omni-directional antenna and array by Kishor and Hum.	36
Figure 3.15	Mean SINR gain of each SU.	37
Figure 4.1	Array geometry (a) the collinear array, (b) a single sub-array, and (c) top view of the array.	41
Figure 4.2	(a) Simulated $ S_{11} $ vs. frequency for different values of dx and dy , and (b) simulated $ S_{21} $ vs. frequency for different values of s	42
Figure 4.3	Comparison of S parameters vs. frequency for arrays on (a) flat surface and (b) curvature.	43
Figure 4.4	(a) Top view of the array near multilayered body phantom, realized gain patterns for this set up in the (b) azimuth (XY) plane when $h = 5$ mm, (c) azimuth (XY) plane when $h = 10$ mm, and (d) elevation (ZX) plane when $h = 10$ mm.	45
Figure 4.5	Photographs of the set up for loss tangent measurement.	46
Figure 5.1	(a) Fat strip dipole; $W = 110$ mm, $L = 160$ mm and (b) its simulated VSWR.	52
Figure 5.2	(a) A fat dipole antenna on a uniform mushroom-EBG, (b) top view, (c) simulated VSWR response. (d) simulated radiation patterns at 450 MHz, and (e) simulated 3D pattern at 550 MHz.	53

Figure 5.3	Comparison of simulated VSWR for the EBG substrate of FR4 only and a stacked substrate of FR4 and foam.	55
Figure 5.4	Top view of a NUA metasurface with 20% decreasing taper.	58
Figure 5.5	Simulated VSWR responses for a dipole on NUA metasurface with different increasing taper profiles; (a) 2%, (b) 3%, (c) 4%, and (d) 5%.	60
Figure 5.6	Simulated impedance Vs. frequency data for dipole on NUA metasurface with different increasing taper profiles; (a) 2%, (b) 3%, (c) 4%, and (d) 5%.	61
Figure 5.7	Simulated VSWR response of dipole on NUA metasurface with different decreasing taper profiles; (a) 2%, (b) 4%, (c) 10%, (d) 15%, (e) 20%, and (f) 20% tapering with dipole arm length adjusted to 120 mm each.	62
Figure 5.8	Simulated impedance Vs. frequency for dipole on NUA metasurface with different decreasing taper profiles: (a) 2%, (b) 4%, (c) 10%, (d) 15%, (e)20%, (f) 20% tapering with arm length of the dipole adjusted to 120 mm each.	63
Figure 5.9	Simulated impedance Vs. frequency for dipole on NUA metasurfaces with 20% decreasing taper profile. (a) arm length= 156 mm, (b) arm length= 140 mm, (c) arm length= 120 mm, and (d) arm length= 100 mm.	64
Figure 5.10	Simulated realized gain patterns at (a) 319 MHz, (b) 450 MHz, (c) 550 MHz, and (d) 600 MHz.	65
Figure 5.11	Simulated three dimensional realized gain patterns at (a) 319 MHz, (b) 450 MHz, (c) 550 MHz, and (d) 600 MHz.	66
Figure 5.12	VSWR tunability of the broadband antenna on the NUA metasurface; h represents the height of the Antenna from the metasurface.	67
Figure 5.13	Simulated magnetic (H) field distributions at 500 MHz on (a) conventional mushroom EBG surface and (b) NUA metasurface.	68
Figure 5.14	Photographs of (a) the NUA metasurface and (b) metasurface plus dipole antenna. Total surface area 435 mm by 435 mm (17.1 inch by 17.1 inch).	69

Figure 5.15	Simulated and measured VSWR Vs. frequency of dipole on NUA- metasurface.	70
Figure 5.16	Measured normalized E-plane radiation patterns.	71
Figure 5.17	Measured normalized H-plane radiation patterns.	72
Figure 5.18	Measured dipole broadside realized gain vs. frequency on the NUA metasurface.	73
Figure 5.19	Measured dipole patterns at other frequencies (on NUA- metasurface).	74
Figure 5.20	Measured dipole broadside realized gain vs. frequency on the NUA metasurface.	75
Figure 5.21	(a)Top view of a uniform EBG, (b) $ S_{11} $ Vs. frequency, and (c) azimuth plane (xy) pattern.	77
Figure 5.22	(a)Top view of a NUA EBG, (b) $ S_{11} $ Vs. frequency, and (c) azimuth plane (xy) pattern.	78
Figure 6.1	Array geometry (a) the collinear array, (b) a single sub-array, and (c) top view of the array.	81
Figure 6.2	(a) Configuration of a single sub array, (b) dimensions of a single driven dipole, (c) dimensions of a parasitic element, (d) $ S_{11} $ vs. frequency for the single subarray and (e) Realized gain pattern in the yz plane at 5.2 GHz.	83
Figure 6.3	(a) Cross-sectional view (yz plane) of the array, (b) S_{mn} vs. frequency, and (c) realized gain pattern in yz plane at 5.2 GHz for three progressive phases.	84
Figure 6.4	(a) Geometry of a single phase shifter and (b) an unequal length branchline coupler.	86
Figure 6.5	(a) S_{11} vs. frequency, (b) S_{21} vs. frequency, and (c) S_{11} phase vs. frequency for different capacitance values.	87
Figure 6.6	(a) S_{11} vs. frequency when the array was fed from Left side. (b) Realized gain patterns in the yz plane at 5.2 GHz for $C = 0.6$ pF and $C = 2.2$ pF, and (c) Realized gain patterns in the yz plane at 5.2 GHz for $C = 1$ pF.	89

Figure 6.7	Simulation results for array on fabric substrate.	90
Figure 6.8	(a) Photograph of a fabricated phase shifter and (b) phase shifter measurement set up.	91
Figure 6.9	(a) Photograph of a fabricated phase shifter, (b) measured S_{11} , (c) measured S_{21} , and (d) measured S_{21} phase of the shifter.	93
Figure 6.10	Photograph of the (a)top layer of the array with parasitic elements and (b) bottom later of the array containing the phase shifter network, and (c) measured $ S_{11} $ vs. frequency for two different bias voltages.	95

CHAPTER 1

INTRODUCTION

1.1 BACKGROUND AND MOTIVATION

For over four decades there have been tremendous growth and proliferation in wireless communication technology as evident from applications such as voice, video streaming, and online games. Wireless devices such as mobile phones, wireless enabled computers and laptops, and GPS terminals have become ubiquitous. Lately even wearable wireless devices such as smart glasses, smart watches, and smart sensors have begun to being adopted and used. It is estimated that by 2020 around 50 billion devices will be connected with the wireless network [1]. With these growths the demand for higher data rates has also grown significantly. For example, the first generation (1G) communication systems offered about 14 kilobits per second (kbps) of data rate. Present day WiFi, WiMAX and 4th Generation Long Term Evolution (LTE) uses up to 1 Gbps of data rate. Looking beyond, data rates of 10 Gbps are quite feasible.

To meet future demands of ever increasing data rates, innovative new antennas must be designed that can offer higher gain within a very small form factor. This applies to both handheld and wearable wireless applications. That is the focus of this dissertation.

Traditional antennas that are frequently used in handheld devices are fixed beam antennas such as Planar-Inverted F Antennas (PIFAs) [2–4], slots [5–8], patches [9–14], monopoles, [15–19] and loops. [20–22]. Similarly for wearable applications most

commonly used antennas are patch antennas [23–30], PIFAs [31–34], wire antennas [35–43], EBG based antennas [44–51] etc. These antennas are inefficient and hence offer low gain. Furthermore, they lack steering capabilities which are critical for higher capacity. Although diversity [52–59] addresses some of these concerns, it is not an alternative against high-gain beam steering antennas. Even with diversity, devices often suffer from poor reception, which eventually causes the battery to drain very fast. This occurs because when the link margin is weak the transmitter transmits at the highest power level to compensate for that, e.g. 1 bar vs. 5 bars on one’s phone screen.

High gain beam steering arrays offer three important benefits [60]:

(i) Spatial Filtering: Beam steering arrays can suppress the signal coming from undesired directions. It is reported that beam steering arrays can alleviate problems of multipath fading [61] which occurs when signals from a source travel along multiple paths and are incident upon the receiver containing different phases that represent each individual path. Targeting the beam along a single path can greatly reduce the deleterious multipath fading effect.

(ii) Link Margin Enhancement: Arrays due to their high-gain and narrow beamwidth can either increase the communication distance or increase the data rate when the distance is the same.

(iii) Sensitivity Improvement: It has been shown that for an array with n - driven elements, the total received signal power is n^2 times stronger than the signal from a single source, whereas the noise power gets amplified by n . Consequently, the Signal-to-Noise Ratio (SNR) increases n times. This allows for higher data rate as SNR is directly related to the maximum data rate or the data capacity, C of a communication channel by Shannon’s formula,

$$C = B \log_2(1 + \text{SNR}) \tag{1.1}$$

where B is the bandwidth of the channel.

Various techniques exist to design and develop high gain beam steering antenna arrays. These include Phased array, Electronically Steerable Parasitic Array Radiator (ESPAR), Frequency scanning array etc. An overview of the most relevant techniques and how they relate to the proposed dissertation work is given in Chapter 2.

Notwithstanding, the focus of this dissertation is to develop innovative new antenna concepts that are suitable for handheld and wearable wireless device applications. Key metrics are high-gain, steerable beam and smaller form factors.

1.2 CONTRIBUTIONS

In this dissertation, several innovative methods and techniques to design and develop high-gain beam steering antenna arrays are presented that are suitable for handheld and wearable wireless applications.

First, we introduce the idea of a compressed footprint high gain beam steering collinear antenna array for handheld devices [62–64]. To our knowledge, this is the first ever documented compressed footprint high gain beam steering array for a handheld device. The array design is focused on the 5 GHz frequency band; it is understood that translating such a design at higher frequencies will be fairly straightforward. The collinear array is formed using n subarrays. Each subarray containing one driven dipole and two parasitic strip dipoles the latter of which are controlled using integrated RF switches at their centers. For each subarray, when the driven element is excited, currents are induced into the two parasitic elements the magnitude and phase of which depend on the interelement distances, the switch equivalent circuit parameters (ON vs OFF), and the antenna size and geometrical parameters. These parameters have significant effects on both the driving point impedance of the driven element as well as the array factor that determines the beam direction and gain. Analysis efforts are directed to optimize these parameters which allow good driving point impedance, high gain, and beam steering in the azimuthal plane with

a small form factor suitable for handheld devices. High gain is achieved by forming a collinear array which allows significant reduction in the elevation plane beamwidth. A design example on low cost FR4 substrate is presented and its efficacy for practical MIMO application scenario is evaluated on a system level simulation testbed. An experimental prototype of the proposed array is fabricated and tested that consist of PIN diode switches. The fabricated prototype demonstrates performance as expected with some minor discrepancies e.g. irregular nulls in radiation patterns, gain reduction and a minor shift in frequency of operation. The reasons for these discrepancies can be attributed to the effects of long DC bias wires and the use of coaxial baluns.

Second, we investigate and design a high gain beam steering parasitic antenna array for wearable application platforms [65, 66]. This is also a collinear array of n subarrays, where the subarray consists of one driven and two parasitic dipole arrays. The basic principle of operation for this array is similar to the collinear array operation presented above with the exception that the array design must consider wearable materials (conductive and non-conductive fabrics) and the presence of the human body near the antenna array. Also to make it suitable for wearable applications the antenna array must be thin enough for integration into the garment which necessitated the study and design of V-dipoles instead of straight dipoles before. Based on literature reviews several conductive and non-conductive fabric substrates are considered to fabricate the array. Antenna array design is performed considering layers of fabric materials that can be used to build the array. The effects of human body near the antenna array are analyzed.

Third, a new technique to design ultra-thin directional broadband antennas using a Non-Uniform Aperiodic (NUA) metasurface is introduced. Study and design of the NUA metasurface show that by employing a decreasing taper for both the metasurface patch and their interelement spacing broad impedance and pattern bandwidths can be attained [67–69]. Experimental results show that with a total thickness of 0.04

of the free space wavelength (corresponding to the lowest frequency of operation) an octave bandwidth can be attained which is significantly larger compared to existing designs on uniform mushroom EBG (Electromagnetic Band Gap) structures. The concept of NUA EBG surface is then exploited to develop a thin beam switched parasitic array for 2.4 GHz wireless application [70].

Finally, we present a bidirectional series-fed phased array for body-wearable wireless applications. The beam switched parasitic arrays discussed above have a common disadvantage, their azimuthal beamwidth is wide and no reasonable null exists between the different states of the beams. As conventional phased arrays are incompatible in wearable applications for their high cost and complexity we propose to design and develop a varactor controlled series-fed bi-directional phased array antenna. As a viable alternative for wearable applications, series-fed varactor controlled microstrip patch antennas have been proposed for base station application by others [71]. Our objective is to study and design such arrays for wearable applications considering dipole antennas made from textile materials. The use of dipoles makes the array footprint sparse. Moreover, the use of textile materials studied in the work presented above allows us to leverage that knowledge to develop narrow beam high gain beam steering arrays. The series-fed array consists of several dipoles that are excited using pairs of varactors that are connected to branchline couplers. By changing the bias of the varactors the phase shift is controlled which allows beam steering at -25, 25 etc. degrees. It is critical that impedance matching, gain, and pattern steering is achieved simultaneously as the varactor states are changed. Preliminary design optimizations have been performed. Laboratory prototypes of a single phase shifter on FR4 substrate and a series fed array on TMM4 substrate were fabricated and measured for S-parameters by applying different bias voltages. The measurement results show reasonable response with minor aberrations such as slightly high insertion loss and minor shift in frequency of operation, which can be attributed to imperfections

in fabrication process, dielectric loss from substrate loss, and insertion loss due to parasitic series resistance in the varactor diodes.

1.3 OUTLINE

This dissertation is organized as follows. Chapter 2 describes three important beam steering techniques and their applicability for portable and wearable devices. In Chapter 3, the design and development of a high gain beam steering collinear MIMO array for portable handheld devices are presented. Significant performance parameters such as the return loss, isolation, bandwidth, peak beam directions, realized gain, envelope correlation coefficient are investigated. In a realistic communication environment, the system level improvement in Signal-to-Noise ratio due to the antenna array is showed. Chapter 4 presents a thin switched beam parasitic MIMO array for wearable applications. The challenges for designing antenna arrays for body-centric applications are specified. Several characteristics of the array such as return loss, mutual coupling, beam scanning, bandwidth, gain are studied. In Chapter 5, we introduce the concept of a novel broadband non uniform aperiodic EBG metasurface. Based on that design a thin beam switched parasitic array is developed. In Chapter 6, a novel bidirectional series-fed phased array for body-centric wireless application is introduced. Experimental data of S-parameter magnitude and phases for a single phase shifter from the array is presented. Chapter 7 concludes this dissertation with directions for future works.

CHAPTER 2

BEAM STEERING TECHNIQUES

2.1 INTRODUCTION

Beam steering here means electronic steering where certain electronic devices or circuits are used to steer the beam of an array in space. important parameters may include gain, beamwidth, beam direction, Forward to Backward ratio, Side Lobe Level (SLL) etc. In general, beam steering can be obtained using phased arrays, switched beam parasitic arrays, frequency scanning arrays etc. Each of these approaches has its own merits and demerits and are thus suitable for certain classes of applications. For portable and wearable applications, phased arrays and switched beam parasitic arrays are preferred. Basic principles of these two types of arrays are described below.

2.2 PHASED ARRAYS

Phased arrays are widely used to electronically steer the beam of an array in a desired direction while suppressing the beam in other directions. This requires carefully controlling the phase of the individual element of an array.

Consider a linear array consisting of n identical isotropic radiators arranged along the z axis (Fig. 2.1). Each element is excited with a uniform current with magnitude, I_0 and progressive phase shift, β . The spacing between any two consecutive elements is d . The array factor for such an array is given by [72],

$$AF = 1 + e^{j(kd \cos \theta + \beta)} + e^{j2(kd \cos \theta + \beta)} + \dots + e^{j(n-1)(kd \cos \theta + \beta)}. \quad (2.1)$$

The normalized array factor can be written as

$$(AF)_n \cong \frac{\sin \frac{N\psi}{2}}{\frac{N\psi}{2}} \quad (2.2)$$

where $\psi = \frac{2\pi d}{\lambda} \cos \theta + \beta$, with $k = 2\pi/\lambda$.

The maximum occurs at $\psi = 0$ which gives us the angle where the beam peak occurs,

$$\theta_m = \cos^{-1} \frac{\lambda\beta}{2\pi d}. \quad (2.3)$$

This is an important relation that will be referred to in our future discussions. Equation (2.3) clearly defines the beam direction as function of λ , β , and d . For example if $n = 15$, $d = \lambda/2$, and $\beta = 0^\circ$, the array beam is directed along $\theta_m = 90^\circ$, while for $\beta = 90^\circ$ the array beam is directed along $\theta_m = 60^\circ$ (see Fig. 2.1).

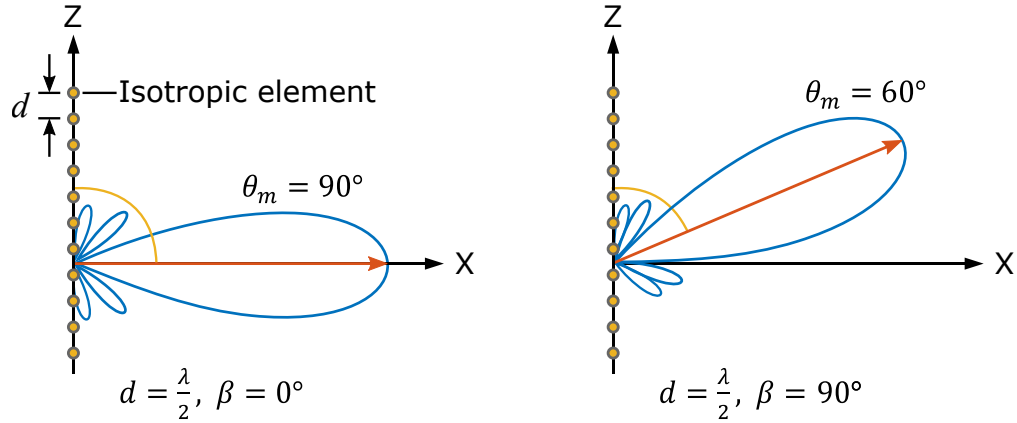


Figure 2.1 Beam steering in a phased array.

With regard to an actual array consisting of real elements such as, dipoles, patches etc. the total field, $\mathbf{E}(\text{total})$ of an array is found by multiplying the array factor (AF) with the pattern of the element as defined in (2.4)

$$\mathbf{E}(\text{total}) = \text{Element Factor} \times \text{Array Factor}. \quad (2.4)$$

For example, the total field pattern of a two element array of infinitesimal dipoles at $d = \lambda/4$ with $\beta = 90^\circ$ is shown in Fig. 2.2.

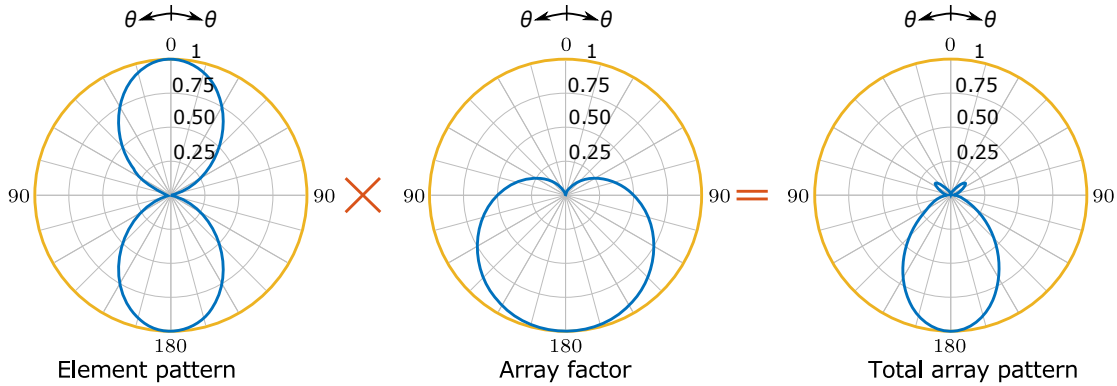


Figure 2.2 Concept of array multiplication showing a single element pattern, the array factor, and the total array pattern ($d = \lambda/4$, $\beta = 90^\circ$).

Although phased arrays provide tremendous opportunities to obtain beam direction, width, SLL, F/B etc. These come at a higher cost and are hence not preferred for small handheld devices. The primary disadvantage of $d = \lambda/2$ precludes applications below 5 GHz. Other disadvantages are that they need costly and complicated phase shifters. For example, cost of a phased array used in collision avoidance radars in high-end vehicles could be between \$1500 - \$3000.

2.3 SWITCHED BEAM PARASITIC ARRAYS

Switched beam parasitic arrays can possibly be best understood from Yagi-Uda arrays [73, 74]. A typical Yagi-Uda consists of a driven dipole, a shorted parasitic dipole that acts as a reflector and multiple shorted parasitic dipoles that act as directors. Such an array generates an endfire beam going in the direction of the directors. The theoretical understanding of a Yagi-Uda array can be based on the concept of reactively controlled directive arrays proposed by Harrington [75] where he used a more general approach and considered the parasitic elements to be terminated using variable reactance. Later Kawakami and Ohira [76] used the same concept to develop Electronically Steered Parasitic Array Radiators (ESPAR).

The principle is illustrated in Fig. 2.3. As seen, two dipole elements are placed

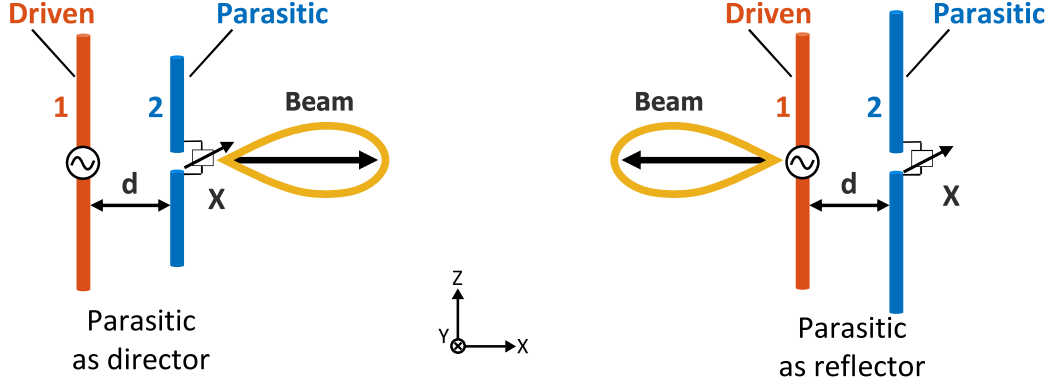


Figure 2.3 Principle of a two-element Yagi-Uda array.

at d distance apart, one is driven and the other is parasitic with a reactance, X at its center. When the driven element is excited, currents are induced in the parasitic element. The currents and voltages of the two elements are related to each other as-

$$\begin{bmatrix} V_1 \\ I_2 X \end{bmatrix} = \begin{bmatrix} Z_{11} & Z_{12} \\ Z_{21} & Z_{22} \end{bmatrix} \begin{bmatrix} I_1 \\ I_2 \end{bmatrix} \quad (2.5)$$

where the subscripts 1 and 2 are for the driven element and the parasitic element, respectively. From (2.5),

$$\frac{I_2}{I_1} = \frac{Z_{21}}{X - Z_{22}}. \quad (2.6)$$

The two dipoles form a linear array which has an array factor of

$$\text{AF}(\phi) = 1 + \frac{I_2}{I_1} e^{jkd \cos \phi} = 1 + \frac{Z_{21}}{X - Z_{22}} e^{jkd \cos \phi}. \quad (2.7)$$

As arranged in Fig. 2.3, if the beam peak occurs at $\phi = 0^\circ$, the parasitic is said to be operating as a director while if the beam peak occurs at $\phi = 180^\circ$, the parasitic element is called a reflector. Equation (2.5)-(2.7) tell us that the parasitic element can operate as a reflector or director depending on the currents. If we take a close look at eqn. (2.7), we can see that at a fixed angle and constant frequency, the array factor depends on the parameters d , X , Z_{12} , and Z_{22} . Again the mutual impedance and the self-impedance depend mainly on the spacing d and the element lengths (and antenna width to some extent, but the sensitivity to length is more prominent than

the width). So, d , X , and antenna lengths are the key variables for this type of array. For dipole elements antenna lengths are often close to a half wavelength, leaving only the spacing (d) and variable reactance (X) as the key contributors.

(a) Effect of d : When d is small, Z_2 and Z_1 are large. This makes the driving point impedance, Z_d small. That results in poor S_{11} when the driven antenna is excited with a 50Ω feed,

$$|S_{11}| = \left| \frac{Z_d - Z_0}{Z_d + Z_0} \right| \quad (2.8)$$

where Z_0 is the characteristic impedance of the feed line (50Ω).

Again, if d is very large, the induced current is very weak and that results in poor array factor.

(b) Implementing X : The variable reactance, X can be implemented using semiconductor devices, such as PIN diodes, Field Effect Transistors, and RF MEMS switches. Varactor diodes can also be used to obtain more precise control over a range of reactances.

Switched beam parasitic arrays occupy less space because $d \ll \lambda$. Also since they do not require external phase shifters the cost is low. These advantages make such array suitable for portable handheld devices and wearable applications. Drawbacks include its relatively wide beamwidth ($\sim 90^\circ$ to $\sim 120^\circ$) and overlapping beams.

2.4 BIDIRECTIONAL SERIES-FED PHASED ARRAYS

To avoid the complexity of traditional phased arrays, a new series-fed phased array was proposed by Ehyaie [60]. It is a bidirectional array. As shown in Fig. 2.4 each of the two terminal ports in the series-fed array can be reconfigured as either a load or an input with the help of a matched Double-Pole-Double-Throw (DPDT) switch. Using this method, the same value of a variable reactance can be used twice (for two

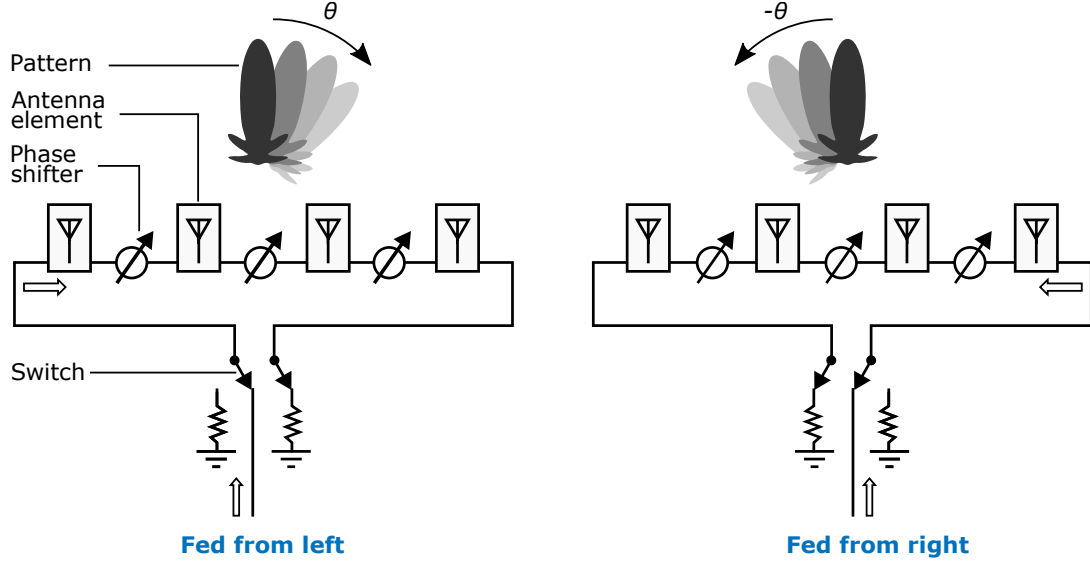


Figure 2.4 Principle of a bidirectional series-fed phased array.

feeding configurations) to steer the beam in two different directions, reducing the phase-shifter complexity by half.

To understand the principle let us rearrange Equation (2.3), assuming the elements are placed along the y axis, and the steering plane being the yz plane,

$$\theta_m = \sin^{-1} \frac{-\lambda\beta}{2\pi d}. \quad (2.9)$$

Let us consider that the array elements are $\lambda/2$ apart. If the phase shifters provide a progressive phase shift ranging from 0 to β , the array peak beam direction can be steered from 0 to $\theta = -\sin^{-1} \frac{\beta}{\pi}$. When the feed direction is switched, the phase shifters provide a progressive phase shift ranging from 0 to $-\beta$ causing the array peak beam direction to steer from 0 to $-\theta = \sin^{-1} \frac{\beta}{\pi}$. Therefore, total of $2 \sin^{-1} \frac{\beta}{\pi}$ steering can be made possible.

The phase shift required can be achieved using varactor diodes. An example is shown in Fig. 2.5a which consists of delay lines, unequal-line length couplers, varactor diodes and grounded radial stubs.

The principle can be understood by analyzing a single phase shifter such as the one shown in Fig. 2.5b. When different bias voltages are applied, varactor capacitances

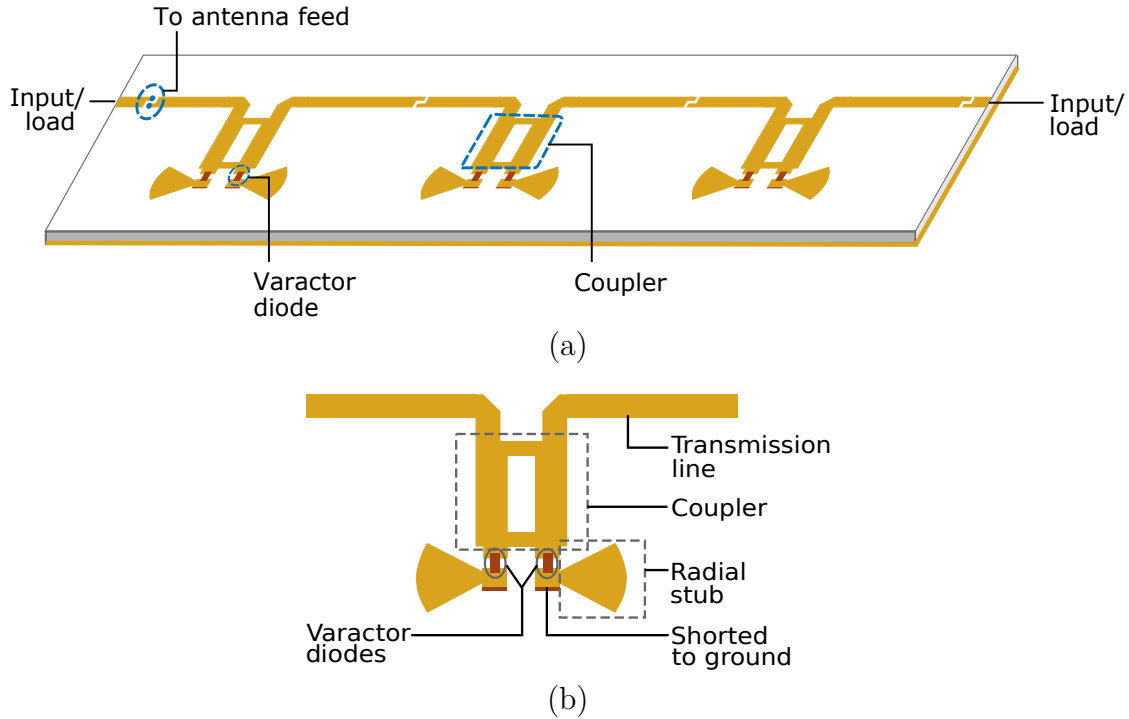


Figure 2.5 (a) Varactor controlled phase shifter network for series-fed array and (b) a single phase shifter.

change accordingly which together with the radial stubs make the load reactances at the bottom two ports of the coupler to change. This changes the phase between the two ports at the top of the coupler that are connected to the transmission line and hence a phase difference is observed between these ports. If two antennas are connected at these two terminals, they will see a phase difference in their input currents and thus a phased array is formed. If multiple such shifters are connected in series, a range of progressive phases can be achieved by varying the voltage. Furthermore, at one time the left terminal of the phase shifter network can be used as the input while keeping the right terminal as the load. Another time it can be done in the opposite way. Thus for the same bias voltage the array beam can point at two different directions.

Although with this method we can exploit most of the benefits of phased arrays (narrow beam, low SLL etc.), unlike traditional phased arrays it does not require

long delay lines with numerous RF switches, which makes it low-cost. This technique can be utilized to develop wearable antenna arrays, where space is available. For high frequency applications such as massive MIMO, mm-wave communications, this technique can be implemented in portable handheld devices also.

CHAPTER 3

HIGH GAIN PATTERN RECONFIGURABLE MIMO

ANTENNA ARRAY FOR WIRELESS HANDHELD

TERMINALS

3.1 INTRODUCTION

Multiple-input multiple-output (MIMO) wireless systems are defined as systems that comprise multiple antenna elements at both the transmitter and receiver ends [77]. MIMO offers important advantages over conventional antennas both in terms of data reliability and data capacity [78]. Considered as one of the most promising candidates of future smart antenna systems, MIMO has already been adopted for IEEE 802.11n [79], worldwide interoperability for microwave access (WiMAX) [80, 81] and long term evolution (LTE) [82].

MIMO for handhelds is an important research area that has the potentials to bring significant advances on antenna and antenna array designs that can be housed within the smaller form factor of a mobile handheld terminal, such as a smartphone or a tablet (iPad). Traditional antennas that are frequently used in handheld devices are fixed beam antennas such as Planar-Inverted F Antennas (PIFAs) [4, 83–86] and monopole antennas [15, 87, 88].

These are inefficient antennas because due to low antenna gain and lack of pattern reconfiguration capability much of the radiated RF power is absorbed by the head or the body resulting in wasted battery power. Furthermore, losses due to multipath

fading result in signal degradation or loss. To circumvent the fading problem diversity [52, 56, 58, 59] have been proposed. Research has shown that only using diversity in a handheld unit signal-to-noise ratio (SNR) improvement of over 8-10 dB can be achieved [56]. This increase in SNR in turn decreases the bit-error-rate [89] resulting in improved spectral efficiency.

MIMO for the handheld [90–92] offers great deal of flexibility especially if it can be combined with high gain and pattern reconfiguration. Other MIMO Antenna examples include [93–95]

The focus of this chapter is to introduce a smaller form factor high gain pattern reconfigurable MIMO antenna array for handheld terminals. The array is designed and developed using the concept of parasitic arrays [96–103] where a driven and one or more closely coupled parasitic elements work in tandem to allow pattern reconfiguration. Since the parasitic elements can be brought very close to the driven antenna element the form factor of the array will be much smaller compared to a traditional phased array making them more suitable for handheld device applications. Although many articles have been published in the literature on parasitic arrays that address dipole or monopole antennas for base stations [97, 98], patch antenna arrays [99, 100], and dipole antenna arrays for wearable wireless applications [31-33], this is the first ever reported detailed work on a high gain pattern reconfigurable collinear parasitic array for the handheld to our knowledge. Very preliminary results of this work were presented at a conference recently [62]. This chapter presents more significant design, analysis, and experimental results and system level simulation results.

The application domain for the proposed array is illustrated in Fig. 3.1a. It is a collinear array of dipole antennas arranged at one edge of a handheld terminal. Although proposed here for handheld terminal the concept is valid for many other applications. The proposed antenna array offers two important features: it can steer the beam in three different directions, and has high gain with narrow e-plane beamwidth.

High gain is achieved by employing the collinear array geometry consisting of multiple ‘sub-arrays’ that allow narrow e-plane beamwidth.

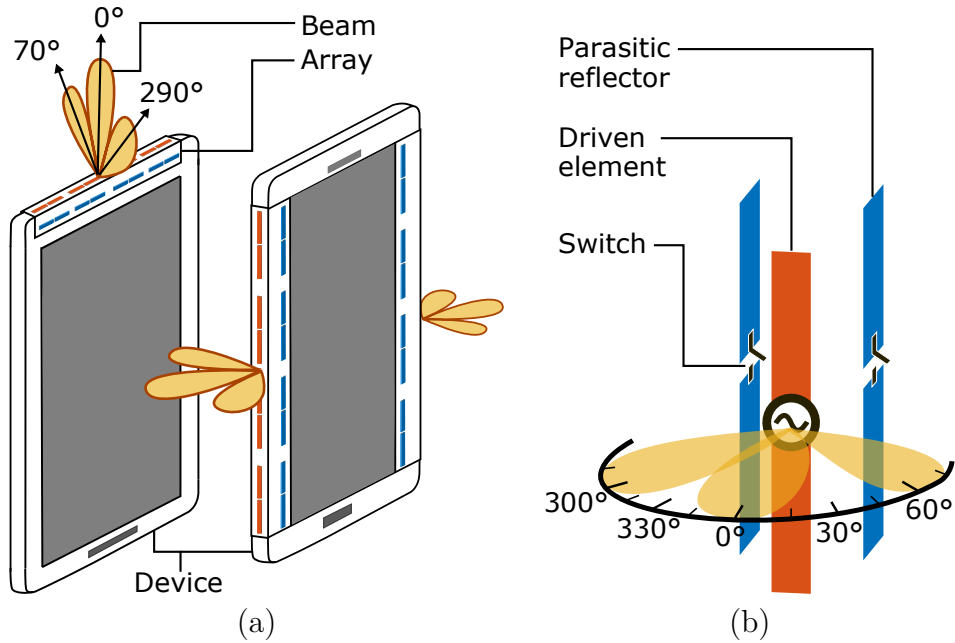


Figure 3.1 (a) Conceptual drawings for the application domain of the proposed array: array at the top and side edges of the device, and (b) illustration of the working principle of the proposed pattern reconfigurable array.

Pattern reconfiguration on the other hand, is achieved with the help of the parasitic array idea which can be explained with the help of one sub-array. Each sub-array contains three dipole elements - one driven and two parasitic (Fig. 3.1b). The parasitic dipoles function as reflectors once activated using RF switches that are located at their centers. This allows array pattern reconfiguration in three different directions for three cases. For example, when switch 1 is ON, the parasitic on the left works as a reflector making the beam point at $\phi = 70^\circ$, when switch 2 is ON, the parasitic on the right works as a reflector making the beam point at $\phi = 290^\circ$, and when both switches 1 and 2 are ON, both parasitics work as reflectors and the beam points at $\phi = 0^\circ$.

The operating frequency considered here is the 5 GHz WLAN band. The rapid

growth and interest in mm wave frequencies and massive MIMO will allow much larger arrays to be implemented using this concept in a variety of application scenarios, e.g. handhelds and base stations, stationary device to device, and chip to chip in computer systems.

The chapter is organized as follows. First, the array configuration parameters are defined. Preliminary simulation studies are performed considering the array implementation in free-space where the effects of parameters, such as, the interelement distances and spacing between subarrays on array input return loss and mutual coupling are investigated. Upon selection of appropriate design parameters, array models with implementation scopes in free-space and on FR4 substrates are developed and analyzed both in terms of S-parameters and radiation patterns. Next, measured S-parameter results and radiation pattern characteristics of the array are presented followed by system level simulations demonstrating performance under communication scenarios.

3.2 ARRAY CONFIGURATION

3.2.1 *The Collinear Array*

The geometry and dimensions of the proposed array are shown in Fig. 3.2a. There are n sub-arrays with the edge to edge separation between two consecutive sub-arrays being s . The length of the array is L . The array axis is the z axis for our analysis with the beam pointing orthogonal to the axis. With increasing n or s , the e-plane beamwidth decreases resulting in increased directivity. The choice of n and s is determined primarily by the space available in terms of the operating wavelength. The parameter, s is also critical as it governs the coupling between two consecutive sub-arrays.

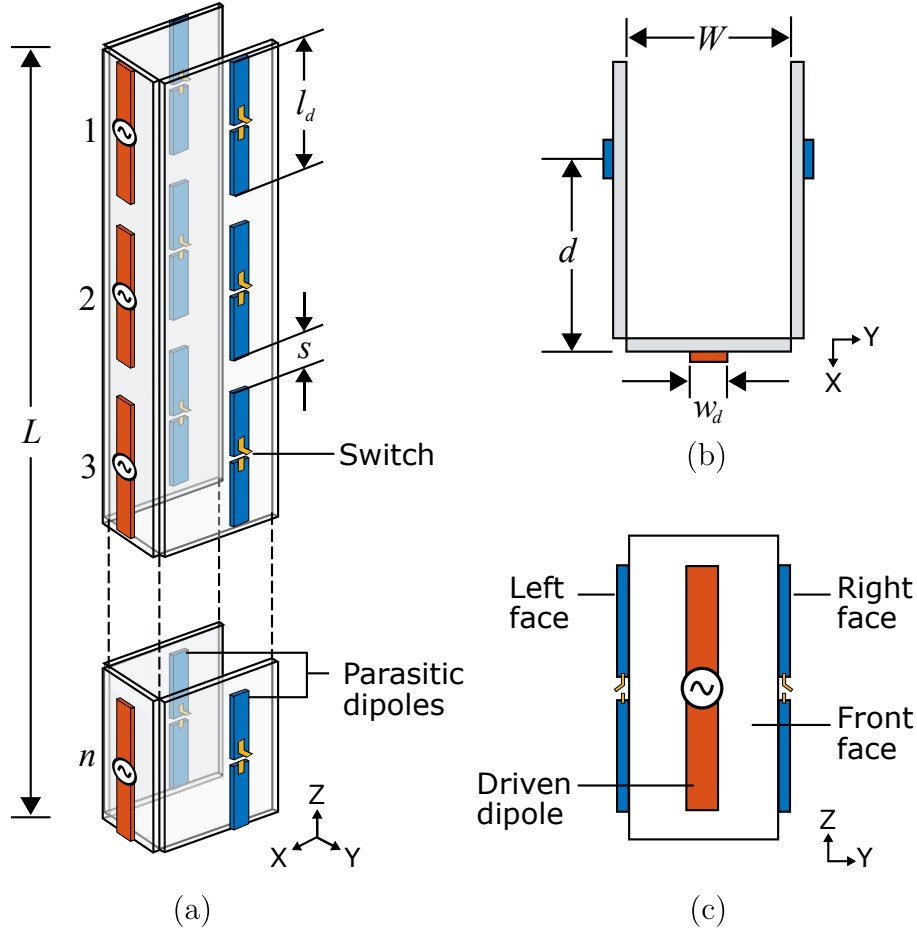


Figure 3.2 (a) Proposed array geometry, (b) top view, and (c) front view of a single sub-array.

3.2.2 The Sub-array

As stated, a single sub-array (Figs. 3.2b and 3.2c) consists of one driven and two parasitic elements. Planar dipole elements on three planar surfaces each approximately half-wavelength long at the operating frequency are considered. The driven element is on the yz plane labeled ‘Front face’ (Fig. 3.2c). The parasitic elements are on two xz planes labeled ‘Left face’ and ‘Right face’, respectively. The left and right faces are separated by distance, W . The distance between the driven and the parasitic is d (Fig. 3.2b). The Front, Left, and Right faces could be considered to constitute the edge of a handheld device.

3.2.3 The Operation of the Sub-array

The driven element is fed using a 50Ω source at its center. The parasitic elements contain RF switches at their centers. Consider the operation of one of the parasitic elements. With the switch OFF each piece of the parasitic is electrically too small to have any effect on the antenna. With the switch ON currents are induced in the parasitic. Following [103], the voltages and currents in the driven and parasitic elements are related by the impedance (Z) matrix given in

$$\begin{bmatrix} V_1 \\ I_2 X \end{bmatrix} = \begin{bmatrix} Z_{11} & Z_{12} \\ Z_{21} & Z_{22} \end{bmatrix} \begin{bmatrix} I_1 \\ I_2 \end{bmatrix} \quad (3.1)$$

and

$$\alpha_{21} = \frac{I_2}{I_1} = \frac{-Z_{21}}{Z_{22} - X} \quad (3.2)$$

where the subscripts 1 and 2 correspond to the driven element and the parasitic element, respectively. The parameters Z_{NN} and the Z_{MN} are the self and mutual impedances in the Z matrix. The excitation voltage in the driven element is V_1 . Clearly Z_{MN} will strongly depend on the distance, d (Fig. 3.2b). Once the Z matrix is calculated Equation (3.2) should be used to determine the magnitude and phase of the coupling coefficient, α_{21} . The phase angle of (3.2) determines if a certain parasitic element will act as a reflector or director; reflector if phase is positive and director if phase is negative [101]. If the parasitic elements are controlled using RF switches or varactor diodes then the X in Equation (3.2) should represent the equivalent circuit to represent its ON and OFF states.

3.3 MODELING DETAILS AND SIMULATION RESULTS

3.3.1 Array in Free Space

Initially the array was designed for operation in free-space in order to obtain a clear understanding of the effects of dielectric loss for the array. Given that material

choices can vary e.g. flexible film, plastics, low loss microwave materials, FR4 etc. Performance data in free-space will serve as a benchmark for comparison. Thus the surfaces on which the dipole elements reside in Fig. 3.2a are considered to be nondielectric ($\epsilon_r = 1.0, \tan \delta = 0$). As mentioned, the design frequency was 5 GHz.

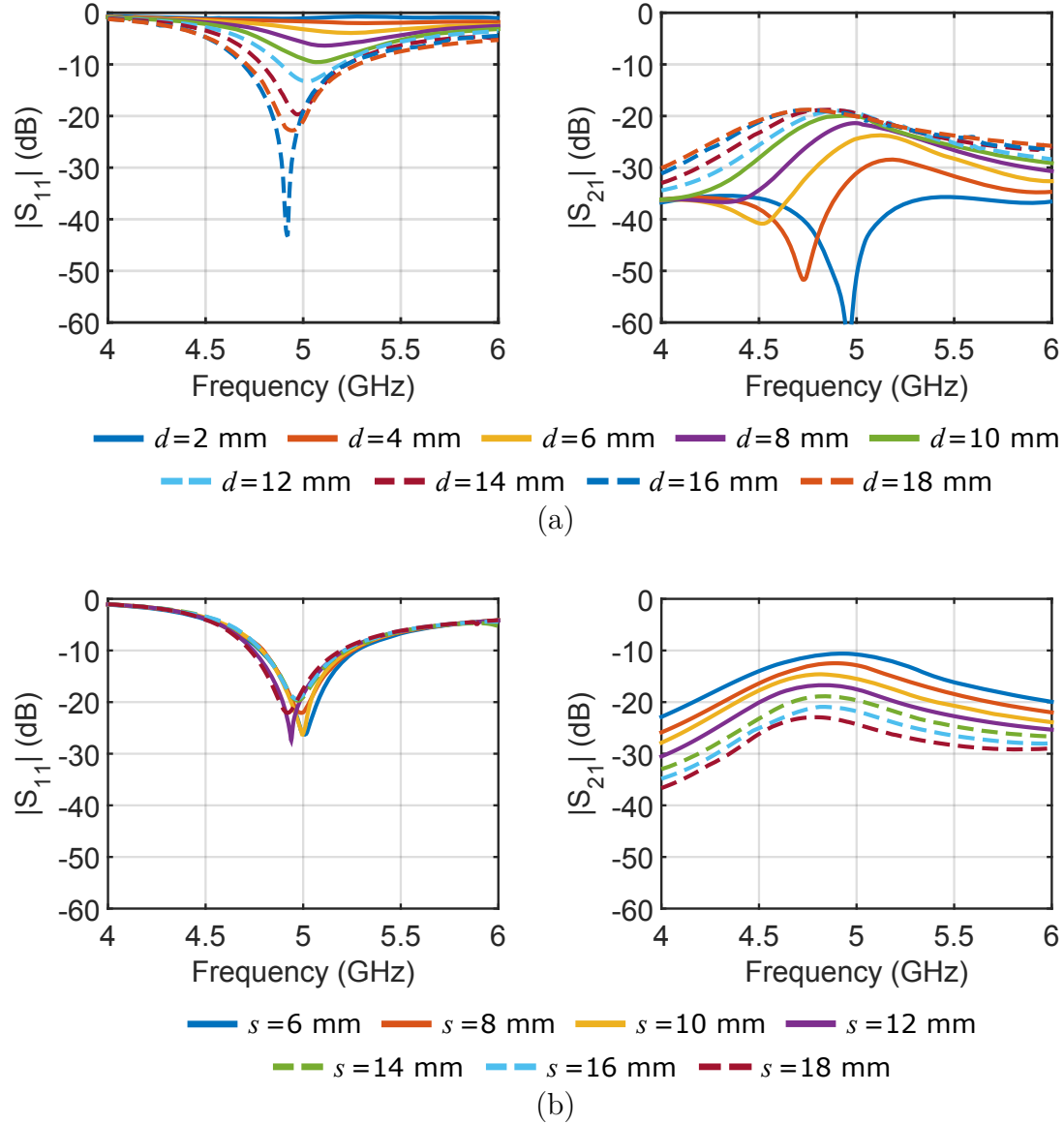


Figure 3.3 (a) Effects on S parameter with variation of d , (b) Effects on S parameter with variation of s when all switches are ON.

The array presented in this chapter consists of 4 subarrays *i.e.*, $n = 4$, hence there are four driven elements and eight parasitic elements. The parasitics are controlled

using discrete RF switches. The choice of $n = 4$ was governed by a device that is about 150 mm long. The length and width of each planar dipole element were 25.4 mm and 2 mm, respectively. The parameter W was selected to be 10 mm considering it to be representative of the thickness of a typical handheld device. Also, we will select the distance, d such that the parasitic elements function as reflectors. Simulations were performed using Ansys HFSS to optimize the array design. To represent the ON state, each switch was modeled using a 5 pF capacitor that represented the equivalent dc blocking capacitance for the switch. To represent the OFF state each switch was modeled using a 0.1 pF capacitor that represented the 8 dB isolation for the switch at this frequency.

Preliminary simulations were performed to select the parameters, d and s such that they allow the parasitics to work as reflectors, provide good impedance matching, and low mutual coupling. For these simulations all switches on the parasitics were modeled as ON. First s was kept constant at 14 mm ($3\lambda/4$ center to center distance between two consecutive sub-arrays) and d was varied. A set of simulations were performed varying d from 2 to 18 mm. These simulation results showed that for $d < 2$ mm, the parasitic elements worked as directors. Since we wanted the parasitic elements to work as reflectors it was concluded that $d > 2$ mm. Important things to consider after this was the $|S_{11}|$ response of each array and the mutual coupling between to consecutive arrays as function of d . Therefore, $|S_{11}|$ for sub-array 1 and the coupling between sub-arrays 1 and 2 were studied as functions of frequency, given that the coupling between two consecutive sub-arrays is the highest. The results presented in Fig. 3.3a show that for $d \geq 12$ mm, $|S_{11}| < -10$ dB and $|S_{21}| < -18$ dB. In order to obtain even better $|S_{21}|$ performance $d = 14$ mm was selected.

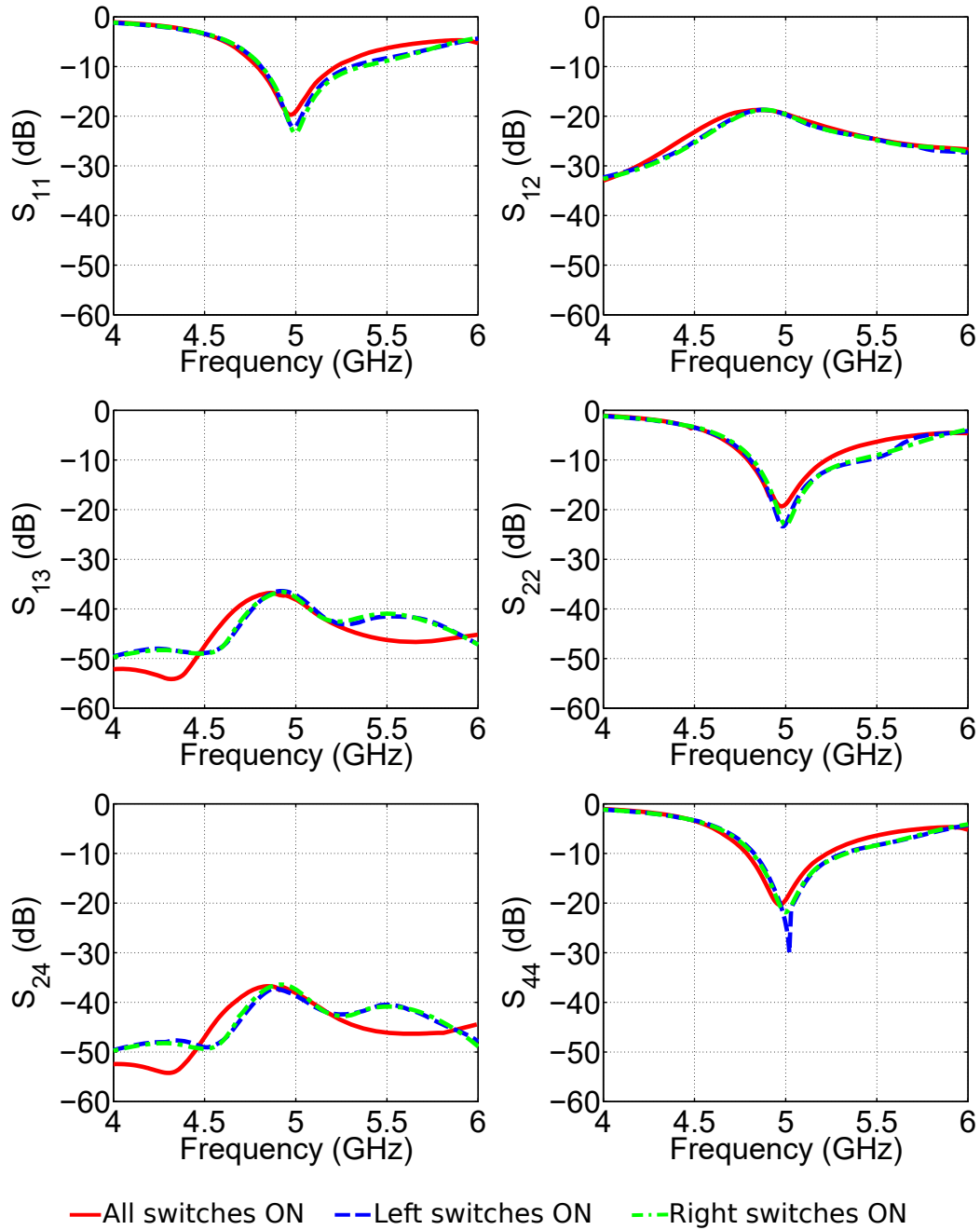


Figure 3.4 Simulated S parameters vs. frequency for array in free-space

Next, while d was fixed at 14 mm s was varied from 6 to 18 mm. As can be seen from Fig. 3.3b, $|S_{11}|$ does not vary much with s , but $|S_{21}|$ does. For the initially assumed value of s (14 mm), the $|S_{21}|$ is around -20 dB at 5 GHz, so this value was kept unchanged.

3.3.2 Computed S Parameters for Array in Free Space

The array with $d = 14$ mm and $s = 14$ mm was then analyzed for three switching cases: Left switches ON, Right switches ON and All switches ON. The simulated S parameters as functions of frequency are shown in Fig. 3.4 The array shows overall satisfactory S parameters: $|S_{nn}|(n = 1, 2, 3, 4) < -15$ dB and $|S_{mn}|(m, n = 1, 2, 3, 4, \text{ and } m \neq n) < -15$ dB.

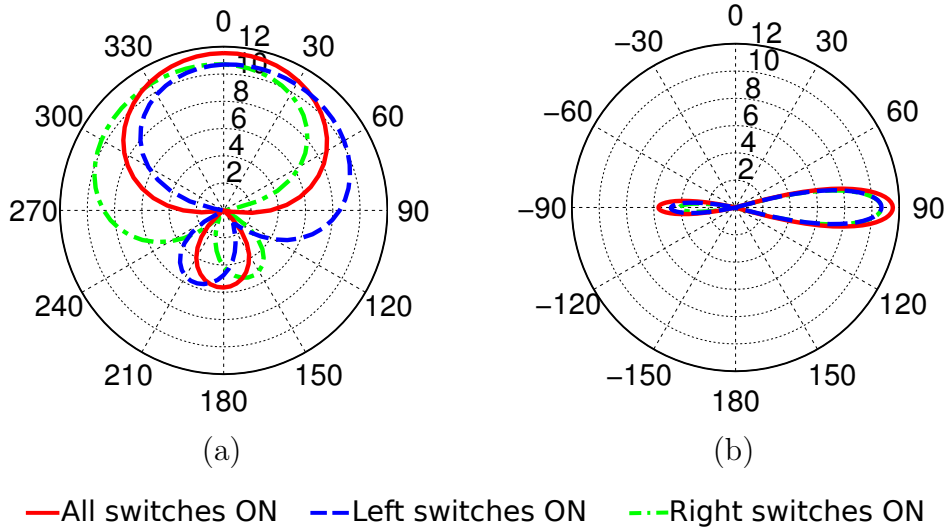


Figure 3.5 Computed realized gain patterns in free-space in the (a) h-plane (xy) and (b) e-plane (xz).

3.3.3 Simulated Radiation Patterns for Array in Free Space

Simulated array realized gain patterns at 5 GHz in the h-plane (xy) and the e-plane (xz) are shown in Figs. 3.5a and 3.5b, respectively. As seen from Fig. 3.5a the pattern has its peak at 0° when All switches are ON, at 30° when the Left switches are ON and at 330° when the Right switches are ON. The e-plane pattern shows a narrow beam (18° half-power beamwidth) as expected. The half-power beamwidth in the h-plane is 120° . The peak gain ranges from 10.7 to 11.7 dBi.

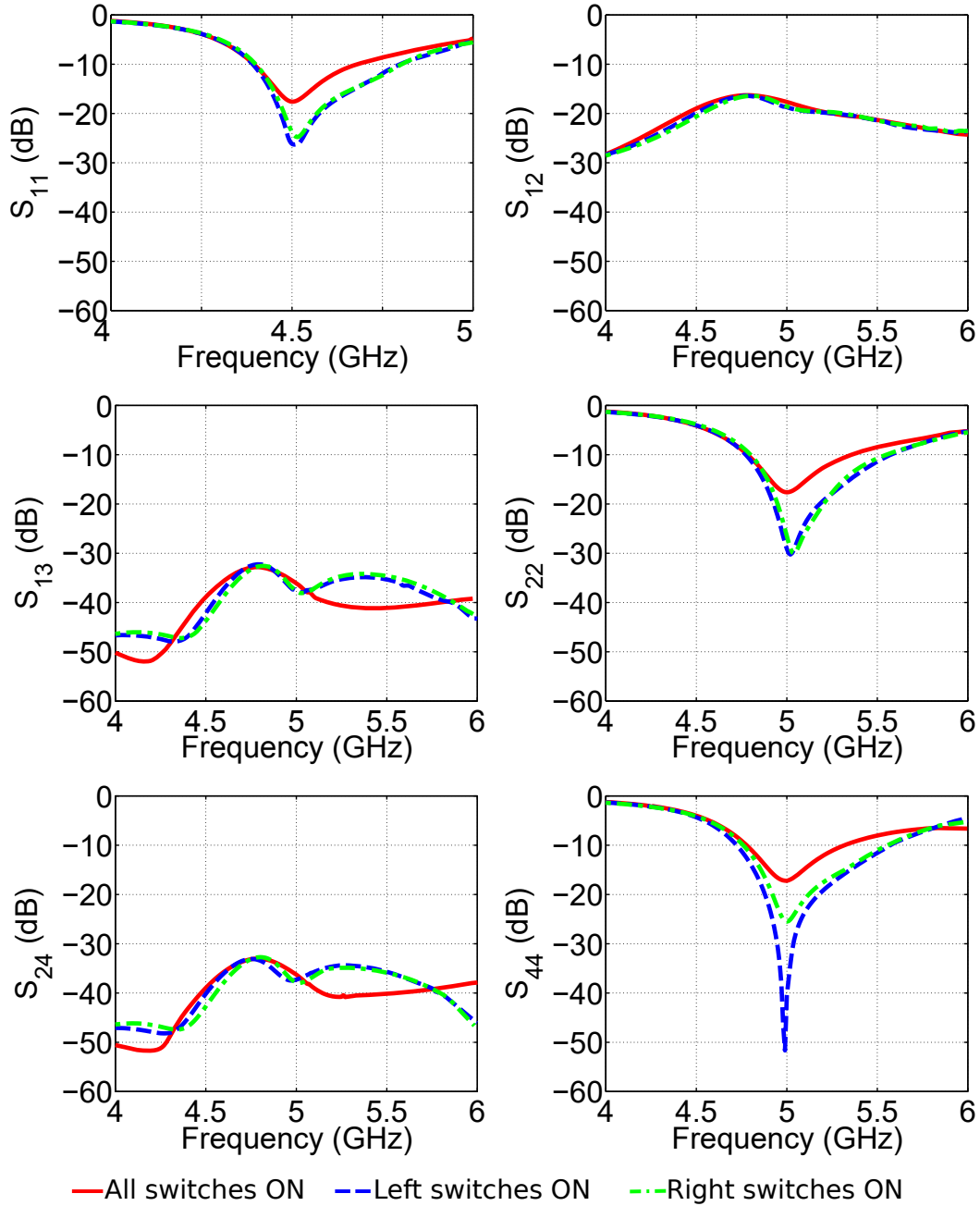


Figure 3.6 Simulated S parameters vs. frequency for array on FR4.

3.3.4 Array on FR4

In order to be able to experimentally fabricate and test an array the free-space design was slightly modified. For the driven and parasitic dipoles on the various faces (Fig. 3.2a) three separate 0.8 mm thick FR4 substrates ($\epsilon_r = 4.5, \tan \delta = 0.02$)

were considered. Dipole lengths were reduced from 25.4 mm to 20.2 mm in order to not change the operating frequency significantly. All other parameters were unchanged. The parameters for the array on FR4 are listed in Table 3.1. The simulated S parameters for this array as functions of frequency are shown in Fig. 3.6. It is apparent that the array operates at 5 GHz with $|S_{nn}|(n = 1, 2, 3, 4) < -15$ dB and $|S_{mn}|(m, n = 1, 2, 3, 4, \text{ and } m \neq n) < -15$ dB.

Table 3.1 Geometry parameters for array on FR4

Parameter	l_d	l_w	L	W	d	s
Value (mm)	20.2	2	122.8	10	14	14

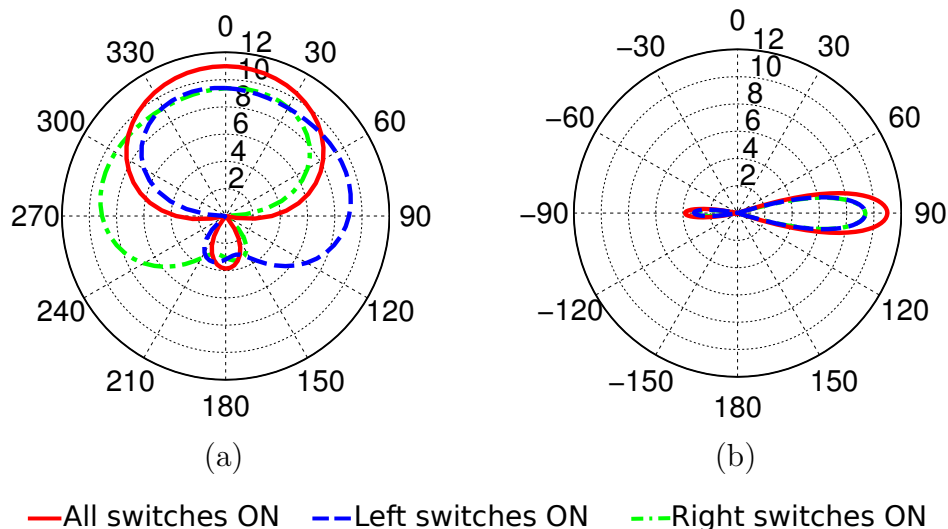


Figure 3.7 Computed realized gain patterns on FR4 in the (a) h-plane (xy) and (b) e-plane (xz).

Simulated realized gain patterns for this array are shown in Figs. 3.7a and 3.7b. Fig. 3.7a shows the h-plane (xy) and Fig. 3.7b shows the e-plane (xz) realized gain patterns of the array at 5 GHz. As seen in Fig. 3.7a, the pattern has its peak at $\phi = 0^\circ$ when All switches are ON, at $\phi = 70^\circ$ when the Left switches are ON and at $\phi = 290^\circ$ when the Right switches are ON. The half power beamwidth in the e-plane is 20° . The half-power beamwidth in the h-plane is 120° . The peak gain ranges from

9.7 to 11 dBi. The degradation in gain (about 0.7 to 1 dB) is due to the $\tan \delta$ of the FR4 material.

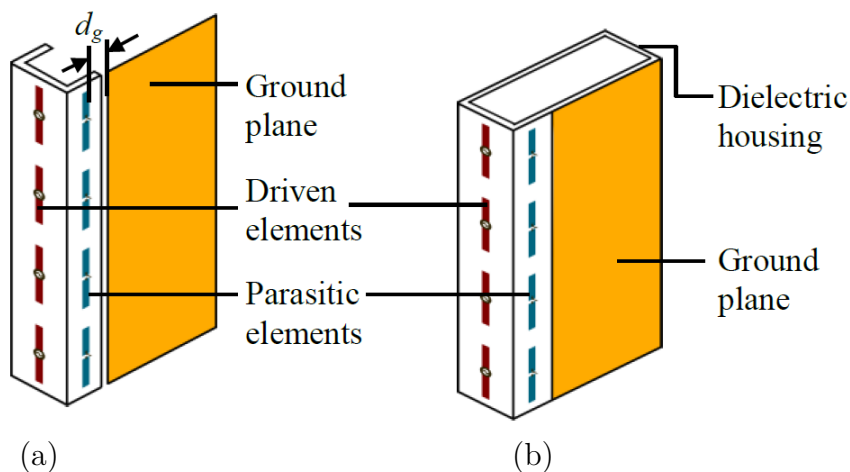


Figure 3.8 Configuration of the array with (a) a ground plane and (b) a ground plane and a dielectric housing (not drawn to scale).

The effect of the presence of a ground plane on antenna performance was studied. A copper ground plane ($150 \times 40 \text{ mm}^2$) was created on the same plane as one of the parasitic antenna planes (Fig. 3.8a). It was placed at a distance, d_g from the corresponding parasitic elements. Two cases were considered, namely, $d_g = 5 \text{ mm}$ and $d_g = 10 \text{ mm}$. For both cases it was found that the effect of adding a ground plane on S parameters was insignificant. On the other hand, a tilt in the radiation patterns was visible. When the ground plane was placed next to the right parasitic elements, the peak beam directions were at $\phi = 75^\circ$, $\phi = 355^\circ$, and $\phi = 240^\circ$ respectively for Left switches ON, All switches ON, and Right switches ON cases. The gain reduced by 1 dB.

The effect of a generic dielectric housing and the ground plane on the antenna was also studied. We considered a $150 \times 70 \times 10 \text{ mm}^3$ dielectric housing ($\epsilon_r = 4.4$ and $\tan \delta = .02$) (Fig. 3.8b). The thickness of the dielectric material for the housing was 0.8 mm and d_g was 10 mm. It was found that the presence of the housing

caused 5% lowering of the antenna center frequency. Nevertheless, the array remained operational at 5 GHz. The radiation patterns and gain were nearly identical to those obtained for the array with a ground plane.

Since the array would most likely be manufactured for placement at the edge of a mobile device other than thin, low dielectric constant, low loss materials can be used, such as plastic for example. It is unlikely that the antenna array will be made from FR4 because the device housing will not be made from FR4. Nevertheless, we think it is safe to assume that such material will be thin, have low dielectric constant and lower loss compared to FR4.

3.4 EXPERIMENTAL RESULTS

A laboratory prototype of the array was fabricated and measured (photographs shown in Fig. 3.9). Each face of the array shown in Fig. 3.2a was photo-etched on a separate 0.8 mm thick FR4 substrate. The dimension of each substrate was $145 \times 9 \times 0.8 \text{ mm}^3$. Each driven dipole was fed using a 2.2 mm diameter semi-rigid 50Ω coaxial cable and a split coax balun made from the same cable (Fig. 3.9). Each parasitic element was controlled using a PIN diode (Skyworks Inc. SMP1345) switch. The switch biasing circuit shown in Fig. 3.9c contains current limiting resistor, $R = 470 \Omega$, inductors, $L = 10 \text{ nH}$ and capacitors, $C = 10 \text{ pF}$. To turn the switches ON 5V dc supply was applied. The application of 5V dc results in 9 mA of forward current allowing the diode ON state resistance to be 1.5Ω . And thus the expected insertion loss is 0.4 dB.

3.4.1 *S-Parameter Measurements and Results*

S parameter measurements were performed for the prototype shown in Fig. 3.9a. Since a 2-port Vector Network Analyzer (VNA) was used at each time when the S-

parameters of two ports were measured the other two ports were terminated using 50Ω loads. The measured S parameter data for the array are shown in Fig. 3.10.

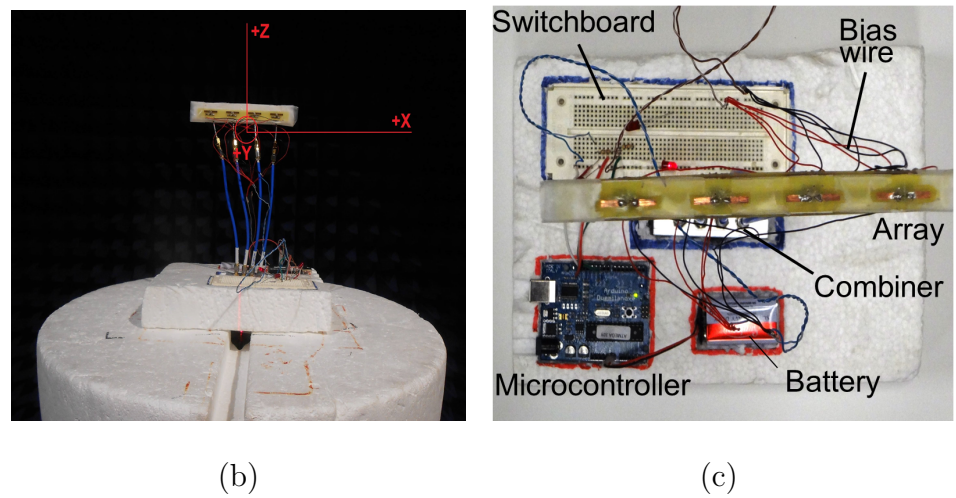
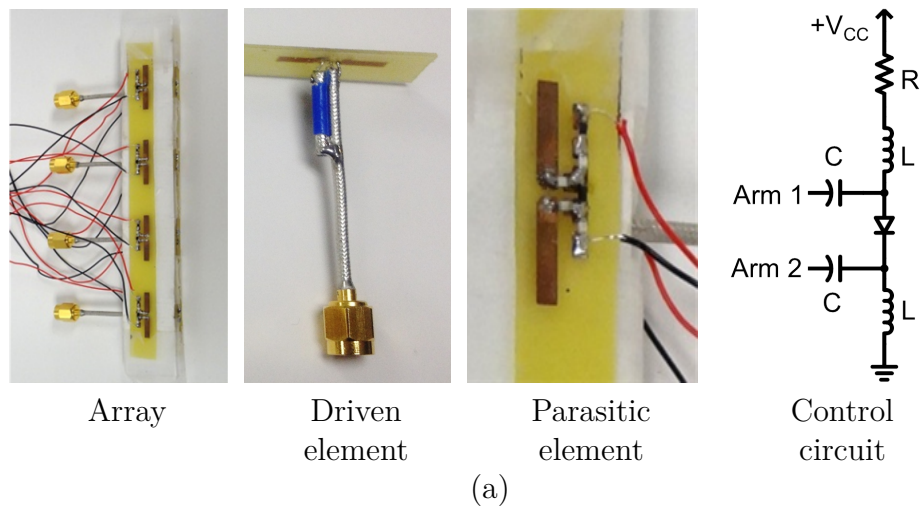


Figure 3.9 (a) Photo of the built antenna prototype (a) The array components and control circuit, (b) side-view and (c) top view of the setup in anechoic chamber.

The measured results show that the array operates in the frequency range of 4.4 to 5.1 GHz (As $|S_{11}| \leq -10$ dB and $|S_{21}| \leq -18$ dB). Comparing the measured results of 3.10 to the simulated results of Fig. 3.6 it can be seen that the operating frequency for the measured is slightly lower than the simulated. The decrease in frequency is probably due to a combined effect of imperfections in the fabrication process, non-

ideality of FR4 material, and the adverse effect of long bias wires which were used to supply dc voltage to the switch control circuit.

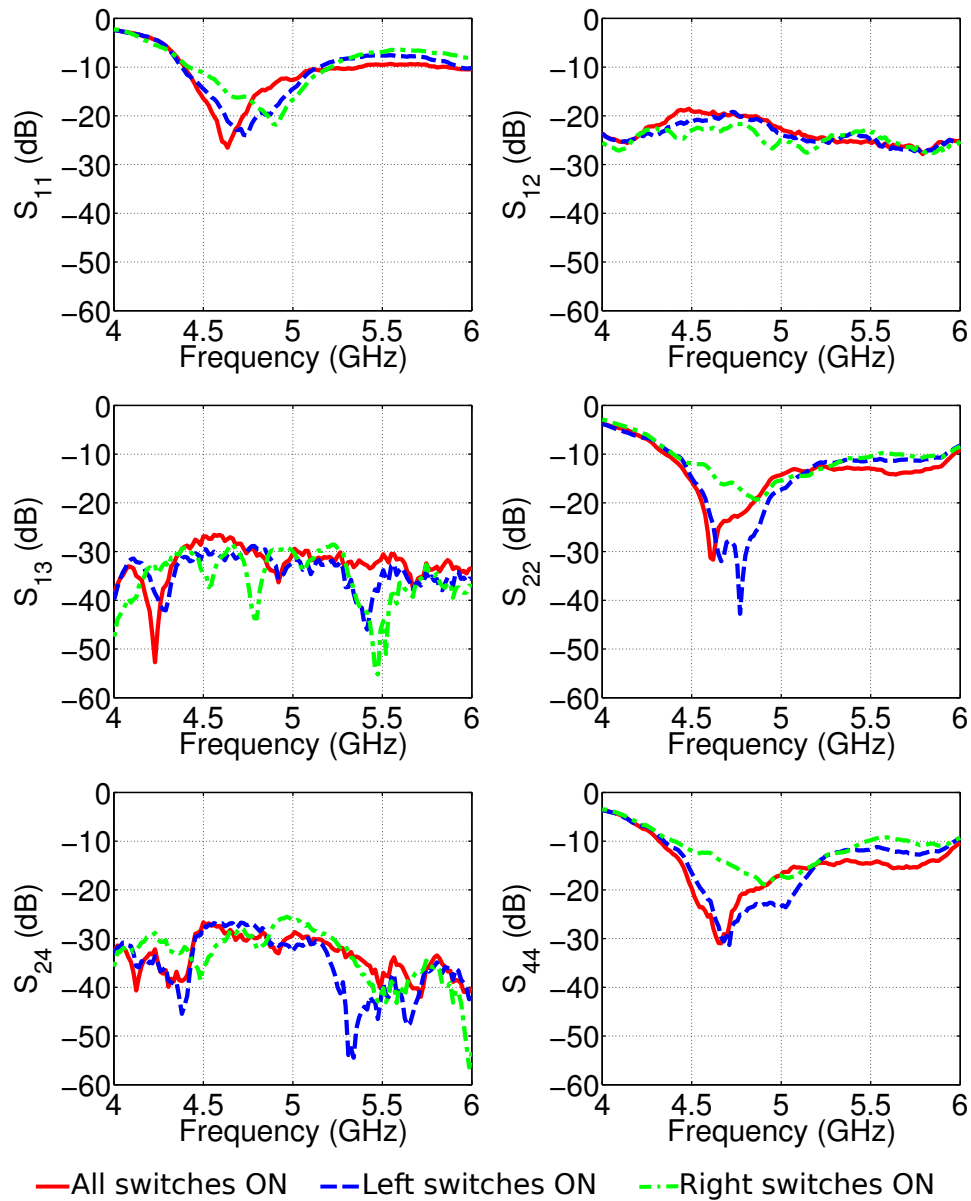


Figure 3.10 Selected measured S parameters vs. frequency for array on FR4.

3.4.2 Gain and Pattern Measurement Results

The array gain and radiation patterns were measured in a SATIMO anechoic chamber. The setup is shown in Fig. 3.9b. As shown in Figs. 3.9a and 3.9b each driven dipole

is first connected to a split-coax balun and a coaxial cable. The balun resides between two pieces of foam, each 5 mm thick. This coaxial cable then connects to another 152.4 mm long coaxial cable via a female-female SMA adapter. This cable assembly along with three similar assemblies from the other three driven dipoles are then connected to the 4 output ports of a 4-to-1 combiner (Minicircuits ZN4PD-642W-S+). The input of the combiner is connected to the measurement cable of the chamber.

A microcontroller (Arduino Duemilanova) fed by a 9V battery was used to control the bias states of all eight switches. Sixteen pieces of 381 mm long dc bias wires were connected from the parasitic elements to the microcontroller circuit board. The assembly is shown in Fig. 3.9c.

The cables, connectors, adapters and the combiner were measured to quantify the combined insertion loss for the pattern and gain measurement setup that preceded the array elements. The insertion loss was between 1.1-1.3 dB. The insertion loss was added to the measured gain data from the anechoic chamber.

Measured realized gain patterns at several frequencies within the operating frequency band are shown in Fig. 3.11. Array pattern reconfiguration in the h-plane is apparent from Figs. 3.11a-3.11e. For all three cases, namely All switches ON, Left switches On, and Right switches ON measured peak gain is between 8-10 dBi. Measured antenna efficiency is about 80 %. The individual patterns for the three cases provide a near hemispherical coverage with an average array gain of 8 dBi. The Half-Power Beam Width (HPBW) for the All ON case is wider than the HPBW for the other cases. Average HPBW is about 100°. The E-plane patterns for one frequency shown in Fig. 3.11f show that the beams are narrower as expected with the HPBW of about 25°. Comparing the measured patterns of Fig. 3.11 with the simulated patterns shown in Fig. 3.7 there are signs of reflections and distortions in the measured patterns. These are more pronounced for the case called the Right switches ON. Ideally the h-plane patterns should be directed at 0°, 70°, and 290° for

the All ON, Left ON, and Right ON cases, respectively.

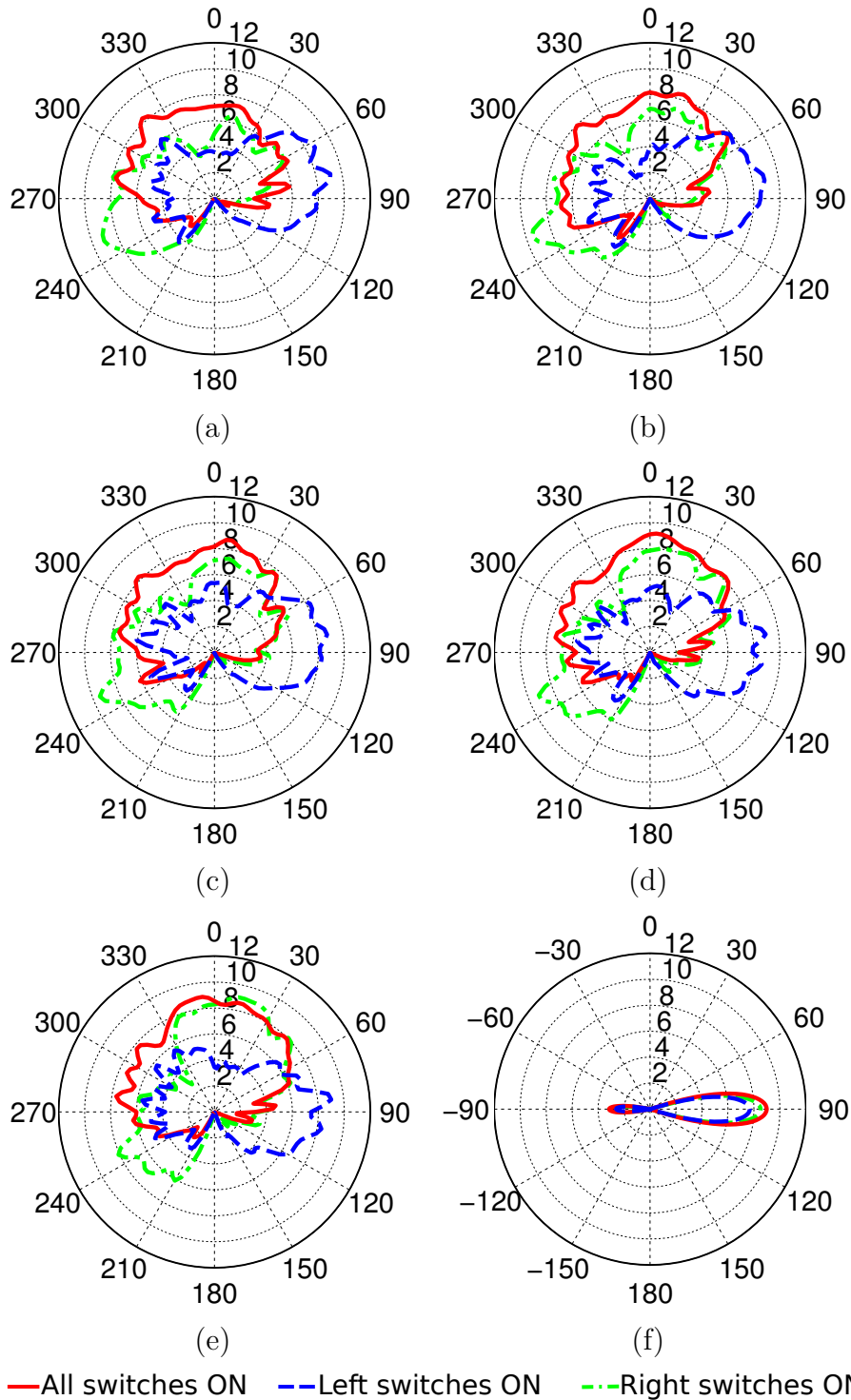


Figure 3.11 Measured realized gain patterns in the h-plane at (a) 4.8 GHz, (b) 4.9 GHz, (c) 5 GHz, (d) 5.1 GHz, (e) 5.2 GHz, and (f) measured realized gain patterns in the e-plane at 5 GHz.

The differences between the simulated and measured patterns can be attributed to the presence of the four coaxial cables and split coax baluns, the 16 dc bias wires, and also possibly the power combiner that were not present in the simulation models. It is expected that if lumped element chip baluns and dc bias traces made from high resistance ($>500 \Omega/\text{square}$) lines [104] are implemented much of the reflections and distortions in the pattern will disappear. The simulation models did not include the cables and the wires which are likely the cause for the discrepancies.

The performance of the proposed array is compared with some available designs as shown in Table 3.2.

Table 3.2 Comparison of proposed array with available designs

Publication	Element no.	Meas. gain (dBi)	Freq. of operation (GHz)	Size (mm ³)	Scan angles (degree)
Qin <i>et al.</i> [91]	2	6	5.2	$30 \times 30 \times 30.2$	Not well-defined
Kishor and Hum [90]	4	2.5	2.3	$90 \times 30 \times 5$	30, -30
Rhee <i>et al.</i> [92]	4	5.4	5.2	$120 \times 40 \times 6$	30, -30
Proposed array	4	10	5	$123 \times 10 \times 14$	70, 0, 290

3.5 SYSTEM LEVEL PERFORMANCE ANALYSIS

3.5.1 Envelope Correlation Coefficient

Envelope Correlation Coefficient (ECC) is a metric often used for MIMO antennas that measures the correlation between two antennas. For MIMO applications with N antennas, the ECC between the i -th and the j -th elements is given by [105]

$$\rho_e(i, j, N) = \frac{\left| \sum_{n=1}^N S_{i,n}^* S_{n,j} \right|^2}{\prod_{k=i,j} (1 - \sum_{n=1}^N S_{k,n}^* S_{n,k})} . \quad (3.3)$$

Fig. 3.12 shows the ECC for the array that was computed using the measured S-parameter data presented in Fig. 3.10. As seen, $ECC < 0.01$ which is excellent for a MIMO array. This should be stated that for accurate ECC calculation far field patterns should be used instead of S parameters as the latter method assumes lossless antennas [106]. However for efficient antennas it can provide good approximation for ECC [107].

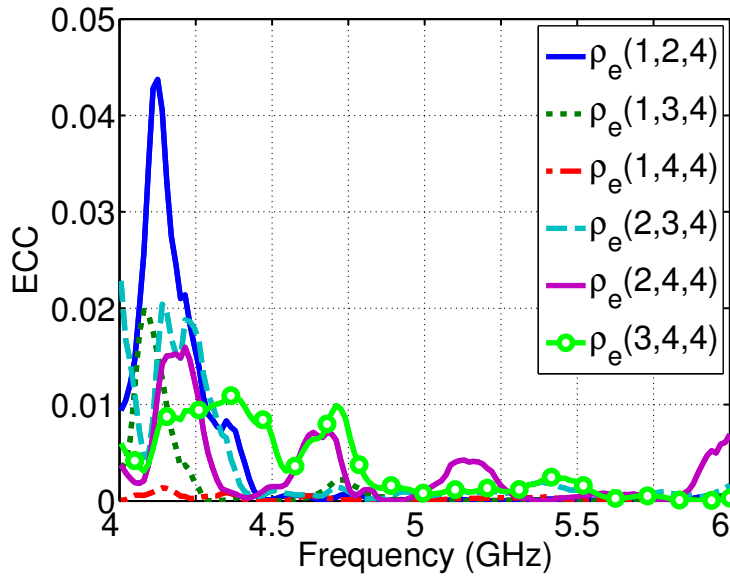


Figure 3.12 Envelope correlation coefficient from measured data.

3.5.2 Signal-to-Interference-plus-Noise Ratio (SINR) Performance

Finally, a system level analysis is performed to understand the performance characteristics of the proposed array compared to two other antennas: a 5 dBi gain omni-directional antenna and a MIMO array proposed by Kishor and Hum which has two states [90]. Resource allocation study is carried out among the secondary users (SUs) within the game theoretical framework in the heterogeneous networks which consist of 16 primary users (PUs), 20 secondary base stations with 2 SUs in each under one primary network (Fig. 3.13).

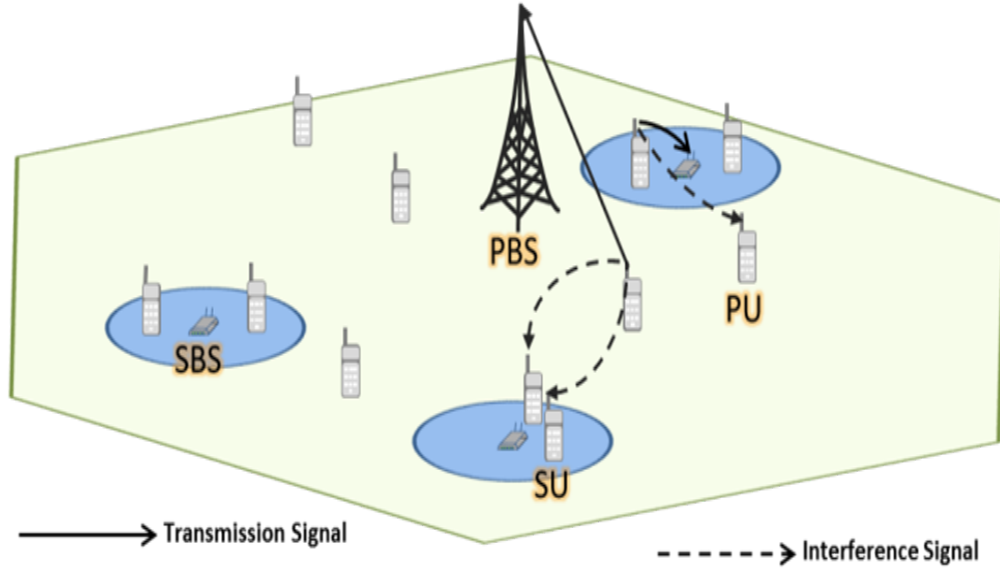


Figure 3.13 Heterogeneous Network structure with PUs, SUs, Secondary Base Stations (SBS) within a primary cell with a Primary Base Station (PBS).

We consider that the number of available resources is 256 under the orthogonal frequency division multiple accessing scheme, and it is assumed that all resources are allocated by PUs. Likewise, the SUs in each secondary network are considered to use all resources. Since the aim is to decrease the interference induced on the PUs, only SUs are assumed to use the array by Kishor and Hum or the proposed array, i.e., PUs are equipped with only omni-directional antenna. SINR of a SU u can be expressed as follows,

$$\text{SINR}_u = \sum_{f \in F} \frac{p_u g_{uf} \beta_{uf}}{\sum_{v \in U, v \neq u} p_v g_{vf} \beta_{vf} + \sum_{b \in \beta} p_b g_{bf} \beta_{bf} + \omega_0} \quad (3.4)$$

where $f = 1, 2, \dots, F$ is the subcarrier index, U and B show the total number of SUs and PUs, respectively, v is the interfering SU index, $u, v \in U$, b is the PU index, p_u denotes the transmit power for user u and parameter $\beta_{u,f}$ is the indicator function for the f th subcarrier. If SU u uses the f th subcarrier, $\beta_{u,f} = 1$, otherwise $\beta_{u,f} = 0$. ω_0 is the additive white Gaussian noise.

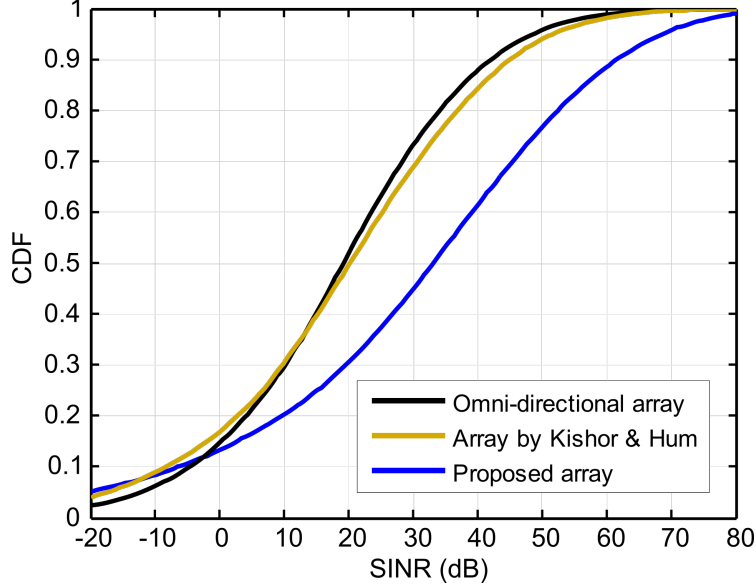


Figure 3.14 Comparison of the proposed array with omni-directional antenna and array by Kishor and Hum.

Fig. 3.14 shows the performance results of the proposed array, omni-directional antenna and PIFA in terms of SINR. As seen from the figure, proposed array outperforms the standard antennas. While 50% of the SINR values are only below 19 dB and 20 dB respectively for the omni-directional antenna and the Kishor and Hum antenna, respectively 50% of the SINR values are below 33 dB for our proposed array. In other words, the gain in mean SINR of the Kishor and Hum antenna over the omnidirectional antenna is 2.5%. The same for the proposed antenna over an omnidirectional antenna is 59%. This indicates that the SUs can achieve higher SINR values with proposed array. This result can also be confirmed from Fig. 3.15 which shows the mean SINR gain obtained in each SU. As shown in Fig. 3.15, almost every SU achieves higher gain with proposed array. System level results indicate that the proposed array is a strong candidate for the user devices in heterogeneous networks. This result can also be proved in Fig. 3.15 which shows the mean SINR gain obtained in each SU. As shown in Fig. 3.15, almost every SU achieves higher gain with

proposed array. System level results indicate that the proposed array is a strong candidate for the user devices in heterogeneous networks.

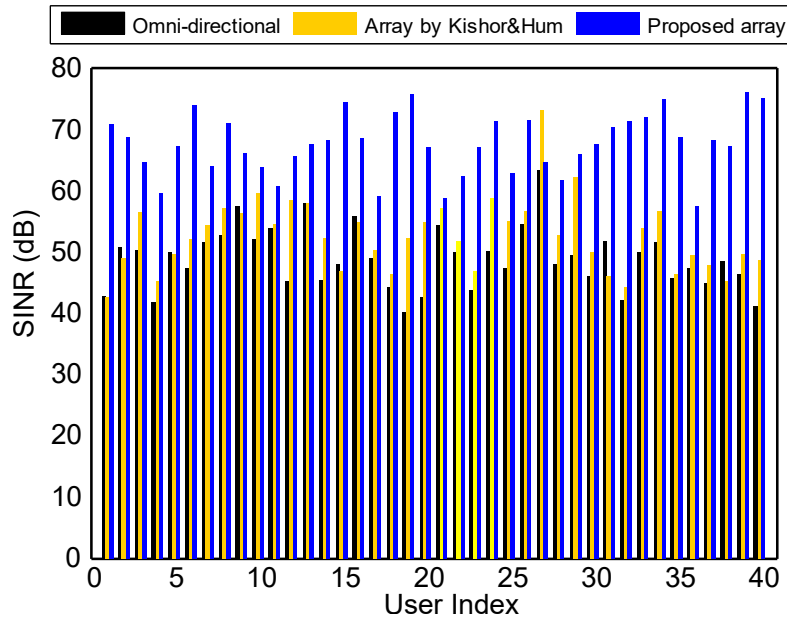


Figure 3.15 Mean SINR gain of each SU.

CHAPTER 4

HIGH GAIN BEAM STEERING ARRAYS FOR WEARABLE WIRELESS APPLICATIONS

4.1 INTRODUCTION

Body-centric wireless communication is a rapidly growing field which can be classified into three types: Off-body, on-body, and in-body communication [108]. If only one antenna in the communication link remains on body and rest of the link is outside the body (in the surrounding place) it is called off-body communication. This sets up the communication between local base stations and the antenna on body, which can be a wearable or textile antenna. If all antennas are on the surface of the body and hence the communication link is also on the surface of the body it is called the on-body domain. And if most of the antennas or sensors are implanted inside the body it is referred to be the in-body domain. This includes the implantable chips and sensors. In this chapter we will focus on off-body communications.

Many fixed beam antennas have been proposed for off-body communication which suffer from gain degradation in multipath rich environment causing low data rate and low reliability[108]. It has been shown that pattern reconfigurable MIMO arrays can perform better in these situations [22]. As mentioned earlier, pattern reconfiguration can be achieved using phased arrays but that will make the array too large and costly to implement for wearable communications. Parasitic arrays are a good alternative for low cost smaller footprint applications.

Recently, in our group, we introduced the concept of high-gain compressed foot-

print switched parasitic beam steering array for 0.9 GHz, 2.45 GHz and 5 GHz wearable application [101–103]. The 0.9 GHz and 2.45 GHz array each consists of a single subarray with one driven element and thus has low gain. The 5 GHz array is a high gain collinear array consisting of multiple driven and parasitic elements but it uses a thick foam substrate which is impractical for wearable applications.

In this chapter we present the design of a thin high-gain beam steering collinear antenna array based on realistic fabric materials which can be integrated within the clothing or uniform of a person. The robustness of the design is demonstrated with material sensitivity analysis and performance studies on a curved surface and near a multilayered body phantom. Loss tangent measurement data for fabric substrate is presented.

4.2 MATERIALS FOR THE PROPOSED WEARABLE ANTENNA

Properly selecting non-conductive fabric substrates is important while designing and developing wearable antenna arrays. RF properties that are highly desired are low dielectric constant, ϵ_r and low loss tangent, $\tan \delta$. Low dielectric constant allows wider bandwidth while low $\tan \delta$ allows high gain. Mechanical/structural properties that are greatly desired are flexibility/malleability, homogeneity, and very low tendency to absorb moisture.

Table 4.1 Dielectric properties of various non-conductive fabric materials.

Nonconductive Fabric	ϵ_r	$\tan \delta$
Cordura	1.90	0.0098
Cotton	1.60	0.0400
100 % polyester	1.90	0.0045
Quartzel fabric	1.95	0.0004
Lycra	1.50	0.0093

In general, the dielectric properties of a textile material depend on the frequency,

temperature, surface roughness, moisture content, purity and homogeneity of the material [109]. The fabric materials are generally anisotropic because of the weaving pattern of the fibers or yarns. Non-conductive fabrics are also porous materials with ϵ_r varying from 1.2 to 2. The ϵ_r and $\tan \delta$ of various fabrics are shown in Table 4.1 [110].

Moisture content in fabric materials is a key contributor in ϵ_r change. Typically the higher the moisture content the higher is the ϵ_r . The sensitivity of fabrics to moisture is characterized using the term ‘regain’ [109], which is defined as

$$\text{Regain} = \frac{\text{Mass of water absorbed}}{\text{Mass of dry specimen}} \times 100\%. \quad (4.1)$$

Regain is related to relative humidity (RH). It is reported that at 65% RH, wool fiber, cotton and polyester might present a regain of 14.5%, 7.5% and 0.2% respectively, which shows that Polyester is much less sensitive to humidity [109].

Similarly to fabricate antennas that can be formed or shaped to go with body contour conductive fabrics can be used. Various conductive fabrics Flectron [111], ShieldIt, Copper taffeta, Nickel Copper Ripstop, Ripstop Silver [112] etc. have been reported in the literature. Key properties include electric surface resistivity, ρ_s which is related to conductivity, σ , and fabric thickness, t

$$\sigma = \frac{1}{\rho_s t}. \quad (4.2)$$

Table 4.2 shows the ρ_s , t , and σ of some commonly used conductive fabrics.

Table 4.2 Electrical properties of various conductive fabrics.

Conductive Fabric	Surface resistivity, ρ_s ($\Omega/\text{Sq.}$)	Thickness, t (mm)	Conductivity, σ (S/m)
Flectron	0.07	0.2	7.14×10^4
ShieldIt	0.50	0.15	1.33×10^4
Copper Taffeta	0.05	0.08	6.67×10^5
Nickel Copper Ripstop	0.03	0.08	4.16×10^5
Ripstop Silver	0.25	0.05	8×10^4

Typically woven conductive fabrics are preferable because they minimize RF loss.

4.3 PROPOSED ARRAY CONFIGURATION

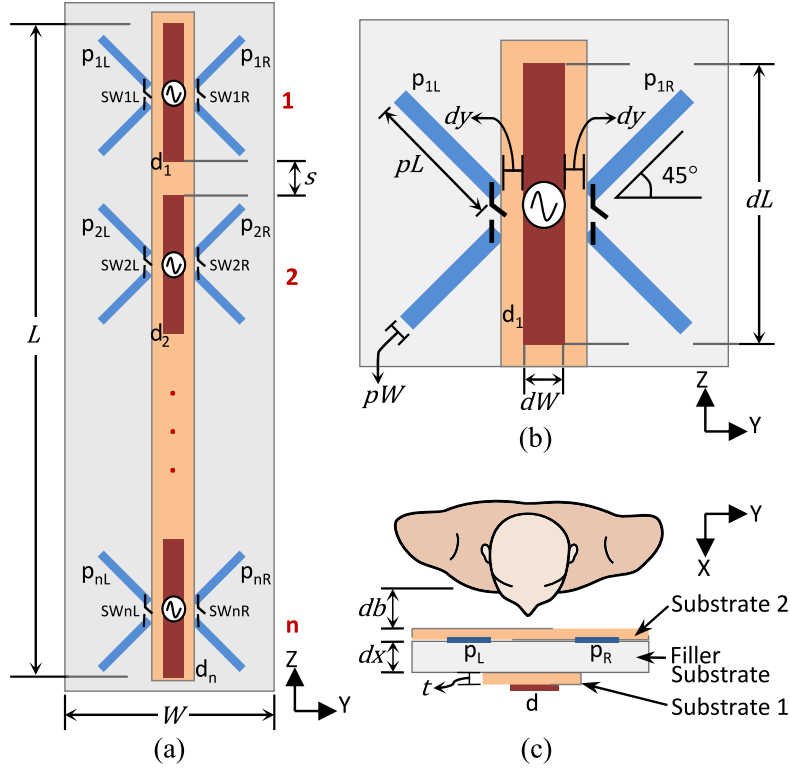


Figure 4.1 Array geometry (a) the collinear array, (b) a single sub-array, and (c) top view of the array.

The geometry of the array is shown in Fig. 4.1. As seen, the array comprises n sub-arrays. Each sub-array is composed of one driven and two v-shaped parasitic dipoles. V-shaped parasitic dipoles elements can be placed much closer to each other without deteriorating antenna matching and $|S_{11}|$.

The cross-sectional view (Fig. 4.1c) of the array shows three fabric substrate layers: on top, the driven dipoles are placed on substrate 1, in the middle, a filler substrate is located and in the bottom is substrate 2, where the parasitic dipoles are positioned. The parasitic elements have RF switches at their centers. Changing the states of these switches causes the induced currents in the parasitics to change.

Three switching states are considered: only the left switches are ON, only the right switches are ON, and all switches are ON. This allows the array beam to steer in three different directions in the azimuth (xy) plane. The parameters that were kept constant throughout the study were: $dL = 22.6$ mm, $dW = 3$ mm, $pL = 10.8$ mm, $pw = 1$ mm, and $t = 2$ mm. All fabric substrates were assumed to have a relative permittivity, ϵ_r of 1.7 and loss tangent of 0.001.

4.4 SIMULATION RESULTS

4.4.1 Array Design and Optimization

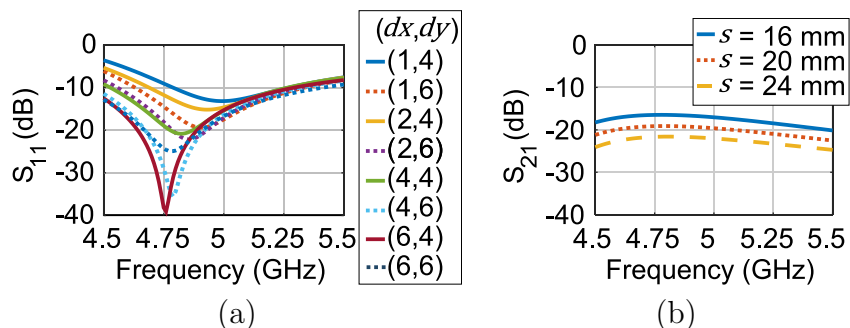


Figure 4.2 (a) Simulated $|S_{11}|$ vs. frequency for different values of dx and dy , and (b) simulated $|S_{21}|$ vs. frequency for different values of s .

The design and optimization of the array were performed using Ansys HFSS. The ON state of the switch was modelled using a SHORT while the OFF state was modelled using a 0.01 pF capacitor. First, the values of the parameters dx and dy were determined in order to discern whether the parasitic elements would act as reflectors or directors [103]. Parametric simulations were performed showing that dx could be as small as 1 mm (Fig. 4.2a), thus allowing the total thickness to be 5 mm. The parameter dy was kept fixed at 4 mm. The parameter, s determines the mutual coupling between two consecutive collinear elements. When s was varied from 16 to 24 mm, $|S_{21}|$ improved from -17 to -24 dB with all switches being ON (Fig. 4.2b).

The calculated envelope correlation coefficient was less than 0.01, suggesting reliable MIMO operation with low mutual coupling. When s was varied from 16 to 24 mm, the array gain increased from 8.9 to 9.3 dBi. As apparent, increasing n increases the array gain, e.g. with $dx = 1$ mm, $dy = 4$ mm, and $s = 16$ mm, as n varies from 6 to 8, gain increases from 8.9 to 9.6 dBi.

4.4.2 Array Performance on Curvature

The proposed array is expected to be integrated within the clothing of a person, possibly near the person's back or chest. Analyses were performed to evaluate the effects of curvature. With a formable cable the curvature of the back of a 30-year-old male subject was measured. The average curvature was found to be around 180 mm. This value was used for the simulation in this section. Figs. 4.3a. and 4.3b show the S parameters and the corresponding geometries for an array on a flat surface and on a curvature.

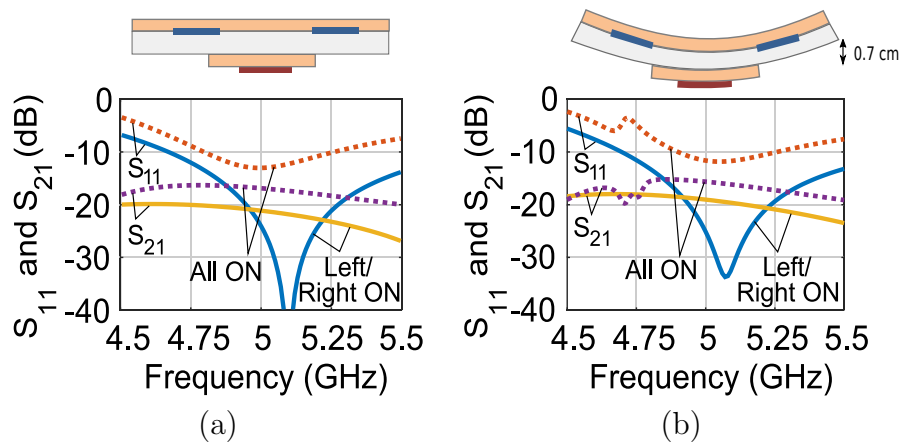


Figure 4.3 Comparison of S parameters vs. frequency for arrays on (a) flat surface and (b) curvature.

The S parameters show only minor changes as radius of 180 mm makes the array almost flat with a corner deflection of 0.7 mm. If the array is to be worn near the wrist or the arm, the radius can be as low as 30 mm, which will cause substantial

deflection, frequency shift or gain degradation is possible for that case. The array on the curved surface resulted in a small increase in the gain (gain increased from 8.9 to 9.1 dBi when all switches were ON).

4.4.3 Material Sensitivity

Simulation results of the array considering four different types of fabrics show that the array performs well. The dielectric properties of these materials were obtained from [113]. For all cases, $|S_{11}| < -10$ dB and $|S_{21}| < -15$ dB were found. The gain at 5 GHz for all cases are listed in Table 4.3.

Table 4.3 Gain variation with different types of fabrics.

Fabric type	Polyester ($\epsilon_r = 1.5$)	Polycot ($\epsilon_r = 1.6$)	Jeans cot- ton ($\epsilon_r =$ 1.7)	Fine wo- ven cotton ($\epsilon_r = 2.0$)
Peak Gain (dBi) [All Switches ON]	9.7	9.3	9	7.9
Peak Gain (dBi) [Only Left/Right Switches ON]	10.5	10.6	10.9	10.7

4.4.4 Array Performance near Human Body

The array was analyzed near a multilayered flat human phantom composed of 2 mm thick skin, 5 mm thick muscle and 10 mm thick bone layers (Fig. 4.4a). A spacer fabric is placed between the array and human body. The tissue properties at 5 GHz were obtained from IT'IS Foundation based in Zurich, Switzerland. The tissue properties at 5 GHz are listed in Table 4.4.

Table 4.4 Human tissue properties at 5 GHz.

Tissue	ϵ_r	$\sigma(Sm^{-1})$
Skin (2 mm)	35.80	3.06
Muscle (5 mm)	49.50	4.04
Bone (10 mm)	10.00	0.962

At a distance of 5 mm from the phantom, the array beam points to 30° , 0° , and 330° for left switches ON, all switches ON and right switches ON, respectively (Fig. 4.4b). At 10 mm, the array beam points to 45° , 0° , and 315° (Fig. 4.4c) with gain varying between 11.7 to 12.3 dBi. The half-power beamwidth in the azimuth plane was 90° . In the elevation plane the beamwidth is 20° (Fig. 4.4d).

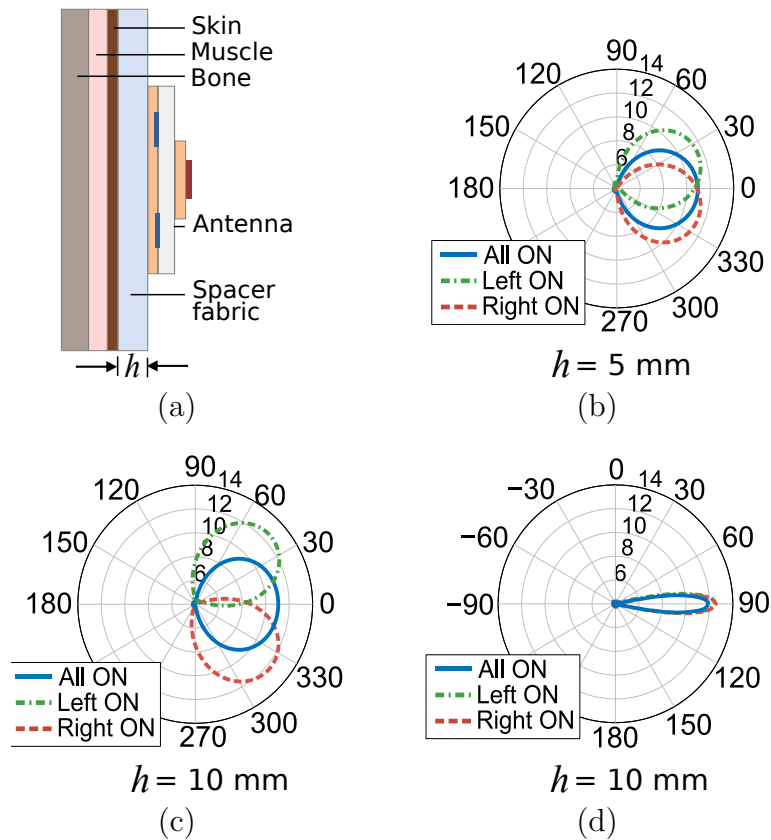


Figure 4.4 (a) Top view of the array near multilayered body phantom, realized gain patterns for this set up in the (b) azimuth (XY) plane when $h = 5$ mm, (c) azimuth (XY) plane when $h = 10$ mm, and (d) elevation (ZX) plane when $h = 10$ mm.

4.5 EXPERIMENTAL RESULTS

A microstrip patch antenna was built using a 2.7 mm thick cotton material (90% cotton, 10% olefin) as substrate and it was then compared with simulation results

obtained from Ansys HFSS. It revealed that the cotton substrate actually has a dielectric constant of 1.2.

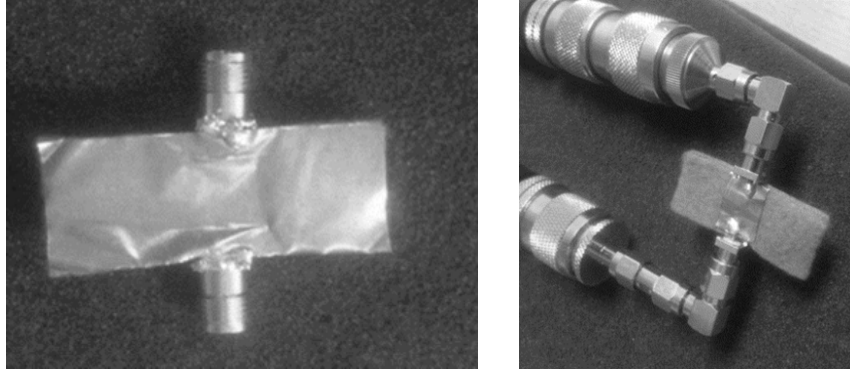


Figure 4.5 Photographs of the set up for loss tangent measurement.

To characterize the loss tangent, a 9.7 mm wide and 10 mm long microstrip transmission line was built using the cotton substrate. The line and the ground was made using flexible copper tapes. The setup for loss tangent measurement is shown in Fig. 4.5. Two port measurement was performed to find the insertion loss and using that data the loss tangent at 5 GHz was calculated using the relation [114]

$$\tan \delta = \frac{2\alpha_d \sqrt{\varepsilon_e} (\varepsilon_r - 1)}{8.686 k_0 \varepsilon_r (\varepsilon_e - 1) l} \quad (4.3)$$

where, α_d is the dielectric loss in dB, ε_r is the dielectric constant of substrate, $k_o = 2\pi f/c$, l is the length of the line, and ε_e is the effective dielectric constant which is given by, $\varepsilon_e = \frac{\varepsilon_r + 1}{2} + \left(\frac{\varepsilon_r - 1}{2}\right) \frac{1}{\sqrt{1 + 12d/W}}$.

At 5 GHz the insertion loss was measured to be 1.04 dB. By taking account of the losses from conductor and connectors loss due to dielectric alone was approximated to be 0.46 dB. Hence from (4.3) $\tan \delta$ was found as 0.084. It indicates that cotton is a lossy substrate.

CHAPTER 5

THIN SWITCHED BEAM PARASITIC ARRAY ON A NON-UNIFORM APERIODIC (NUA) METASURFACE

5.1 INTRODUCTION

Increasing interest in wearable technologies is creating demands for high performance broadband antennas. Dipole type antennas are considered as good choices for broadband operation. But they need to be properly isolated from the human body in order to reduce losses. Isolation can be achieved by placing a ground plane between the antenna and the body. But if the ground plane is too close to the antenna the return loss and gain degrade. This problem can be solved with the help of a well-designed Electromagnetic Band Gap (EBG) structure.

EBG materials are engineered materials which suppress electromagnetic wave in any given spatial direction within a certain frequency range. They have also been called High Impedance Surfaces (HIS), Artificial Magnetic Conductor (AMC), and Artificial Impedance Surfaces (AIS). Electromagnetic bandgap (EBG) materials are also known as photonic bandgap (PBG) materials or photonic crystals (PC). In 1987 Yablonovitch proposed that it should be possible to create three dimensional periodic structures that would exhibit electromagnetic band gap properties [115]. The idea was later expanded by John [116]. The existence of such band gap was experimentally established by Ho *et al.* [117]. Later Yablonovitch *et al.* experimentally showed that the Face Centered Cubic (FCC) structure could also be used as a PBG structure if holes were drilled into that structure [118]. In 1994 the ‘wood-pile’ structure was

proposed [119] and materialized [120]. Meanwhile soft and hard surfaces were proposed in [121]. In 1999 Sievenpiper *et al.* proposed the mushroom-like EBG as a high impedance surface (HIS) which inhibited the propagation of surface waves within a certain frequency band [122, 123]. Yang *et al.* developed uniplanar compact EBGs (UC-EBG) which showed a behavior similar to the mushroom-like EBG [124, 125]. Generally most of the EBG structures that have been proposed have periodic geometry. With the discovery of quasi crystals in solid-state physics aperiodic EBGs have also been introduced [126]. Other examples of EBGs and their analysis methods can be found in [127–132].

Research on antennas integrated with EBG materials dates back at least ten years [122, 123]. Since then there have been many research publications on the subject matter some on high performance microstrip patch antenna design [132–139], some on slot and circularly polarized antenna design [140–145] and some on directional dipole antenna design [146–156] using EBGs. Many commercial and military applications need directional dipole antennas that can be flush mounted on the surface of a vehicle, such as an aircraft. Yet the presence of the ground plane below the dipole poses a challenging environment to develop very thin conformal antennas especially in the lower GHz frequency range. Typically if no additional dielectric or magnetic loading is used the antenna height can very well exceed 3-5 inches at UHF (Ultra High Frequency) frequencies which is highly undesirable. The application of a well-designed EBG metamaterial as a supporting structure in between the dipole and the ground plane can alleviate this situation. Hansen’s analytical work [147] explained the interaction between a dipole antenna and the reflection phase of an EBG structure. The authors of [148] performed FDTD simulations of the reflection phase and a dipole antenna and obtained a certain range of phase angles that provided a better impedance match for a dipole.

Akhoondzadeh-Asl *et al.* [153] introduced a wideband (bandwidth = 1.7) diamond

dipole on an EBG structure with a total thickness of $0.07\lambda_0$. In our research group, Abedin et al. [152] introduced the concept of impedance modulation to develop an ultrathin printed dipole antenna (height = $0.025\lambda_0$). The impedance of a driven dipole antenna was modulated by the reflection phase of an EBG structure [152]. Also, in our research group, Azad *et al.* [155] introduced the design methodology of a wideband (bandwidth = 1.4) dipole on EBG where the interplay between the EBG reflection phase and the impedance of the dipole antenna were exploited to design a thin ($0.03\lambda_0$) directional dipole. The experimental prototype of a wideband (bandwidth = 1.5) bowtie dipole on EBG reported by Best et al. [156] had an EBG height of $0.05\lambda_0$. Tunable EBG surfaces using varactor diodes have also been introduced in [157–159]. However, they need complicated circuitry and have the potentials of emitting higher order harmonics especially at high power because of device non-linearity. Other broadband EBG structures that have been proposed include a periodic structure with unit cells consisting of different sizes of patches cascaded [160].

The summary of research activities on EBGs clearly delineate that it has been a difficult journey to reconcile the two contradictory requirements, broad bandwidth and thin very low profile design using uniform mushroom type EBG structures. The premise of this work was to address this subject from the point of a Non-Uniform Aperiodic (NUA) EBG structure. Instead of following the traditional route of illuminating the EBG surface using a plane wave source then computing its reflection phase as function of frequency and then matching it with the antenna resonant frequency we follow our previously demonstrated concept of impedance modulation [152, 155]. The latter is more logical and consequential as because the antenna is almost always operated in the near field of the EBG surface. We consider the EBG surface to be an impedance transformer that provides the necessary matching for the dipole. In support of this claim consider the works reported in [117, 127, 129, 161]. We have

found that the total electrical dimensions of the two sides of the square mushroom patch, w and its via height, h is $(2w + h\sqrt{\epsilon_{reff}})$ which is approximately a quarter wave length at the respective center frequencies considering $\epsilon_{reff} = (\epsilon_r + 1)/2$. Thus the quarter wave impedance transformer e.g. the uniform mushroom EBG surface presents a good match for the dipole antenna within its frequency of operation.

However, since the use of uniform mushroom EBG transformer has apparently reached its limits in terms of bandwidth potential for a specific thickness it is logical to consider a NUA EBG surface as a better alternative. The analogy is that of impedance matching using a standard quarter wave transformer (narrowband) versus impedance matching using multi-section transformers (broadband) where the former is analogous to the uniform EBG while the latter is analogous to the NUA EBG. Hence we model and analyze the antenna and the EBG together and then examine the impedance perturbation of the dipole as function of the EBG geometrical parameters. The goal of this paper is to explore the prospects of designing and developing a one octave bandwidth directional antenna on a NUA EBG surface with a total thickness of 1 inch ($0.04\lambda_0$) or less for operation starting at 450 MHz. The contemporary term metasurface has come to encompass any parasitic loading structure consisting of numerous small inclusions. This work represents a fully developed detailed version of our more recent conference presentation [67].

The chapter is organized as follows: first, the design of a UHF broadband fat strip dipole antenna on a traditional uniform mushroom EBG surface is presented. Second, a tapering scheme is introduced to generate a NUA metasurface that maintains the same volume as the traditional mushroom EBG surface. Using the proposed percent tapering scheme the dimensions and spacing of the patches for the NUA EBG surface can be generated. The geometrical tapering is achieved where the individual patches and their spacings are tapered according to a percent (prescribed) taper profile. Third, Simulation results of various tapering profiles are presented from

which the optimum tapering is selected that allows broadband operation. Fourth, the magnetic fields on the proposed NUA metasurface are compared to those on a conventional mushroom EBG and their differences are identified. Fifth, an experimental laboratory prototype of a UHF metasurface dipole is fabricated and tested for VSWR, pattern, and gain. Finally, based on the NUA-EBG concept design, we present the study and design of a very thin planar pattern reconfigurable antenna on EBG for operation in the 2.4 GHz ISM band. The EBG in conjunction with the parasitic array approach allows beam steering at -25 (335), 0, and 25 degrees which otherwise would have been -90 (270), 0, and 90 degrees without the EBG. The goal of investigating and designing the beam steering array on EBG structure was geared towards reducing its total thickness while achieving very high (F/B). A second objective was to attain a slight tilt in the array beam from the 90 and 270 degree directions.

5.2 FAT STRIP DIPOLE ANTENNA ON A UNIFORM MUSHROOM TYPE EBG

As a starting point, a wideband fat strip dipole operating against a mushroom type EBG structure was considered. Although a fat bow-tie dipole could have been used, a rectangular dipole was used for simplicity. The objective was to understand the maximum VSWR, pattern, and gain bandwidths that can be obtained under such an approach.

5.2.1 *Fat Strip Dipole Antenna in Free-Space*

The fat strip dipole shown in Fig. 5.1a consisted of two conducting strips each measuring 160 mm (length) by 110 mm (width). The two metal strips were separated by a 10 mm gap and was excited using a lumped port in HFSS. Simulated VSWR vs. frequency for this antenna in free-space are shown in Fig. 5.1b. As apparent, the antenna operates from 300-900 MHz within $VSWR < 3$. The patterns (not shown) resemble those of a half-wave dipole within the frequency range of 330-900 MHz (a

ratio of 2.7:1).

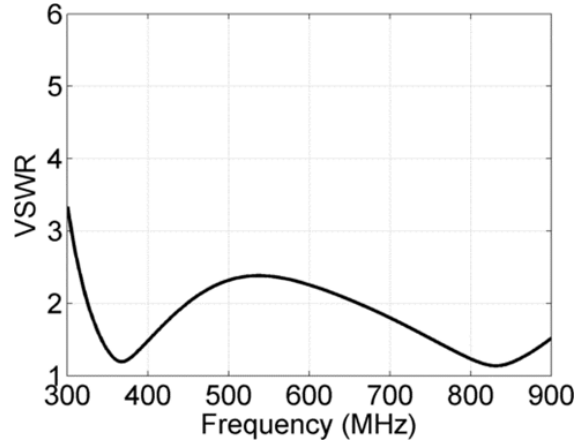
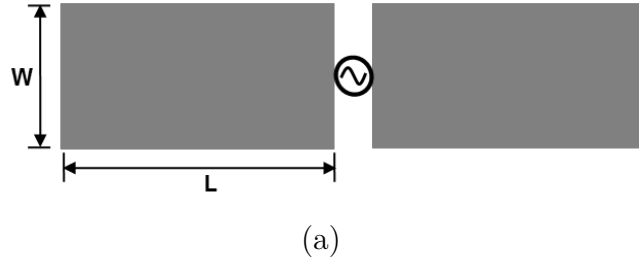


Figure 5.1 (a) Fat strip dipole; $W = 110$ mm, $L = 160$ mm and (b) its simulated VSWR.

5.2.2 UHF Wideband Dipole on Uniform Mushroom EBG Surface

Following our previous work in the 1750-2500 MHz frequency band on wideband dipole design on mushroom type EBGs [155], the unit cell size of a baseline uniform mushroom EBG was determined for operation at 450 MHz and above. This was about a factor of 4 size increase compared to the EBG design in [155]. The UHF mushroom EBG surface consists of 8 by 8 conducting patches each measuring 50 mm by 50 mm (Fig. 5.2). Each patch is separated from the other by a distance of 5 mm. The total length of the square EBG surface was 435 mm. Each EBG patch contained a 2 mm diameter conducting post at its center that connected it to the conducting ground plane below (Fig. 5.2). The total EBG thickness, $h_1 + h_2$ was 25 mm and

both $\epsilon_{r1} = \epsilon_{r2} = 4.5$ (FR4). The strip dipole described above was placed $h_3 = 1$ mm above the EBG.

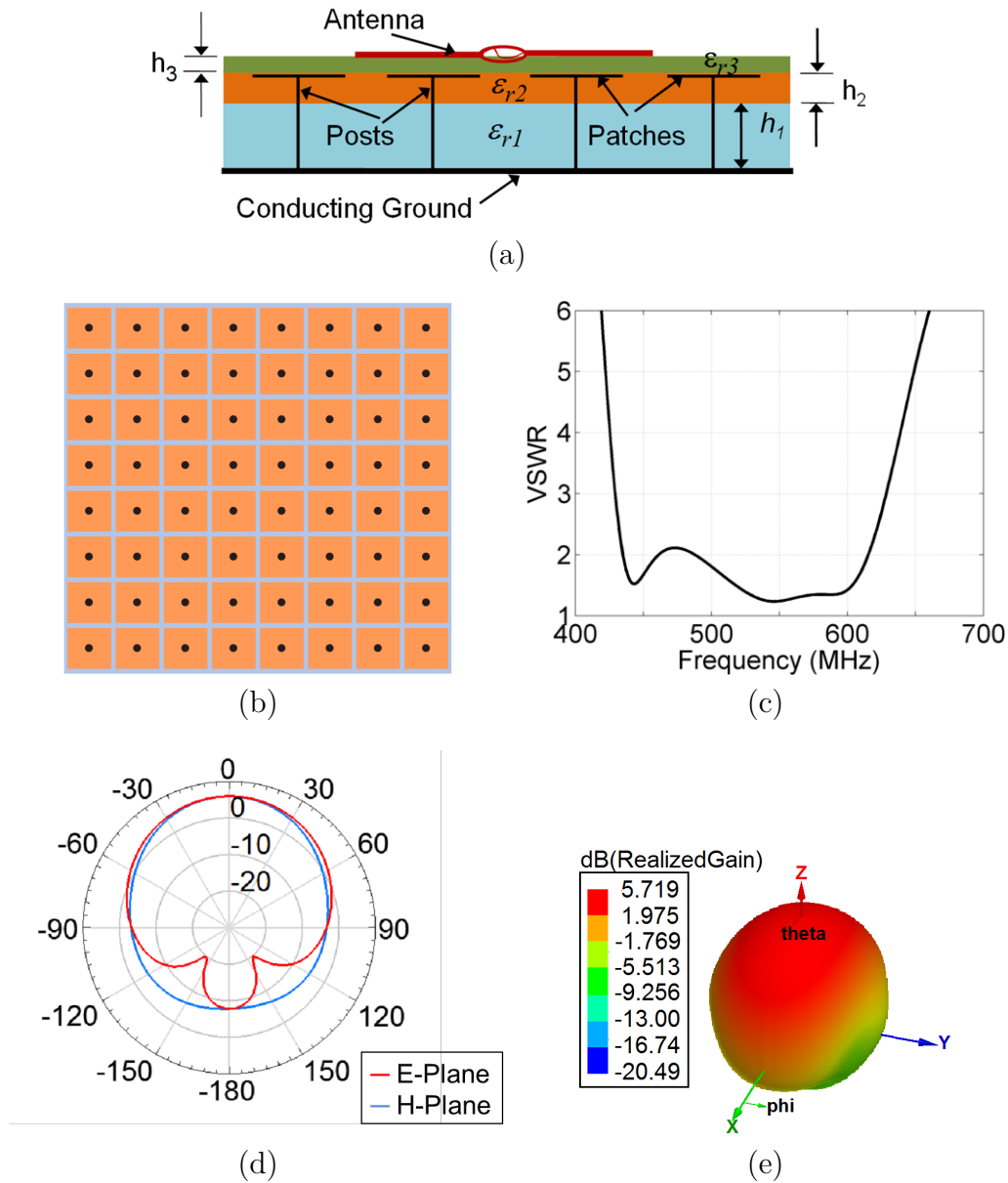


Figure 5.2 (a) A fat dipole antenna on a uniform mushroom-EBG, (b) top view, (c) simulated VSWR response. (d) simulated radiation patterns at 450 MHz, and (e) simulated 3D pattern at 550 MHz.

Simulated VSWR vs. frequency results for this case are plotted in Fig. 5.2c wherefrom it is apparent that the antenna on this EBG operates from 430 MHz to 620 MHz. The frequency ratio is 1.4 or the VSWR bandwidth is 40%. This bandwidth

is fairly typical for this type of thin design ($0.035\lambda_0$ at the lowest frequency of 430 MHz). Antenna radiation patterns (both principal planes) computed at 450 MHz are shown in Fig. 5.2d. Patterns are directional with peak gain of 6 dBi and Front to Back ratio (F/B) of about 18 dB. The three dimensional realized gain pattern at 550 MHz is shown in Fig. 5.2e. It is clear that the pattern is directional and well defined. Peak realized gain data for the same antenna on the uniform EBG are listed in Table 5.1. Peak gain varies from 1.9 to 6 dBi.

Table 5.1 Antenna realized gain on mushroom type EBG

Frequency (MHz)	440	500	550	575	585	600	620
Realized Gain (dBi)	4.9	6.0	5.7	4.4	3.7	2.2	1.9
Directivity (dBi)	5.8	7.0	6.4	5.2	4.6	3.5	2.5

5.2.3 Lightweight Low Dielectric Constant Design on Uniform Mushroom EBG Structure

Clearly the use of 25 mm (≈ 1 inch) thick FR4 material poses a practical problem which includes size, weight, fabrication issues, and cost. To ameliorate this problem, a thick low dielectric constant foam in the bottom and a thin relatively high dielectric constant material can be used on the top. With reference to Fig. 5.2a we considered $\epsilon_{r1} = 1.0$ and $\epsilon_{r2} = 4.5$ where $h_1 = 15$ mm and $h_2 = 10$ mm. Thus the thickness of the FR4 layer was 10 mm while the thickness of the foam layer was 15 mm. The VSWR vs. frequency response for this case is shown in Fig. 5.3. The operating frequency shifted higher by about 50 MHz as expected. Thus the total thickness slightly increased from $0.035\lambda_0$ to $0.04\lambda_0$. The bandwidth slightly increased. Clearly a combination of a dielectric material plus a foam with proper thickness can be used to allow the development of a light weight system.

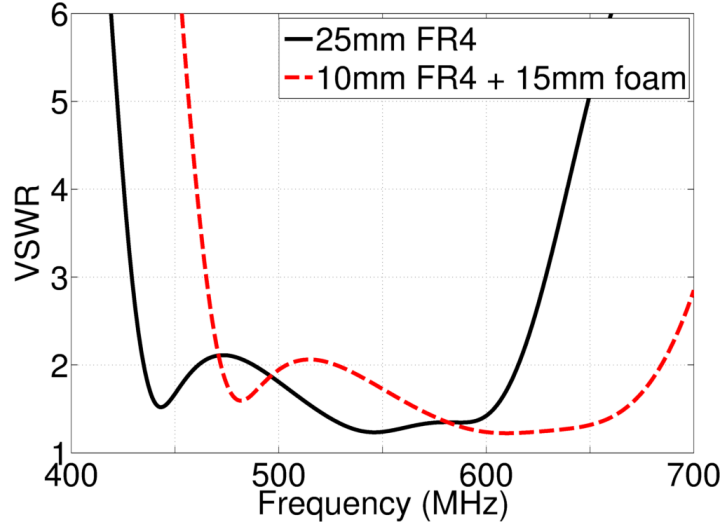


Figure 5.3 Comparison of simulated VSWR for the EBG substrate of FR4 only and a stacked substrate of FR4 and foam.

5.3 BROADBAND DIPOLE ANTENNA ON A NUA METASURFACE

5.3.1 Design Methodology of a NUA Metasurface

The bandwidth obtained using a $0.035\lambda_0$ thick EBG plus antenna combination is about 1.4:1. The design goal is to extend this bandwidth to 2:1 or even 3:1 while maintaining the same range of thickness. We looked into the analogy of broadband impedance matching where a load impedance is matched to a feed transmission line over a broad frequency range with the help of quarter wavelength long multi-section transformers. The characteristic impedance of each multisection transformer is slightly different from the other. Or, in other words, they follow a prescribed taper. The challenge for our case is to match the impedance of the dipole antenna to that of the surface impedance of the metasurface. Although much of the geometrical and material constructs of the metasurface can be tapered we focused on the patch sizes and their inter-element spacings. We considered the uniform mushroom EBG structure shown in the previous section as the baseline. The metasurface volume was

kept constant at $435 \times 435 \times 25 \text{ mm}^3$ and the dielectric material was FR4 for both ε_{r1} and ε_{r2} shown in Fig. 5.2a. The design scheme followed here can be described as follows:

- A mushroom like metasurface consisting of n by n conducting patches is placed on $n/2$ concentric square rings. The innermost ring (ring 1) is shown in Fig. 5.4 using a dotted outline. Thus the outermost ring is ring number $n/2$. The i -th ring has $4(2i - 1)$ number of patches where $i = 1, 2, 3, \dots, n/2$
- While in a conventional mushroom EBG structure all square patches have the same dimension in the proposed NUA metasurface the square patches in the same i -th ring have the same dimension but in a different i -th ring they have different dimension. Thus there is a tapering as we move from one square ring to the other. Let any square of the i -th ring have a side length, a_i .
- Also for a conventional mushroom EBG surface the spacing between two consecutive rings i.e., inter-ring spacing and the spacing between two consecutive patches in a same ring i.e., intra-ring spacing is the same. In a NUA metasurface the intra-ring spacing or the spacing between the individual patches in the same ring is fixed but the inter-ring spacing is tapered. Let the spacing between two consecutive patches in the central ring be s_1 , the spacing between rings 1 and 2 be s_2 , and the spacing between rings 2 and 3 be s_3 and so on.
- The tapering can be described as follows

$$a_{i+1} = r a_i \quad (5.1)$$

$$s_{i+1} = r s_i \quad (5.2)$$

where $i = 1, 2, 3, \dots, (n/2 - 1)$ and

$$r = \left(1 \pm \frac{p}{100}\right) \quad (5.3)$$

where p is the percent increase or decrease in the patch size (plus sign in equation (5.3) for increase and minus sign in equation (5.3) for decrease) and the parameters and are determined as follows.

- Let a_{base} be the width of the square patches of the conventional mushroom EBG surface. Then a_1 is found by letting a_{base} be the average of the different patch widths, a_1 to $a_{n/2}$.

$$a_1 + a_2 + \cdots + a_{n/2} = \frac{n}{2}a_{base} \quad (5.4a)$$

$$\text{or, } a_1 + ra_1 + \cdots + r^{(n/2-1)}a_1 = \frac{n}{2}a_{base} \quad (5.4b)$$

$$\text{or, } a_1 = \frac{n}{2} \frac{a_{base}(r-1)}{r^{(n/2)} - 1} \quad (5.4c)$$

- The variable s_1 is found by keeping the total length, L constant

$$2(a_1 + a_2 + \cdots + a_{n/2}) + (s_1 + 2s_2 + 2s_3 + \cdots + 2s_{n/2}) = L \quad (5.5a)$$

$$\text{or, } s_1 = \frac{L(r-1) - 2a_1(r^{n/2} - 1)}{2(r^{n/2} - 1) - (r-1)} \quad (5.5b)$$

For example, for $n = 8$, $L = 435$ mm, $a_{base} = 50$ mm and $p = 20$ (for 20% decreasing taper) the parameter values listed in Table 5.2 will be the result. The corresponding geometry is shown in Fig. 5.4. Similarly, for a 15% increasing taper, the dimensions listed in row 5 of Table 5.2 will be the result.

As stated earlier, for the studies and design of this paper, $n = 8$ was considered. However, the dimensions for $n = 10$ and $n = 12$ with a 20% decreasing taper are given in Table 5.3. These dimensions were arrived at by considering the same patch size and spacing as that of the uniform mushroom-type EBG, obtaining a_1 and then L from (5.1) to (5.5).

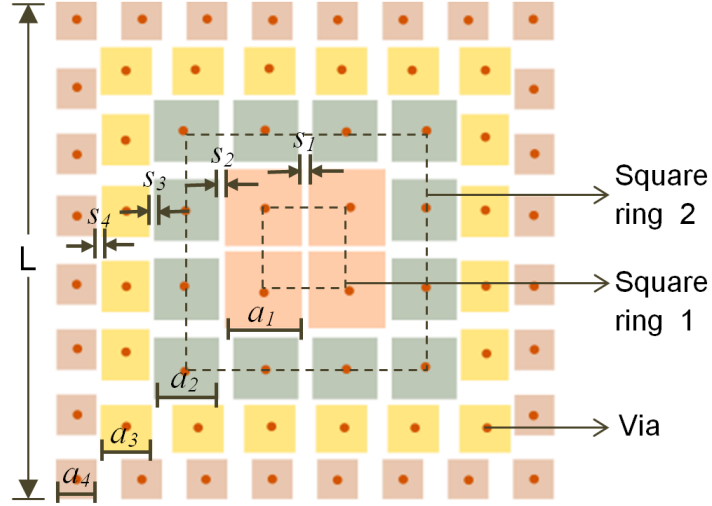


Figure 5.4 Top view of a NUA metasurface with 20% decreasing taper.

Table 5.2 Patch width (in mm) and inter-element spacing (in mm).

Taper profile	a_1	a_2	a_3	a_4	s_1	s_2	s_3	s_4
2% increase	48.4	49.3	50.4	51.4	4.9	5	5.1	5.2
4% increase	47	48.9	50.8	52.9	4.7	4.9	5.1	5.3
10% increase	43.1	47.4	52.1	57.4	4.2	4.6	5.1	5.6
15% increase	40	46	53	60.9	3.9	4.5	5.1	5.9
2% decrease	51.4	50.4	49.3	48.4	5.3	5.2	5.1	5
4% decrease	53	50.9	48.8	46.9	5.4	5.2	2	4.8
10% decrease	58	52.2	47	42.3	6	5.4	4.9	4.4
15% decrease	63	53.5	42.5	38.7	6.2	5.3	4.5	3.8
20% decrease	68	54.4	43.5	34.8	6.8	5.4	4.4	3.5

Table 5.3 Patch width (in mm) and interelement spacing (in mm) for 20% decreasing taper for different number of elements.

n	a_1	a_2	a_3	a_4	a_5	a_6	s_1	s_2	s_3	s_4	s_5	s_6	L
8	68	54.4	43.5	34.8			6.8	5.4	4.4	3.5			435
10	74.4	59.5	47.6	38	30.5		7.9	6.3	5	4	3.2		545
12	81.3	65	52	41.6	33.3	26.6	8.6	6.9	5.5	4.4	3.5	2.8	655

As shown, with $n = 8$, the maximum to minimum patch size has a ratio of 2. This ratio increases to 2.4 and 3, respectively, for $n = 10$ and $n = 12$. Moreover,

note that, with increasing n , the total dimension L increases. As we will observe later, the parameter L has an important influence on the antenna radiation pattern, particularly when it is one wavelength.

Choosing too few patches would make the structure too small to fully support the near fields of the radiating element. This will also create undesirable amount of high back radiation. The number of patches, i.e., 8 by 8, and the patch sizes chosen for UHF band design in this paper, was a compromise in that respect. Our premise is such that, if one wishes to use $n = 10$ or 12 , then one should determine the patch sizes and spacing based on the baseline design metric first and by using the equations provided. The baseline design metric is a quarter-wave transformer as explained earlier in Section 1. However, it should be noted that a change in n may require finding an optimum design that entails determining the proper amount of taper, the dipole size, and the dipole height.

5.3.2 Simulation Results of Increasing Taper

Initially, NUA structures with increasing taper was considered. For example, the patch dimensions and spacings for 2%, 4%, 10% and 15% increase are listed in Table 5.2. The total length, mm was kept unchanged and was considered. Substrate material and thickness was also unchanged (FR4, 25 mm thick). Each patch contained a 2 mm diameter via as before. Numerous simulations were performed among which the results of several simulations are shown in Figs. 5.5 and 5.6.

Observing the VSWR results shown in Fig. 5.5 it is clear that they do not show any sign of improvement in antenna bandwidth. Actually, the bandwidth worsens as the amount of taper increases. We should note that the operation of the dipole against this AIS manifests itself as a coupled resonance phenomenon as seen in Fig.5.6a, where only a slight taper (2% increasing) has been introduced. There are two visible knots that contain the frequency ranges of 420-475 MHz and 500-600 MHz, respectively.

Although these two resonances are isolated from each other since they mutually interact with each other knot 1 is primarily due to the dipole while knot 2 is primarily due to the AIS. As the taper increases to 5%, the patch size in the innermost ring reduces to 47 mm pushing the AIS resonant frequency higher.

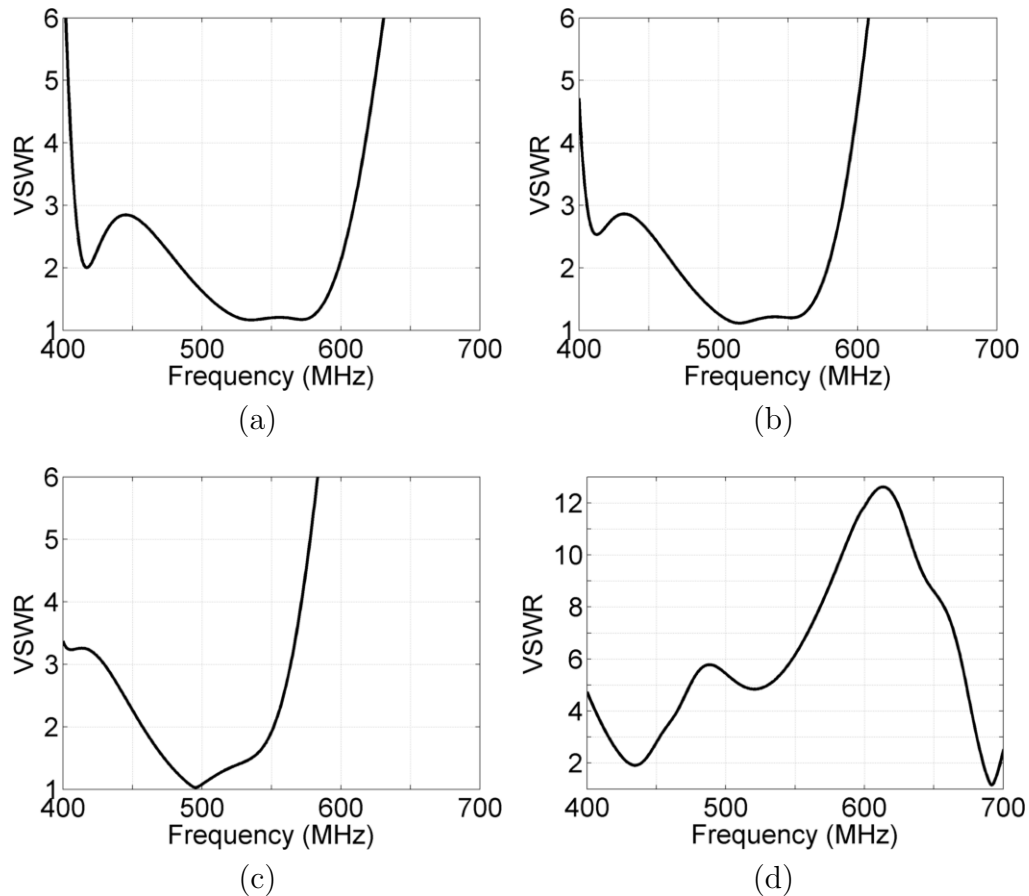


Figure 5.5 Simulated VSWR responses for a dipole on NUA metasurface with different increasing taper profiles; (a) 2%, (b) 3%, (c) 4%, and (d) 5%.

As a matter of fact, since there are different rings with different patch sizes each AIS ring should have its own characteristic resonance if there is a significant change in the patch dimension as one moves from one ring to another. Fig. 5.5d shows a dipole that is loosely coupled to the AIS that is clearly operating at a higher frequency. This problem can potentially be solved by using a decreasing taper that will allow larger

size patches near the dipole region and smaller size patches away from the dipole which is the subject matter of the discussion in the following section.

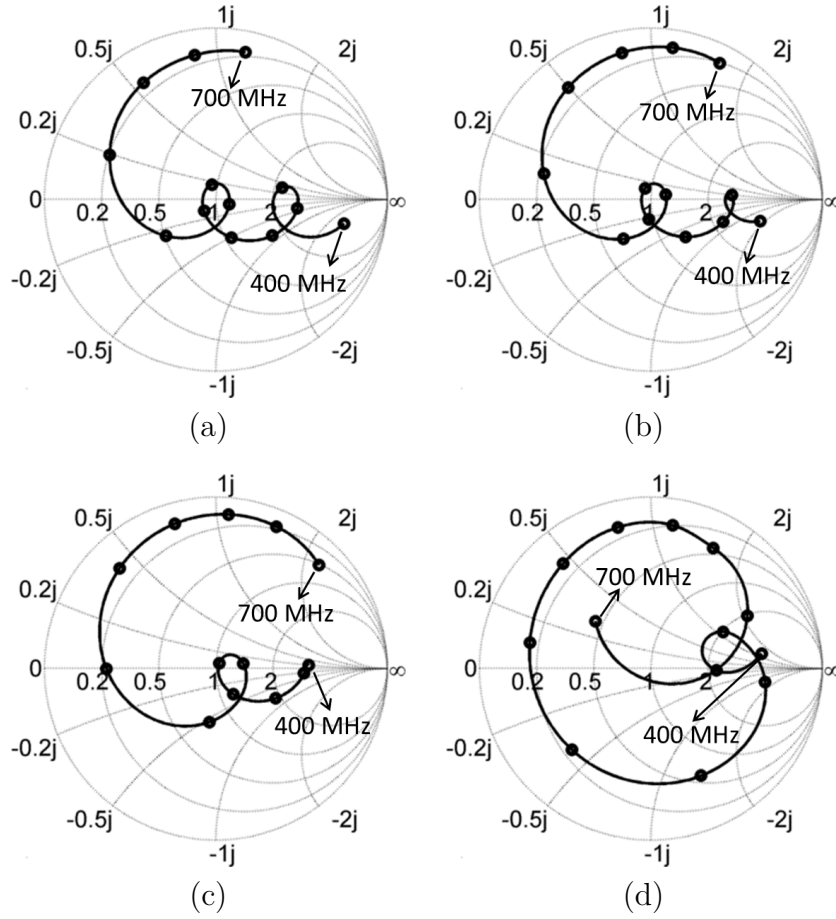


Figure 5.6 Simulated impedance Vs. frequency data for dipole on NUA metasurface with different increasing taper profiles; (a) 2%, (b) 3%, (c) 4%, and (d) 5%.

5.3.3 Simulation Results of Decreasing Taper

Based on the observations and the understanding from before cases of decreasing taper were considered next. Several cases of patch dimensions and spacing with decreasing taper are listed in Tables 5.2 and 5.3. As apparent, any amount of decreasing taper results in larger size patches near the center and smaller size patches away from the center. Fig. 5.7 shows the simulated VSWR vs. frequency characteristics for a

number of cases with decreasing tapering. Corresponding impedance vs. frequency characteristics are shown in Fig. 5.8.

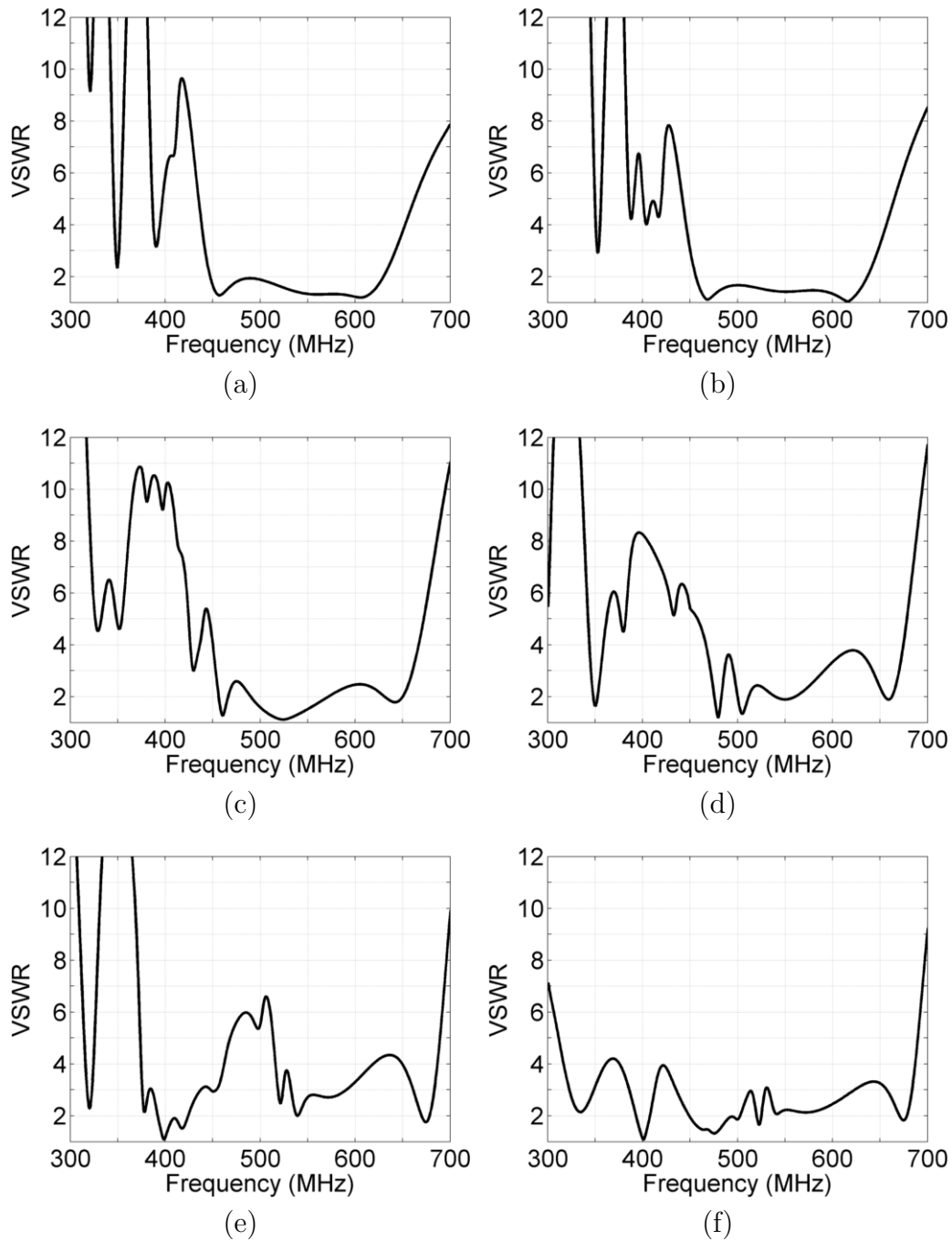


Figure 5.7 Simulated VSWR response of dipole on NUA metasurface with different decreasing taper profiles; (a) 2%, (b) 4%, (c) 10%, (d) 15%, (e) 20%, and (f) 20% tapering with dipole arm length adjusted to 120 mm each.

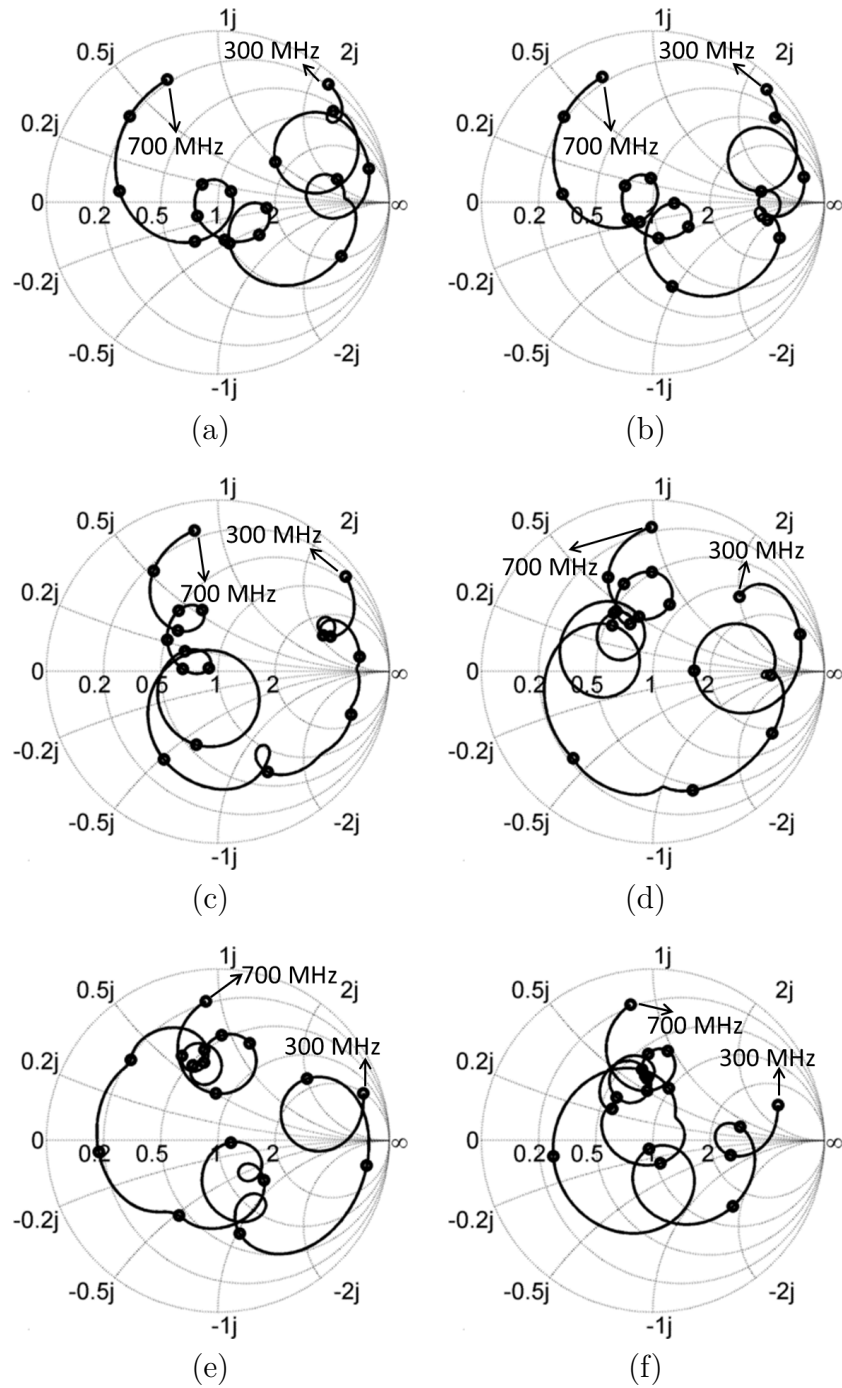


Figure 5.8 Simulated impedance Vs. frequency for dipole on NUA metasurface with different decreasing taper profiles: (a) 2%, (b) 4%, (c) 10%, (d) 15%, (e) 20%, (f) 20% tapering with arm length of the dipole adjusted to 120 mm each.

Comparing Figs. 5.6a and 5.8a within the 400-700 MHz frequency range one can

observe that there are three visible knots for the latter while two for the former. As the amount of decreasing taper increases, increased coupling between the dipole and the AIS surface is observed. At 20% decreasing taper (Fig. 5.8e) it is clear that there is significant coupling and hence bandwidth potential if the top and bottom knots on the center of the Smith chart can be moved further to the center. That is when adjusting the dipole length was attempted. The simulation results with the dipole length as the parameter are shown in Fig. 5.9. By gradually reducing the dipole length the coupling between the dipole and the AIS was made to be optimum resulting in a broadband response as seen in Fig. 5.7e.

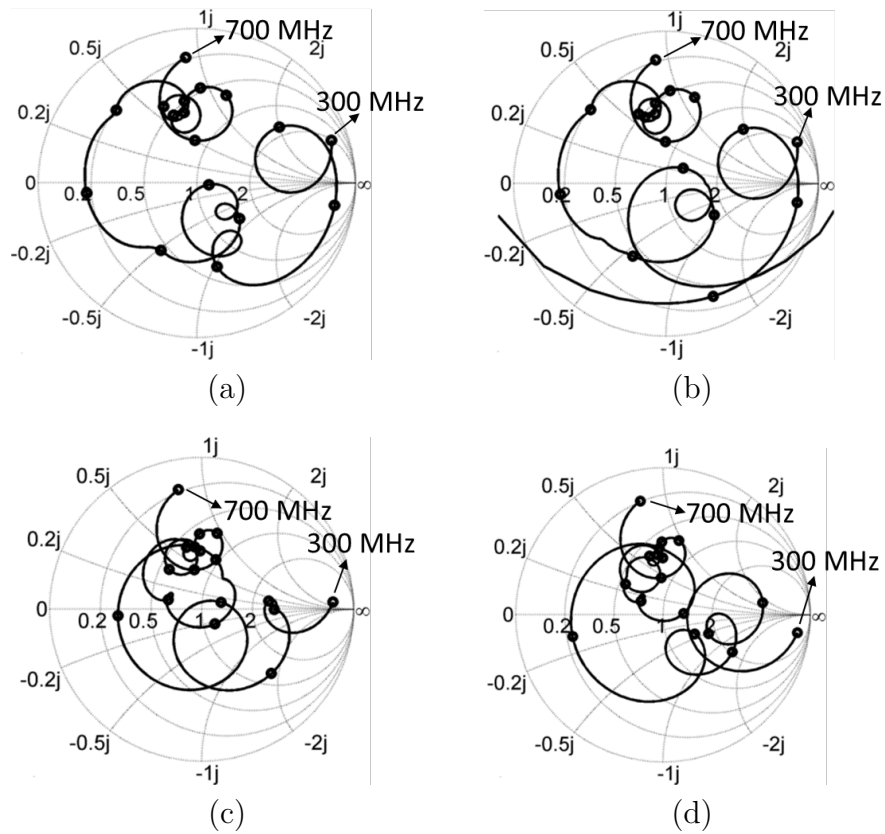


Figure 5.9 Simulated impedance Vs. frequency for dipole on NUA metasurfaces with 20% decreasing taper profile. (a) arm length= 156 mm, (b) arm length= 140 mm, (c) arm length= 120 mm, and (d) arm length= 100 mm.

5.3.4 An Effective Antenna EBG system

The results shown in Fig. 5.7e show clear potential for broad bandwidth extending from 320-680 MHz within VSWR < 3:1 which is more than an octave. Although in some regions across the frequency band the VSWR exceeds 3:1, it is expected that further tuning will reduce these numbers. Simulated peak realized gain patterns are shown in Figs. 5.10 and 5.11.

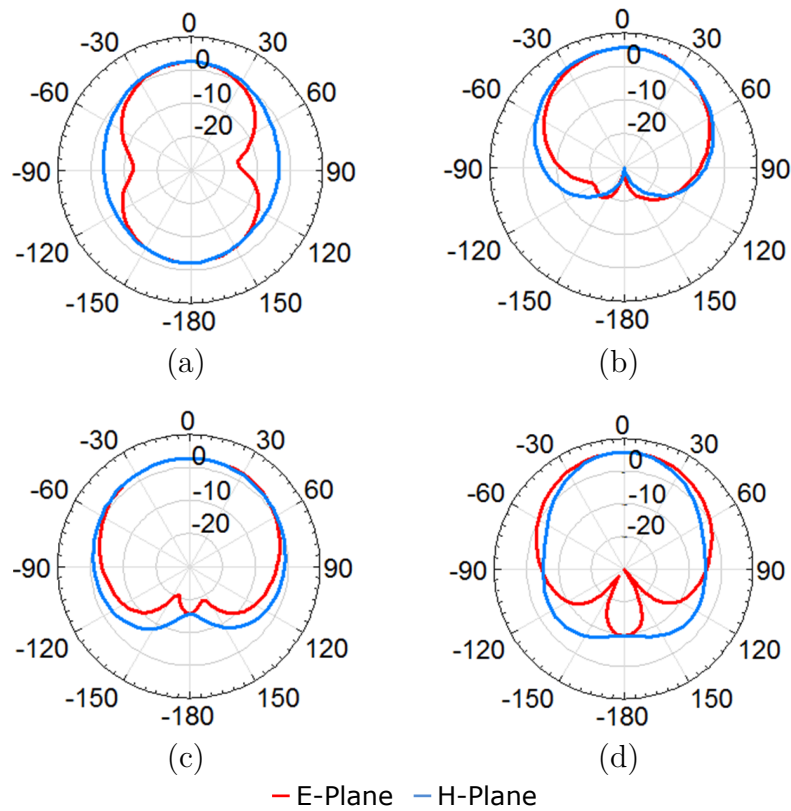


Figure 5.10 Simulated realized gain patterns at (a) 319 MHz, (b) 450 MHz, (c) 550 MHz, and (d) 600 MHz.

As apparent, the patterns are directional. The peak realized gain numbers at various frequencies are also listed in Table 5.4. The peak realized gain is greater than 2 dBi at all frequencies except at 400 MHz. The directivity at 400 MHz is high but, the gain is near -0.5 dBi. Similar in-band gain degradation was also observed by the authors of [156]. The reason given was that the gain degradation was due to the vias.

Table 5.4 Simulated antenna realized gain and directivity on the proposed NUA metasurface

Frequency (MHz)	319	400	450	500	550	600	650
Realized Gain (dBi)	2.5	-0.5	5.6	2.1	2.8	5.8	4.4
Directivity (dBi)	4.8	5	7.1	5.1	4.8	7.2	6.7

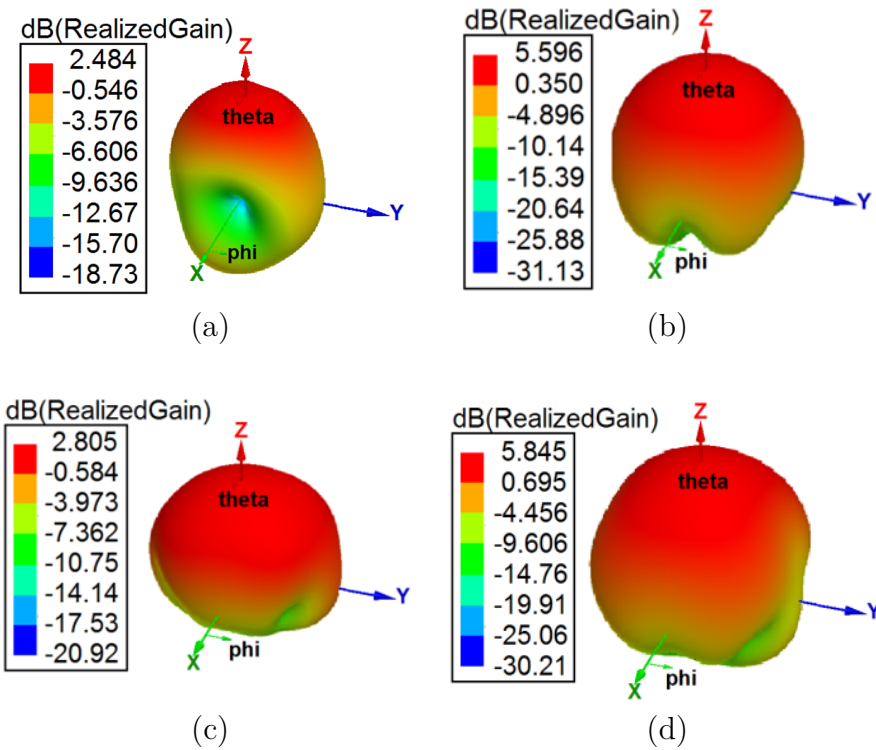


Figure 5.11 Simulated three dimensional realized gain patterns at (a) 319 MHz, (b) 450 MHz, (c) 550 MHz, and (d) 600 MHz.

Further evidence of improving the tuning is shown in Fig. 5.12 which shows that some degree of control on the VSWR response can be obtained by adjusting the height of the dipole from the NUA surface. Consequently, once the metasurface design is complete the dipole lengths, widths, and the dipole height can be adjusted to further improve the VSWR matching, gain, and pattern performance.

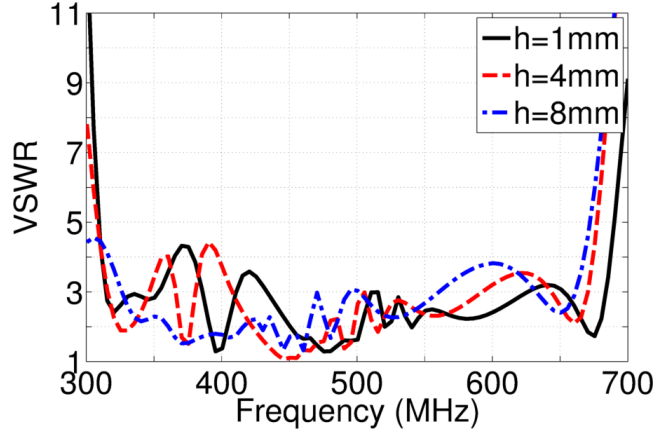


Figure 5.12 VSWR tunability of the broadband antenna on the NUA metasurface; h represents the height of the Antenna from the metasurface.

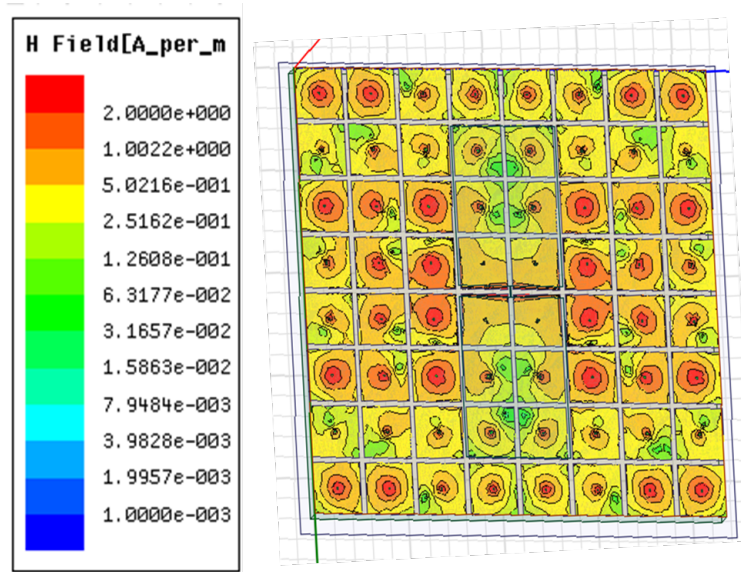
Simulated magnetic field distributions of a dipole on a conventional mushroom EBG and on a NUA metasurface are compared in Fig. 5.13. In both cases the fat strip dipole was used as the illuminating source and magnetic fields were computed at 500 MHz. As seen, unlike the H-fields on the uniform mushroom EBG structure the H-fields on the NUA metasurface (Fig. 5.13b) show that the fields on this structure are excited like a tapered distribution. The broadband performance resulted likely due to that.

5.4 EXPERIMENTAL RESULTS

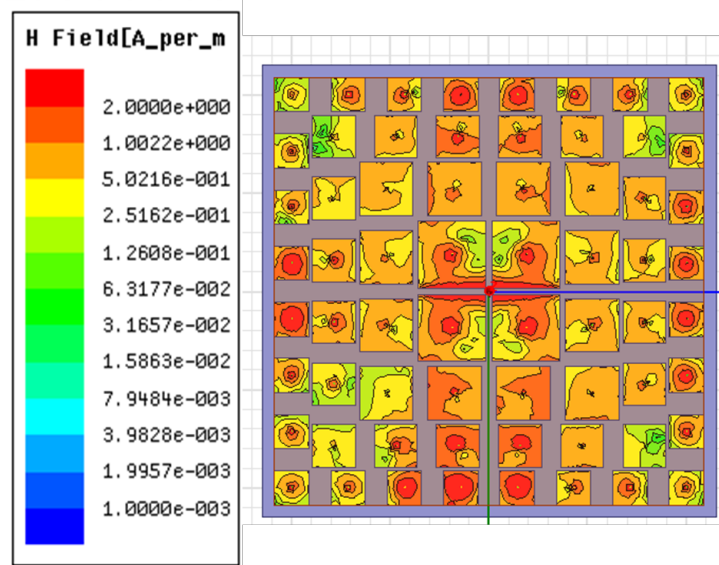
To determine the validity of these simulation results, an experimental NUA metasurface was fabricated. Photographs of the fabricated metasurface and the metasurface plus the dipole antenna are shown in Fig. 5.14.

Due to the unavailability of a thick FR4 material we used plexiglass ($\epsilon_r = 3.4$) as the substrate. Four plexiglass dielectric slabs were clamped together to form a total thickness of 0.88 inch (22.3 mm). A total of 64 holes were created on the substrate

through which copper conducting posts were routed. A brass sheet was used as the ground plane below the plexiglass substrate.



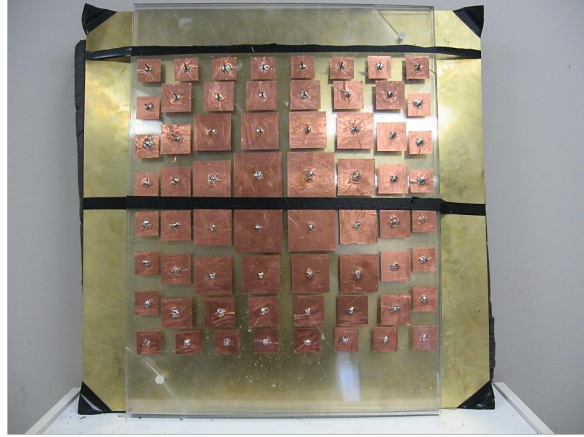
(a)



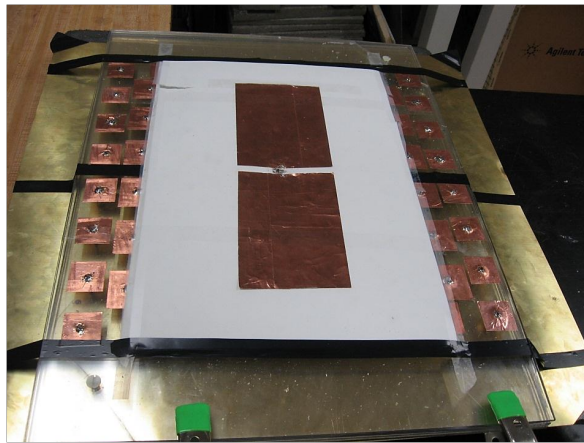
(b)

Figure 5.13 Simulated magnetic (H) field distributions at 500 MHz on (a) conventional mushroom EBG surface and (b) NUA metasurface.

Each metasurface patch was made from flexible copper tape. At the center of each metasurface patch a hole was drilled and a 2 mm diameter copper wire was inserted.



(a)



(b)

Figure 5.14 Photographs of (a) the NUA metasurface and (b) metasurface plus dipole antenna. Total surface area 435 mm by 435 mm (17.1 inch by 17.1 inch).

The copper wire was then soldered to the metasurface patch on the top and the brass ground plane below. Since large brass sheets are heat sinks a heat gun was used along with a soldering iron to solder the conducting copper wires. The dipole antenna was also made from flexible copper tape and was placed on a very thin foam material as shown in Fig. 5.14 . To feed the dipole a semirigid coaxial cable was routed through the cable and the plexiglass substrate by drilling a large enough hole. The coaxial cable was connected to a broadband surface mount chip balun (RFXF9503). The

balanced output from the surface-mount chip balun was then used to excite the two dipole arms.

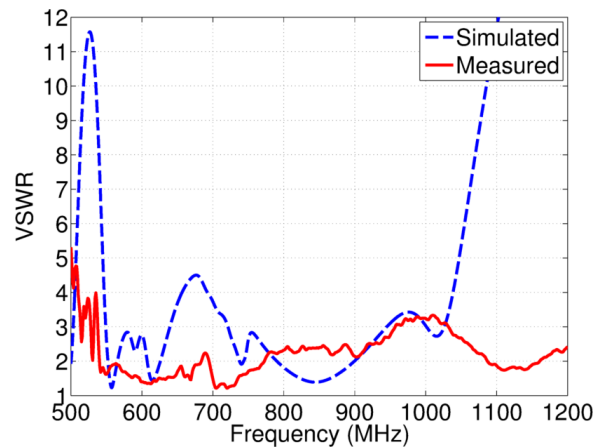


Figure 5.15 Simulated and measured VSWR Vs. frequency of dipole on NUA-metasurface.

Measured VSWR vs. frequency data of the dipole on the NUA metasurface are shown in Fig. 5.15. It is clear that the antenna operates from 537-1180 MHz within $VSWR \leq 3 : 1$. The bandwidth is more than an octave, as before, while the total thickness is $0.04\lambda_0$. The operating frequency for the experimental prototype shifted higher compared to the simulations because we used plexiglass as opposed to FR4 and also the thickness used is slightly less than what was used in the simulations. Furthermore, the experimental specimen had multilayer dielectric slabs joined together that contained air pockets in between and were slightly deformed in some areas during the drilling, soldering, and assembly.

The antenna VSWR was also simulated using plexiglass as the substrate. However, using the dielectric constant value for plexiglass listed in HFSS library ($\epsilon_r = 3.4$) did not yield good performance. Measured dielectric constant value of plexiglass has been reported to be 2.5 in [162]. Considering the multilab scheme and the air pockets within for our construction the dielectric constant was assumed to be less

than 2.5. Simulations were performed considering dielectric constant of 1.8, 2.0 and 2.2 that showed the results of the 1.8 dielectric constant model to generally follow the measured data.

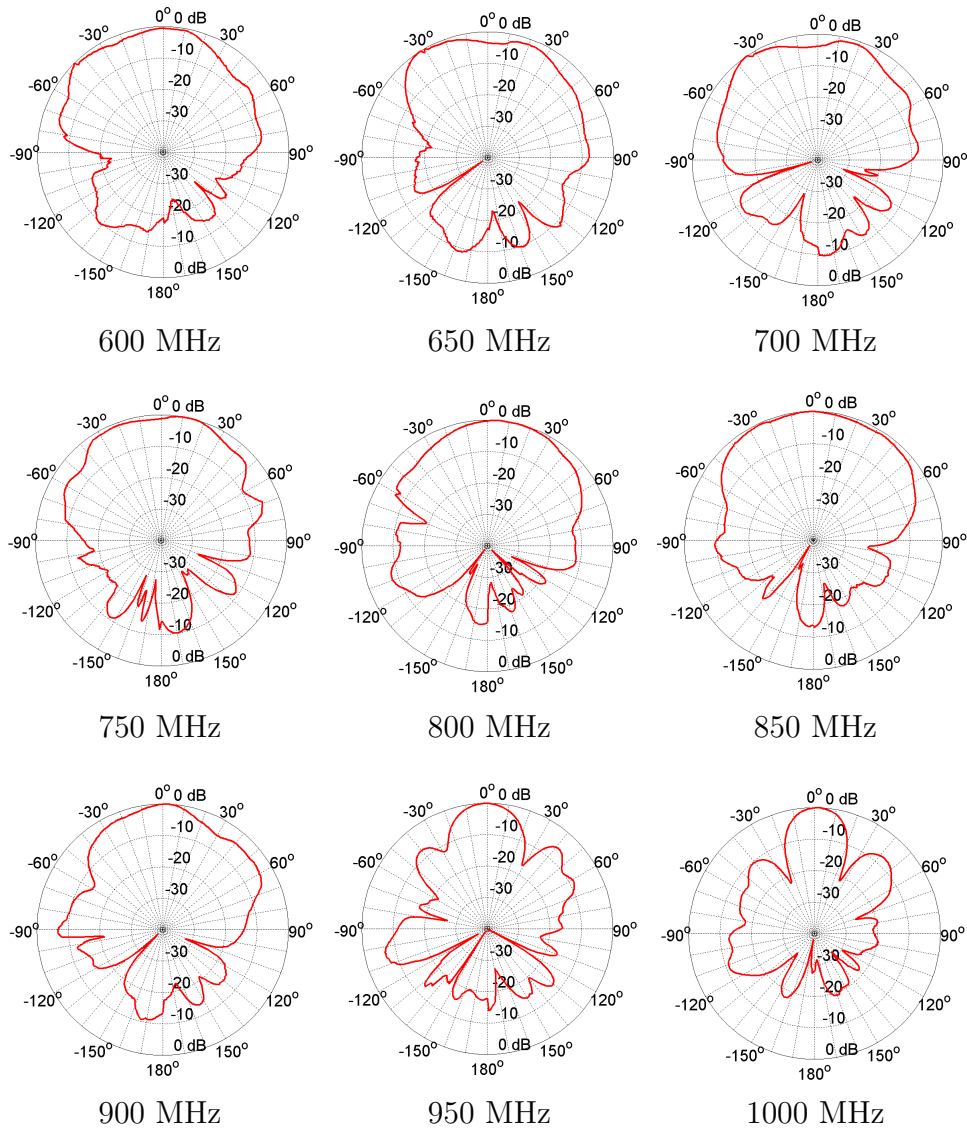


Figure 5.16 Measured normalized E-plane radiation patterns.

The simulated results showed operating bandwidth from 550-1030 MHz within 3:1 VSWR but with additional VSWR peaks at 680 MHz and 980 MHz. The VSWR peaks in the simulation data at 680 MHz was 4.5 and at 980 MHz was 3.4 with the former being not present in the experimental data.

Measured normalized gain patterns in the E-plane from 600-1000 MHz at 50 MHz intervals are shown in Fig. 5.16. Patterns are directional with the F/B exceeding 10 dB at most frequencies. Larger F/B can be achieved with a larger metasurface than the one used here. The main beam becomes narrower as the frequency increases to 1000 MHz and side lobes start to appear as expected.

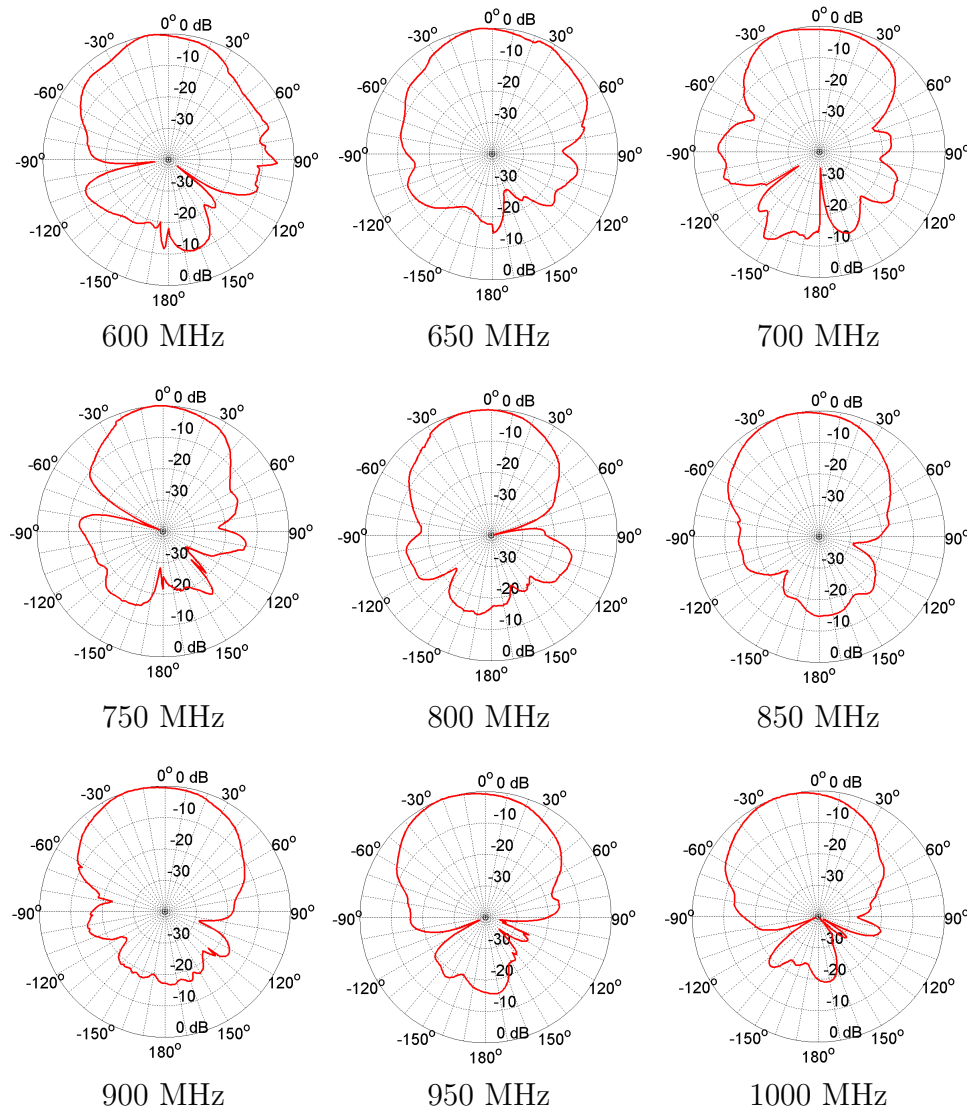


Figure 5.17 Measured normalized H-plane radiation patterns.

Measured normalized gain patterns in the H-plane from 600-1000 MHz at 50 MHz intervals are also shown in Fig. 5.17. These patterns are also directional with the

F/B exceeding 10 dB at most frequencies. Unlike the E-plane patterns the H-plane patterns show slight leftward tilt compared to the broadside direction of $\theta = 0$ degree.

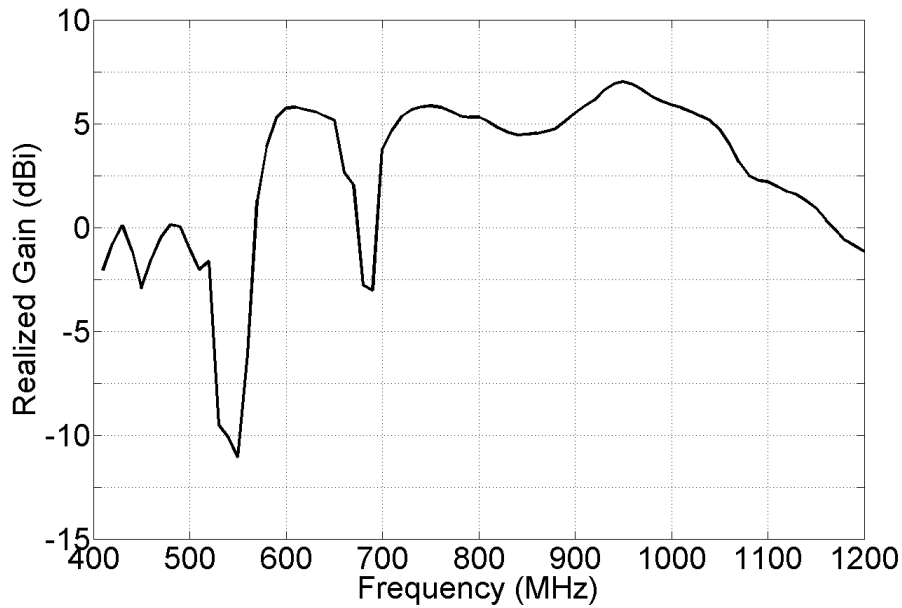


Figure 5.18 Measured dipole broadside realized gain vs. frequency on the NUA metasurface.

The measured broadside realized gain data shown in Fig. 5.18 show that the antenna on the proposed NUA metasurface has good gain (>1 dBi) within the frequency range of 570 MHz to 1150 MHz with the exception of the frequency range of 675 MHz to 695 MHz (20 MHz) where the gain falls off to -2.8 dBi. The drop seen in the gain within this very narrow frequency range is because of beam peak direction change. The patterns at 680 MHz have been plotted in Fig. 5.19 to underscore this broadside gain degradation.

Note that the peak gain at 680 MHz is about -0.2 dBi and is directed along $\theta = 45^\circ$. It is interesting to note that the overall size of the NUA structure (435 mm) is one wavelength at 680 MHz. Thus it is likely that a lateral mode of radiation is the cause for the beam peak direction change and the reduction in antenna gain within a very narrow frequency range. However, one can redesign the NUA metasurface

structure such that the total dimension coincides with the wavelength corresponding to the frequency at its lower band edge of operation. Radiation patterns at 1050 MHz are also shown in Fig. 5.19 which show that the antenna patterns are generally satisfactory at this high frequency.

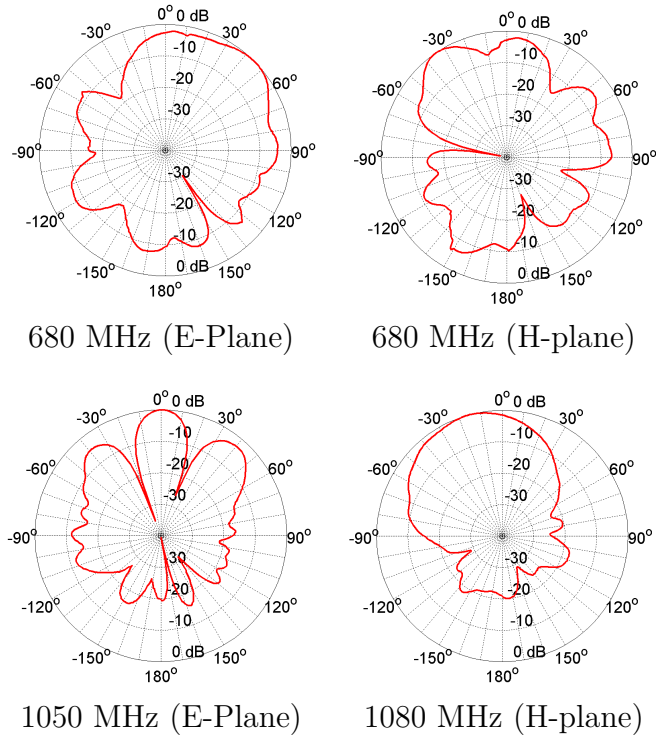


Figure 5.19 Measured dipole patterns at other frequencies (on NUA- metasurface).

5.5 SWITCHED BEAM ARRAY ON NUA EBG SURFACE

The NUA EBG concept presented in the earlier sections of this chapter has been exploited to develop a thin switched beam parasitic array.

5.5.1 Array Configuration

The array geometry shown in Figs. 5.20a and 5.20b shows that it has two parts: an antenna on Substrate 1 (ϵ_{r1} and thickness, h) and an EBG structure on Substrate 2 (ϵ_{r2} and thickness, t).

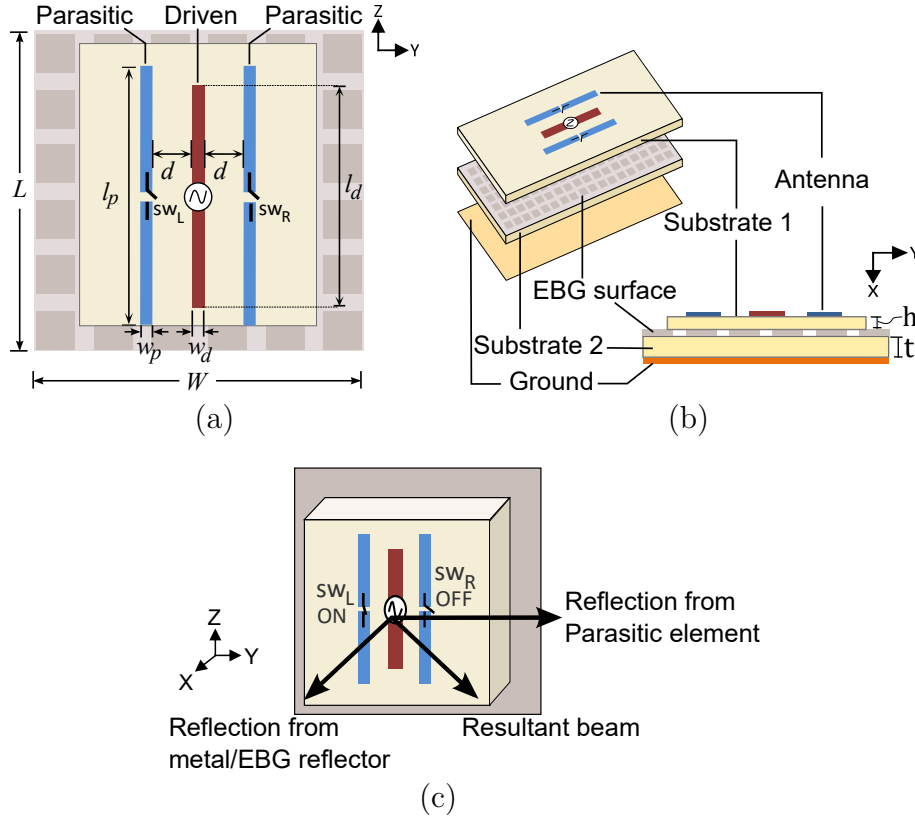


Figure 5.20 Measured dipole broadside realized gain vs. frequency on the NUA metasurface.

The EBG structure is composed of a frequency selective surface consisting of square metal patches on a substrate and a ground plane (Fig. 5.20b). The antenna consists of one driven and two parasitic planar dipole elements (Fig. 5.20a). The length and width of the driven element are l_d and w_d , respectively. Similarly the length and width of each parasitic element are l_p and w_p , respectively. L and W represent the total length and width of the array on the EBG. Edge-to-edge separation between the driven and one of the parasitic dipoles is d . The parasitic elements have RF switches at their centers (sw_L and sw_R in Fig. 5.20a). Array operation can be explained using [103] and from Fig. 5.20c when there is no EBG and ground plane present. When only the Left switch (sw_L) is ON, the left parasitic element operates as a reflector which directs the array beam to $\phi = 90^\circ$ (y -axis). Similarly when only

the Right switch (sw_R) is ON the beam points to $\phi = 270^\circ$. When both switches are ON, the beam points in the forward direction ($\phi = 0^\circ$).

5.5.2 Results

First, a three element switched beam antenna array was designed ($l_d = 57$ mm, $w_d = 3$ mm, $l_p = 65$ mm and $d = 20$ mm) for operation in free-space at 2.4 GHz. The array performed as expected. Good return loss and beam steering at 0, 90, and 270 degrees were observed. When the array was placed at a height from a 125 mm square copper reflector it was found that a separation of at least 18 mm ($\approx 0.14\lambda_0$ from the reflector) was required to obtain good return loss. Subsequently the space between the array and the reflector was filled with Rogers TMM4 ($\epsilon_r = 4.5$) substrate. To ensure that the array still operated at 2.4 GHz its dimensions were adjusted as $l_d = 18$ mm, $l_p = 18$ mm, and $d = 18$ mm. It was found that a minimum thickness of 11 mm for the TMM4 was needed for the antenna to have acceptable return loss. Neither of these approaches seemed feasible or desirable from a practical point of view because of large thickness.

5.5.2.1 Array on Uniform Planar EBG

Next, array performance was studied on a planar EBG (Fig. 5.21a) structure. The EBG consisted of 6×6 square patches on TMM4 substrate (thickness t).

The planar EBG was designed for operation at 2.4 GHz based on the guidelines found in the literature [163]. The geometrical parameters for the EBG and antenna were $a = 16.3$ mm, $s = 1.6$ mm, $h = 1.2$ mm, $t = 5.8$ mm, $l_d = 34.5$ mm, $l_p = 45.5$ mm, $w_d = w_p = 3.1$ mm, and $L = W = 106.8$ mm, $\epsilon_{r1} = \epsilon_{r2} = 4.5$. The smallest total thickness ($h + t$) that allowed good return loss was found to be 7 mm ($0.056\lambda_0$). As seen in Fig. 5.21b, $|S_{11}| < -10$ dB is satisfied at 2.4 GHz for all three switching combinations with bandwidth being 8%. Fig. 5.21c show the realized gain patterns

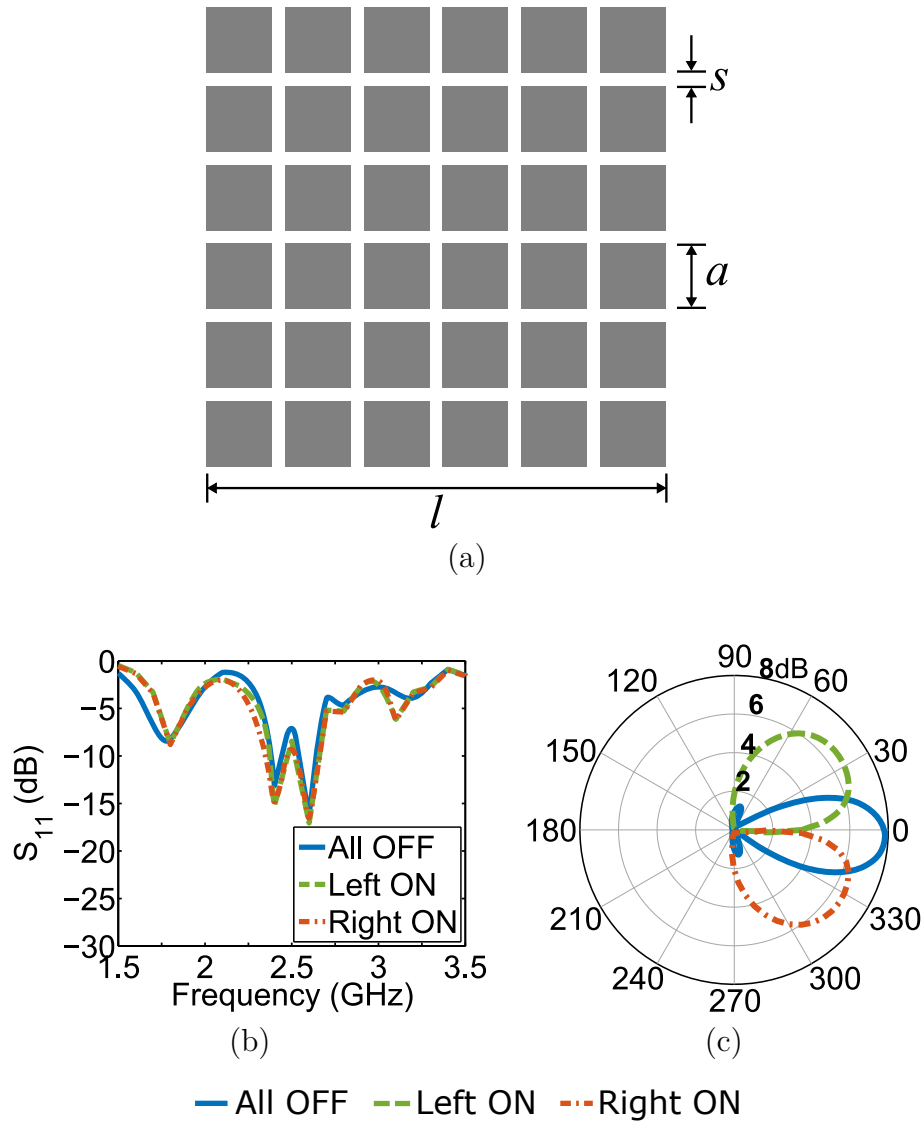


Figure 5.21 (a) Top view of a uniform EBG, (b) $|S_{11}|$ Vs. frequency, and (c) azimuth plane (xy) pattern.

at 2.4 GHz in the azimuth (XY) plane. The array can steer its beam in the azimuth plane at 0° , 30° , and 330° for three switching cases: all OFF (All OFF is needed in the presence of the EBG to direct the beam in the forward direction), Left ON and Right ON, respectively. The F/B is 12 dB. Peak gains are 8 and 6.7 dBi for all OFF and one (either Left or Right) ON, respectively.

5.5.2.2 Array on NUA EBG Surface

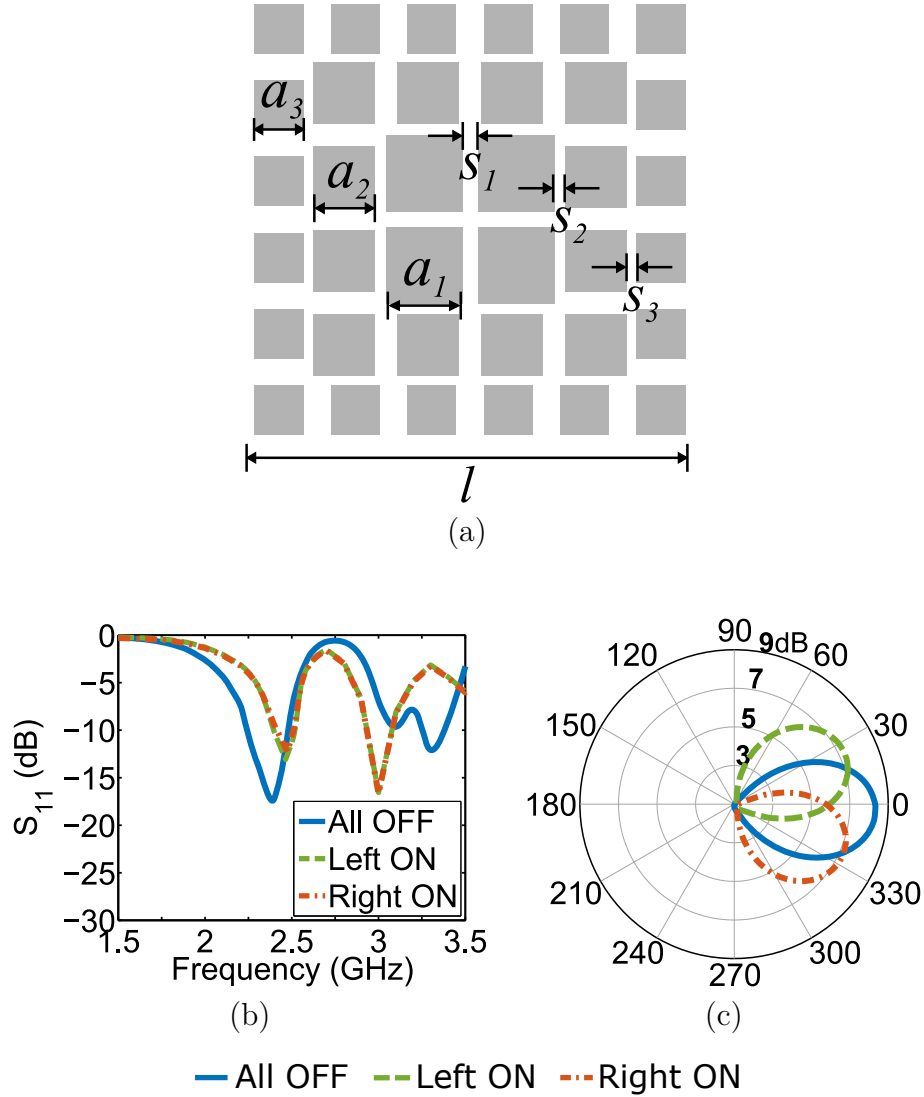


Figure 5.22 (a) Top view of a NUA EBG, (b) $|S_{11}|$ Vs. frequency, and (c) azimuth plane (xy) pattern.

In section 5.3.4, we proposed a non-uniform aperiodic (NUA) EBG surface. Here we have used a variant of that design where we omitted the metal vias. A beam steering array was placed on this NUA-EBG surface consisting of 6×6 square patches. The substrate used was TMM4. The top view of the array is shown in Fig. 5.22a. As before, parametric simulations were performed to optimize the array design. The minimum total thickness ($h + t$) for this case was found to be 5.4 mm ($\approx 0.04\lambda_0$).

This is more than 50% thickness reduction from the array above conductive ground with a TMM4 substrate. The geometrical parameters for this case were $a_1 = 14.4$ mm, $a_2 = 11.5$ mm, $a_3 = 9.2$ mm, $s_1 = 1.44$ mm, $s_2 = 1.15$ mm, $s_3 = 0.92$ mm, $h = 1.4$ mm, $t = 4.0$ mm, $l_d = 32.1$ mm, $l_p = 41.8$ mm, $w_d = w_p = 3.2$ mm, and $L = W = 75.8$ mm.

As seen in Fig. 5.22b, $|S_{11}| < -10$ dB is satisfied at 2.4 GHz for all three switching combinations. Fig. 5.22c shows that the array can steer its beam in the azimuth plane at 0° , 25° , and 335° for three switching combinations: all OFF, Left ON and Right ON respectively. The (F/B) is very high for this case, nearly 30 dB. Peak gain is 8.4 dBi when all switches are OFF and 7 dBi when only one switch is ON.

CHAPTER 6

LOW COST BIDIRECTIONAL SERIES-FED PHASED ARRAY FOR BODY-CENTRIC WIRELESS COMMUNICATIONS

6.1 INTRODUCTION

In recent years, high gain body wearable antennas are drawing attention of researchers as trans-receiving solution for first responders, astronauts, soldiers, and law enforcement personnel.

In Chapters 3, 4, and 5 we presented three switched beam parasitic antenna arrays. Although the arrays are low cost and efficient, they suffer from wide overlapping beams ($90^\circ - 120^\circ$). Traditional phased arrays can produce narrow beams but have large footprints making them unsuitable for wearable applications. As stated in section 2.4, a bidirectional series-fed phased array can be a good alternative.

In this chapter we present the design and development of a varactor controlled bidirectional series-fed array. Four series-connected driven dipoles and eight parasitic dipole elements form a high gain array where patterns are configured using a phase shifter that can add tunable progressive phases. The phase shifter is implemented using unequal line length couplers connected to varactor diodes. The ground plane of the phase shifter serves as a reflector which improves the directivity of the array, reduces RF exposure and isolates the antenna from the phase shifter and the bias network. By incorporating dc bypass lines within the microstrip feedline, the com-

plexity of implementing a biasing network is resolved making it possible to use a single bias tee to bias all varactors. The design frequency is selected to be 5.2 GHz but implementation at other frequencies is also possible.

6.2 PROPOSED ARRAY CONFIGURATION

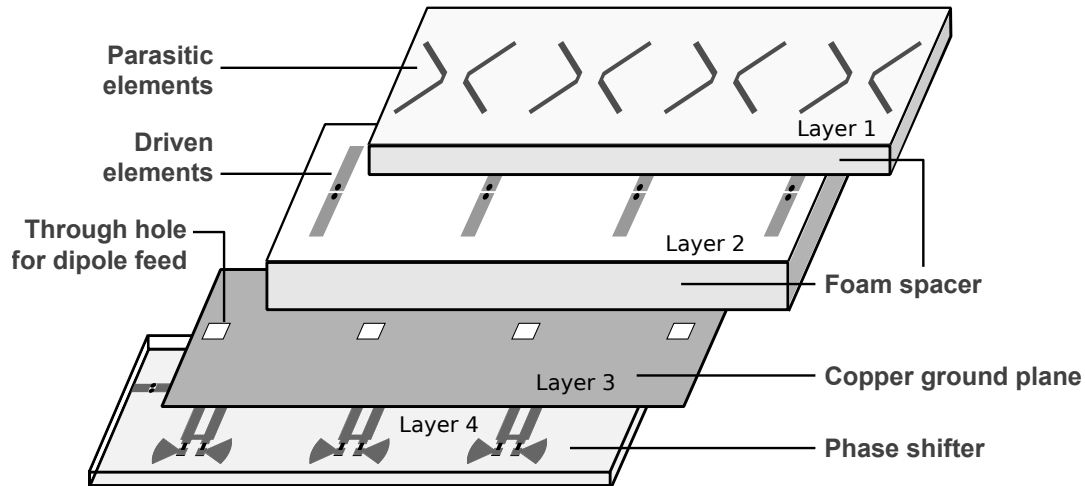


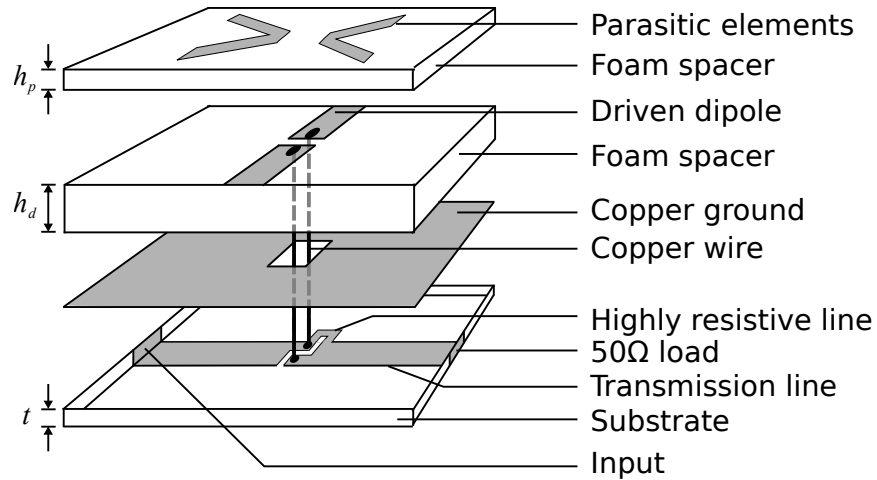
Figure 6.1 Array configuration.

The configuration of the proposed bidirectional series-fed antenna array is shown in Fig. 6.1. The entire antenna array consists of four layers. There are four sub-arrays interconnected with three phase shifters. Each subarray consists of two shorted parasitic v-dipoles and a driven dipole. The parasitics are located on the top layer, and the driven elements are on layer 2. These are constructed on two different substrate boards. Layer 3 and layer 4 can be constructed using a two sided substrate board where layer 3 is the ground plane, and the bottom layer or layer 4 contains the phase shifter network. Two vertical poles (cylindrical copper wires) from the feed region of the phase shifter goes through a hole in the ground and connects in the feed region of the dipole.

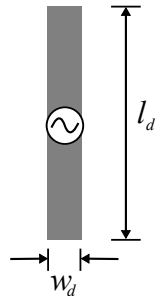
6.2.1 Parasitic Loaded Single Subarray

Fig. 6.2a shows the design of a single sub-array consisting of a driven dipole, two parasitic v-shaped shorted dipoles and a ground plane. This acts as a building block for the array. The length and width of the driven dipole, l_d and w_d are 18.4 mm and 2 mm respectively (Fig. 6.2b). On top of the driven element two v-shaped parasitic dipoles are placed on another foam spacer having thickness, h_p . The driven dipoles are placed on a foam spacer of thickness, h_d ; a copper ground plane resides underneath. Under the ground plane, there is a 0.64 mm thick Rogers[®] TMM4 substrate ($\epsilon_r = 4.5$, $\tan \delta = 0.001$), which has a 2.2 mm wide transmission line on its other side. This line creates a scope to connect phase shifters and other series elements which will be added later. There is a 0.3 mm wide tetris S (⌞) shaped gap in the transmission line. Two parallel copper wires each from one side of the gap connect the transmission line with the driven antenna feed region. The wires are 0.9 mm in diameter and separated by 0.4 mm. They pass through a rectangular hole in the ground plane to avoid contact. The transmission line has a 50Ω input at one edge and is terminated with a 50Ω matched load at the other edge. A 0.3 mm wide dc bypass line is added across the gap. This bypass line will be helpful later when we will add varactor based phase shifters, as they will be used to bias the varactors with a single bias tee.

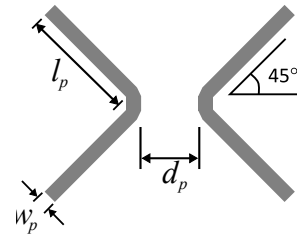
Parametric simulations were performed in Ansys HFSS to carefully select the distance between the driven element and the ground, h_d so that the antenna pattern is directional and return loss > 10 dB. The length (l_p) and width (w_p) of the v-shaped dipoles, the spacing between them (d_p), and the top foam spacer thickness, h_p are determined in such a way that the parasitic dipoles act as directors and maximum directivity is achieved for a minimum h_p . Based on the simulation results, $h_d = 6$ mm, $h_p = 2$ mm, $l_p = 11$ mm, $w_p = 1$ mm, and $d_p = 5.5$ mm were selected. As seen in Fig 6.2d the parasitic dipoles improve the $|S_{11}|$ from -7 dB to -12 dB at 5.2 GHz.



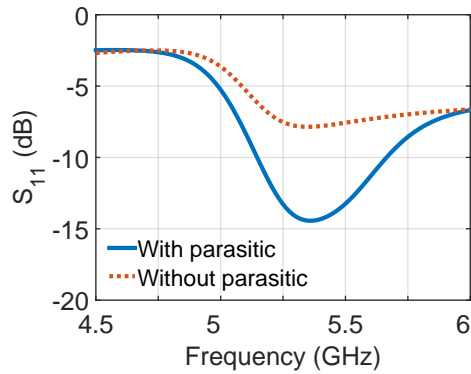
(a)



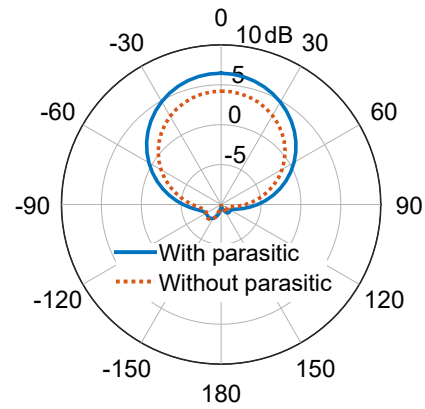
(b)



(c)



(d)



(e)

Figure 6.2 (a) Configuration of a single sub array, (b) dimensions of a single driven dipole, (c) dimensions of a parasitic element, (d) $|S_{11}|$ vs. frequency for the single subarray and (e) Realized gain pattern in the yz plane at 5.2 GHz.

The parasitic elements also enhance the gain by 2 dB which is apparent in Fig. 6.2e that shows the realized gain patterns in the yz plane at 5.2 GHz. For both cases,

with parasitic and without, the beam is directed to $\theta = 0^\circ$ and peak gains are 6.4 dBi and 4.2 dBi respectively.

6.2.2 Phased Array Formation

To examine the effect of progressive phase, HFSS simulations were conducted forming a four element array using the sub-array developed in the previous section. Fig. 6.3a shows the cross-sectional view of the formation.

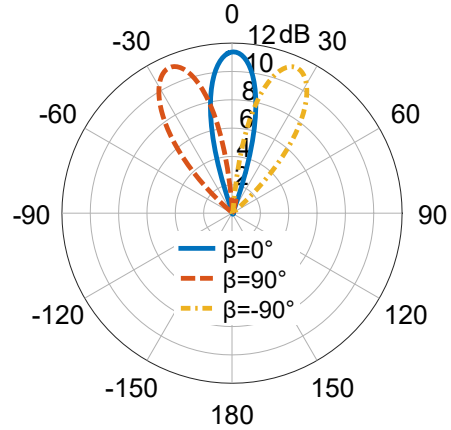
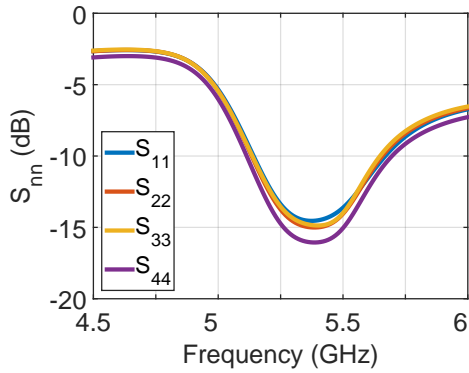
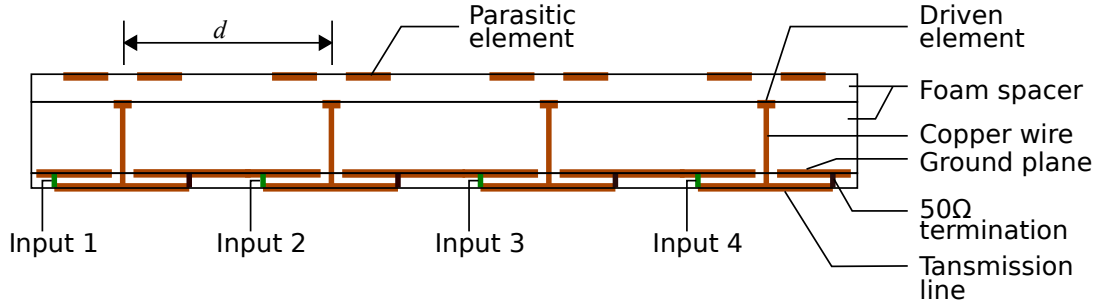


Figure 6.3 (a) Cross-sectional view (yz plane) of the array, (b) S_{nn} vs. frequency, and (c) realized gain pattern in yz plane at 5.2 GHz for three progressive phases.

The center to center distance, d between two consecutive subarrays is 33.8 mm. Total dimensions of the ground plane is $53.8 \times 145.8 \text{ mm}^2$. For this study each sub-

array has a separate input source (Fig. 6.3a) so that the progressive phase, β can be controlled independently for each port in HFSS. Simulated return losses, ($|S_{nn}|$) vs frequency at all ports are plotted in Fig. 6.3b. At 5.2 GHz, the $|S_{nn}|_{n=1,2,3,4} < -12$ dB. The 10-dB $|S_{nn}|$ bandwidth of this array is about 500 MHz as it operates from 5.12 GHz to 5.65 GHz.

Fig. 6.3c shows the simulated radiation pattern of the array in the yz plane for consecutive phase shifts of $\beta = 0^\circ, 90^\circ$ and -90° . As $d = 33.8$ mm and $\lambda = 57.7$ mm is known, one can calculate from the relation $\theta_m = -\sin^{-1}(\lambda\beta/2\pi d)$ that for $\beta = 0^\circ, 90^\circ$, and -90° , the maximum beams should occur at $\theta_m = 0^\circ, -25^\circ$, and 25° , respectively. This is in concordance with our observations from Fig. 6.3c. The peak realized gain of the array is 11.2 dBi for all the cases. In practice, to implement these progressive phases a shift shifter needs to be designed which is described in the next section.

6.2.3 Phase Shifter Design

Recently several authors [71, 164] have proposed phase shifters based on unequal line length coupler with reflective load. The phase shifter designed and implemented in this work was adapted from [164]. The schematic is shown in Fig. 6.4a.

The phase shifter was simulated on a 0.64 mm Rogers TMM4 substrate ($\epsilon_r = 4.5$, $\tan \delta = 0.001$) in Ansys HFSS. Fig. 6.4b shows an unequal line length coupler with its key parameters. The characteristic impedances Z_1 and Z_2 govern the width of their corresponding microstrip line-sections. Once the width is known, equivalent permittivity and hence the guided wavelength can be calculated which is used to find the lengths of the sections from the delays θ_1 and θ_2 . Equations (6.1) - (6.4) can be used to calculate these parameters. The design starts with choosing a power division ratio and finding the constant, k in Equation (6.1). Width (or the characteristic impedance) of one line is selected and the width of the other line can be determined

using Equation (6.2). Its parameters θ_1 and θ_2 can be computed from (6.3) and (6.4). In our design (Fig. 6.4a), the parameters w_3 , w_4 , l_c , and l_e were determined using these relations.

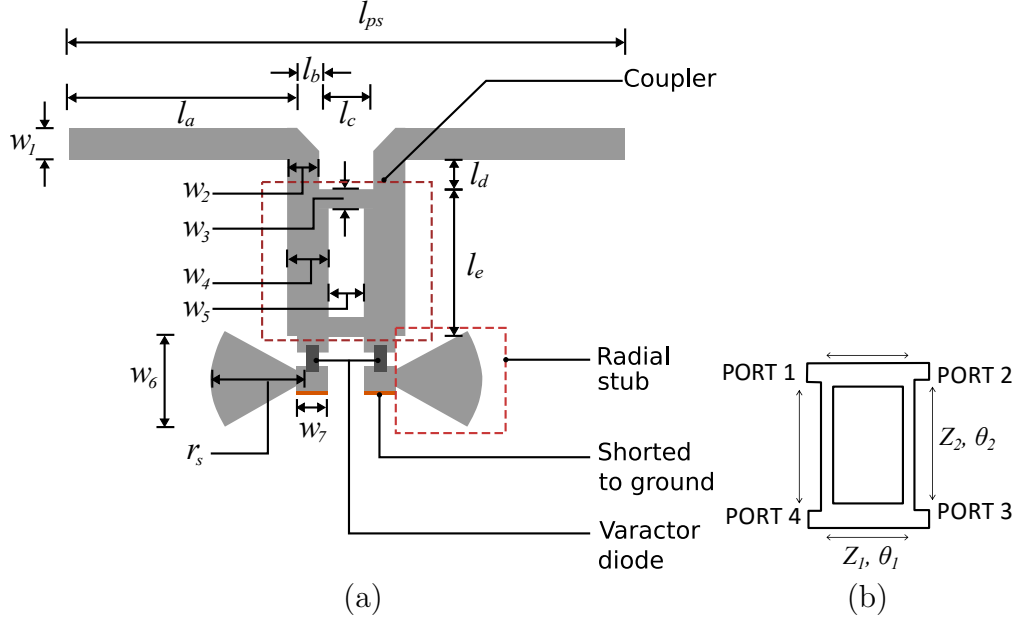


Figure 6.4 (a) Geometry of a single phase shifter and (b) an unequal length branchline coupler.

$$\left| \frac{S_{21}}{S_{31}} \right|^2 = \frac{k^2}{1 - k^2} \quad (6.1)$$

$$\frac{1}{Z_1^2} - \frac{1}{Z_2^2} = \frac{1}{Z_0^2} \quad (6.2)$$

$$Z_2 |\sin \theta_2| = Z_0 \frac{k}{\sqrt{1 - k^2}} \quad (6.3)$$

$$Z_1 \tan \theta_1 = -Z_2 \tan \theta_2 \quad (6.4)$$

As seen in 6.4a, the coupled port (port 3) and the isolated port (port 4) of the coupler are connected with radial stubs through varactor diodes. The radial stubs were designed following the guideline provided in [71]. The stubs are shorted to the ground plane as they ensure broader range of phase shift. The geometrical parameters of the phase shifter are listed in Table 6.1.

Table 6.1 Geometry parameters for the phase shifter (in mm).

Parameters	w_1	w_2	w_3	w_6	w_5	w_6	w_7
Values (mm)	2.24	1.9	1	2.5	2.5	7.83	1.9
Parameters	l_{ps}	l_a	l_b	l_c	l_d	l_e	r_s
Values (mm)	33.8	13.5	1.5	3.7	1.83	9	6

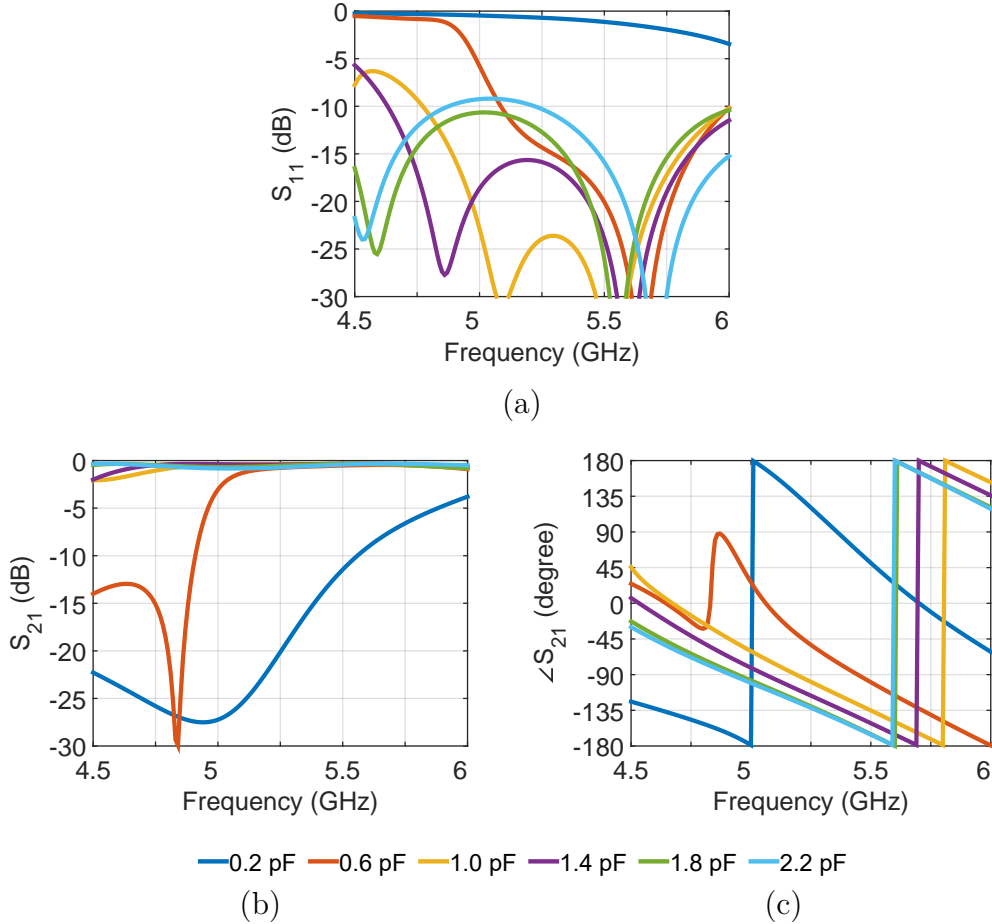


Figure 6.5 (a) S_{11} vs. frequency, (b) S_{21} vs. frequency, and (c) S_{11} phase vs. frequency for different capacitance values.

By varying the bias voltage, the varactor capacitance can be changed. This capacitance in tandem with the radial stubs change the load impedances at the coupled port (port 3 in Fig. 6.4) and the isolated port (port 4). This load impedance variation in ports 3 and 4, by the principle of branchline couplers, causes a phase shift between

port 1 and port 2 which is reflected in the S_{21} phase. In HFSS, the varactor diodes were modeled as ideal lumped element capacitors.

Return loss performance $|S_{11}|(\text{dB})$ vs frequency for different varactor capacitance values are plotted in Fig. 6.5a. The varactor capacitance, C is varied from 0.2 pF to 2.2 pF with 0.4 pF interval. It is observed that for $C < 0.6$ pF, the return loss is > -6 dB at 5.2 GHz. For higher capacitance values, $|S_{11}| < -10$ dB at 5.2 GHz.

Fig. 6.5b shows the simulated insertion loss performances vs frequency varying C from 0.2 pF to 2.2 pF with 0.4 pF interval. Again, for $C = 0.2, 0.6, 1.0, 1.4, 1.8,$ and 2.2 pF $|S_{21}|$ are -22, -0.9, -0.4, -0.4, and -0.6 dB, respectively. Therefore, higher capacitance values are suitable for our design due to low insertion loss. Fig. 6.5c shows the effect of capacitance values on S_{21} phases. As capacitance varies from 0.2 to 2.2 pF, S_{21} phase varies from 134° to -123° which suggests that around 250 degrees of phase shifting is possible with this shifter.

6.2.4 Bidirectional Series-fed Array

Next, a four element series fed array was modeled in HFSS including three phase shifters. The varactors were modeled as lumped capacitors. First the array was fed from left. Here the phrase ‘fed from left’ implies that port 1 is excited and port 2 is terminated with a matched load. Similarly, ‘fed from right’ implies that port 2 is excited and port 1 is terminated with a matched load.

In this study, three capacitance values were considered for the varactor: 0.6 pF, 1 pF, and 2.2 pF. The simulated S_{11} vs. freq. and the realized gain pattern in the yz plane at 5.2 GHz are shown in Fig. 6.6. From Fig. 6.6a we observe that $|S_{11}| < -10$ dB at 5.2 GHz for all three capacitance values. Fig. 6.6b shows the realized gain in the yz plane for $C = 2.2$ pF and $C = 0.6$ pF.

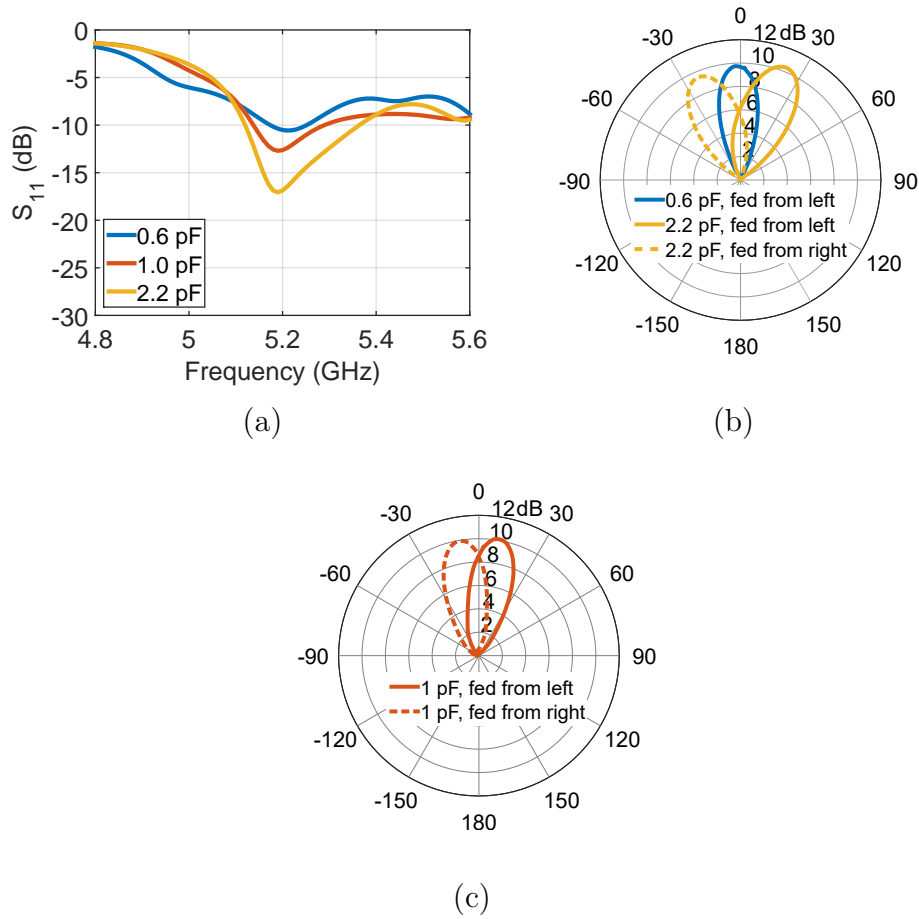


Figure 6.6 (a) S_{11} vs. frequency when the array was fed from Left side. (b) Realized gain patterns in the yz plane at 5.2 GHz for $C = 0.6$ pF and $C = 2.2$ pF, and (c) Realized gain patterns in the yz plane at 5.2 GHz for $C = 1$ pF.

With $C = 2.2$ pF, beam peak occurs at 25° and -25° when the array is fed from the left and the right, respectively. The half power beam width (HPBW) about 30° . The maximum gain is 10.2 dBi. For $C = 0.6$ pF, beam peak occurs at -2° when it is fed from the left. Fig. 6.6b shows the realized gain pattern for $C = 0.6$ pF. Beams are directed to $\theta = 10^\circ$ and $\theta = -10^\circ$, when the array is fed from the left and the right, respectively. The maximum gain is 10 dBi for these cases and the HPBW is 25° .

6.2.5 Array with Fabric Materials

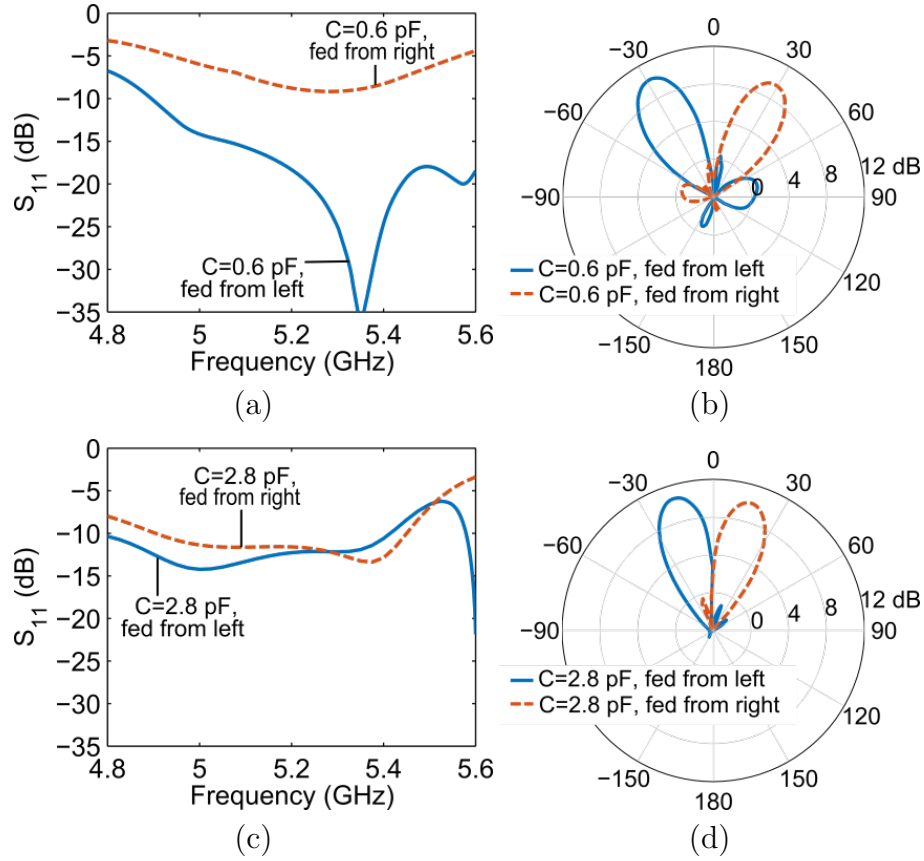


Figure 6.7 Simulation results for array on fabric substrate.

To consider wearable applications, a textile-based array was modelled and simulated. Instead of TMM4, a cotton substrate ($\epsilon_r = 1.6$, $\tan \delta = 0.001$) was used. The driven dipoles, parasitic dipoles, ground, and the phase shifters were modeled using copper taffeta (surface resistivity = $0.05 \Omega/\text{sq.}$)

Return loss and realized gain patterns at 5.2 GHz were studied for two different capacitance values: 0.6 pF and 2.8 pF. From Figs. 6.7a and 6.7b, we see that, for $C = 0.6$ pF, the return loss is near -10 dB and beam steering is possible at -30° and 30° . From Figs. 6.7c and 6.7d we see that, for $C = 2.8$ pF, beam peaks occur at -15° and 15° , when fed from left and right.

6.3 EXPERIMENTAL RESULTS

6.3.1 Fabrication of a Phase Shifter

Due to the easy and immediate availability of FR4, a phase shifter was built and tested using FR4. A photograph of the phase shifter is shown in Fig. 6.8a where two MA46H202 varactors were used. The radial stubs were shorted to the ground via thin copper wires. In Fig. 6.8b the measurement set up is shown, where port 1 of the Vector Network Analyzer (VNA) is connected with a Minicircuits bias tee (model: ZX85-12G-S+) and then connected with port 1 of the phase shifter. Port 2 of the shifter is directly connected to VNA port 2. The bias tee provides the required bias voltage for the varactor.

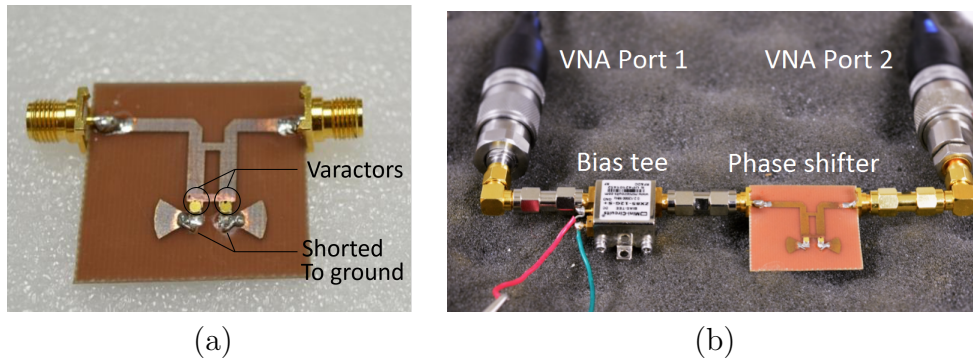


Figure 6.8 (a) Photograph of a fabricated phase shifter and (b) phase shifter measurement set up.

Fig. 6.9 shows the total capacitance vs reverse voltage response taken from the manufacturer's datasheet of the varactor. We observe that 1 pF capacitance can be obtained by applying a reverse bias voltage of around 12 V and 2.2 pF can be obtained with 5 V. These values will be used in the measurement. In the phase shifter measurement we are more concerned about the insertion loss and the phase difference between two ports which are quantified by S_{21} magnitude and phase. Nevertheless, it is important to make sure that the ports are matched so that the loss from reflection is minimal. Fig. 6.9a shows us that for 1 pF and 2.2 pF capacitances the S_{11} magnitude

is < -10 dB at 5.2 GHz, which is satisfactory. Similarly S_{22} magnitude was observed and found satisfactory.

In Fig. 6.9b measured insertion loss for bias voltages 12 V and 5 V are shown. In the measurement there was a 0.7 dB extra loss for the bias tee which has been de-embedded in these figures. We observe that for 12 V bias voltage (which is equivalent to varactor capacitance, $C = 1$ pF), the insertion loss is 2.4 dB at 5.2 GHz. In the simulation with 1 pF capacitor we have observed an insertion loss of 1.4 dB (see Fig. 6.9c, with $R_s=0 \Omega$), which is 1 dB less than what we observe in the measurement. This discrepancy can be explained using a series resistance which is mentioned in the equivalent circuit of the varactors provided by the manufacturer.

As the value of this series resistance, R_s was not specified in the device datasheet, we ignored it in the initial simulation. But R_s shows its effect when we measure the two-port S-parameter data. To study the effect of this series resistance, we performed a parametric simulation from $R_s = 0$ to 5Ω with 1Ω interval. Fig. 6.9d shows the simulated S_{21} of the phase shifter with variation of series resistance, R_s . For $R_s = 2 \Omega$ and 3Ω , insertion losses of 2.1 dB and 2.4 dB are observed. The 1 dB higher insertion loss in the measurement is likely due to the effect of this 3Ω resistance.

Fig. 6.9e shows the phase shifting behavior with the change of the bias voltage. We observe that for 12 V and 5 V bias voltages, the measured S_{21} phases at 5.2 GHz are 127° and 157° , respectively. The measured phase values do not directly agree with the simulation (-54° and -87° for 1 pF and 2.2 pF capacitances). This is because the measurement includes the phase from the bias tee. As the bias tee phase is the same for both cases, its effect can be canceled out if we consider the difference of S_{21} phases for 1 pF and 2.2 pF cases. One can calculate that the difference is 30° for measurement and 33° for simulation, which is in close agreement.

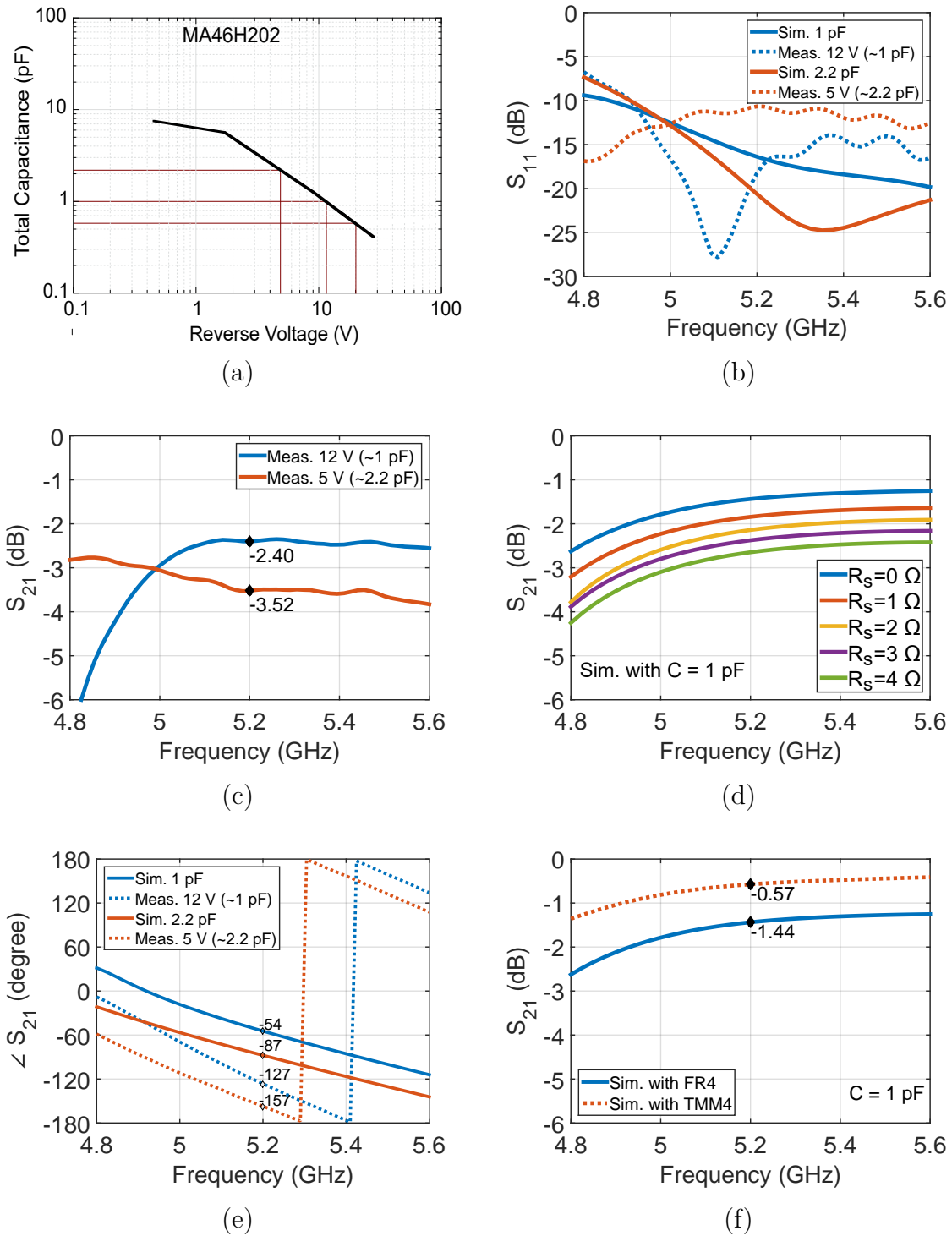


Figure 6.9 (a) Photograph of a fabricated phase shifter, (b) measured S_{11} , (c) measured S_{21} , and (d) measured S_{21} phase of the shifter.

On a related note, it should be noted that even with $R_s = 0 \Omega$ the 1.4 dB insertion

loss in each phase shifter can have detrimental effect on the total array gain. Bulk of this loss is due to the loss tangent of FR4 substrate ($\tan \delta = 0.02$), which can be reduced by using a low loss material such as TMM4 ($\tan \delta = 0.001$). In Fig. 6.9f the comparison of simulated $|S_{21}|$ between FR4 and TMM4 are shown. It is clear that the insertion loss for TMM4 is almost 1 dB less than that for FR4. This led us to switch from FR4 to TMM4 substrate for the entire array simulation and fabrication.

6.3.2 Array Fabrication and Return Loss Measurement

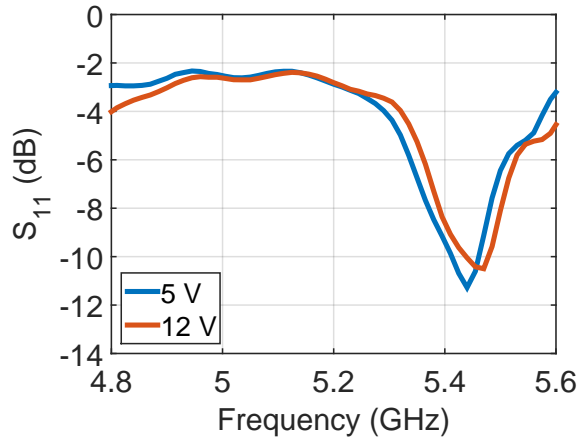
A prototype of the array shown in Fig. 6.1 was built using TMM4 substrate and measured for S parameters. Fig. 6.10a shows a photograph of the top layer of the array which contains the parasitic elements. The parasitic elements were made using flexible copper tapes and placed on a 2 mm thick Rohacell[®] foam spacer with an area of $34 \times 144 \text{ mm}^2$. The driven elements (not shown in photographs as they are concealed by the top layer) were also made using copper tapes and placed on a 6 mm thick Rohacell foam sheet. Layer 3 which contains the ground and layer 4 which has the phase shifter network (see Fig. 6.1) are built on the two sides of a 0.64 mm thick TMM4 substrate. Fig. 6.10b depicts the bottom layer (layer 4) of the array, from where a phase shifter network with three phase shifters can be seen. A total of six MA46H202 varactors (two for each shifter) were used which were connected to the phase shifter using conductive epoxy. Each phase shifter has two radial stubs which are shorted to the ground via 0.9 mm diameter copper wires. As seen in the figure, there are four feed regions in the phase shifter network. From each feed region two 0.9 mm diameter copper wires go through a hole in the ground, get across the foam spacer and connect with two arms of a driven dipole. For the experiment the left port was connected with a Minicircuits bias tee through an adapter and then connected with one port of the VNA. The right port was terminated with a standard 50Ω coaxial load.



(a)



(b)



(c)

Figure 6.10 Photograph of the (a) top layer of the array with parasitic elements and (b) bottom layer of the array containing the phase shifter network, and (c) measured $|S_{11}|$ vs. frequency for two different bias voltages.

As different bias voltages were applied shift in the S_{11} magnitude was observed. Fig. 6.10c shows the S_{11} vs frequency of the array for 5 V and 12 V bias voltages. Ideally these voltages should translate into varactor capacitances of 2.2 pF and 1

pF respectively. Comparing the measured S-parameter data with the simulated S-parameter data from Fig. 6.6a, it can be seen that the resonant frequency has shifted from 5.2 GHz to 5.4 GHz. The 10 dB bandwidth is ≈ 20 MHz. The minor shift can be attributed to imperfections in the fabrication process.

The driven and parasitic elements were manually cut from copper tapes where variation in length and width may have occurred. The wires that connect the phase shifter with the driven element should ideally be separated by 0.4 mm, but this separation could not be guaranteed during fabrication. In the simulation model there was no air gap between the two foam spacers or between the foam spacer and the ground plane. Practically it was not possible to ensure that. Also there might be some non-ideality in the substrate which could have caused the substrate dielectric constant to be different than the ideal value used in the simulation. The shift in frequency can be a combined effect of all these artifacts.

CHAPTER 7

CONCLUSION AND FUTURE WORK

7.1 CONCLUSION

In this dissertation, several innovative techniques to design high gain pattern reconfigurable antenna arrays for portable and wearable applications are presented. A comparative study among different methods for beam steering reveals that the traditional phased array technique is incompatible for portable handheld and body-worn array designing as it requires large space, long delay lines, and complicated bias networks. The switched beam parasitic array is a viable approach where very small antenna volumes are available. Cases where moderate amount of space is available, varactor controlled series-fed arrays are attractive because they can provide narrow beamwidth in the steering plane allowing well defined nulls between consecutive patterns. The series-fed array is more appropriate for wearable applications. Below are the principal conclusions.

First, using the switched beam parasitic array technique, a 4-subarray collinear pattern reconfigurable smart antenna array was designed, developed and tested validating performance. Simulation results in both free-space and on FR4 show that the array operates at around 5 GHz with better than 10 dB return loss and better than 17 dB mutual coupling. For the FR4 array, the peak gain is between 9.7-11 dBi for the three different reconfiguration angles, e.g. 0, 70 and 290 degrees. Experimental fabrication and tests show that the array meets the input $|S_{nn}|$ and $|S_{mn}|$ characteristics of <-10 dB and <-15 dB, respectively. Measured pattern results show

the pattern reconfiguration in three different angles in the azimuth albeit with some degradation due to the presence of long DC bias wires. Measured peak gain is about 1 dB lower than the simulated gain. The reflections and distortions in the pattern can be largely eliminated by the use of lumped element baluns and dc bias traces made from materials with high sheet resistance ($>500 \Omega/\text{square}$ for instance) as opposed to standard copper wires. However, in that case instead of PIN diodes that are current (mA) controlled varactor diodes or RF MEMS switches should be used that almost conducts no current ($<nA$). Finally, when the radiation properties and gain results were used in system level simulations it was found that the high-gain pattern reconfigurable antenna array provided 59% increase in SINR over an omnidirectional antenna.

Next, a high-gain collinear MIMO antenna array design is presented for body-worn wireless application. For three switching states the array beam directions can be steered into three different directions. Array performance for various conductive and nonconductive fabric materials is investigated. Array on a curvature and array near a phantom are studied. The half-power beamwidth is very narrow in the elevation plane (approximately 20°). The array gain is 12.3 dBi for a 4 sub-array embodiment near a phantom. The experimental data with loss tangent measurement is presented.

Then, the concept of a Non-Uniform Aperiodic (NUA) metasurface is studied in the context of achieving broad dipole antenna bandwidth while the total structure thickness is kept less than $0.05\lambda_0$. The frequency range selected is the UHF frequency band because there are many commercial and military applications that may benefit from the outcomes of this research. Starting from a scaled design of a strip dipole on a uniform mushroom EBG structure, the study progressed into tapered metasurface structures that focused on both increasing and decreasing tapers. In either case, the total volume of the metasurface was kept constant as that of the uniform EBG but the individual patch dimensions and their interelement spacing were varied according to a

percent taper. This was inspired by the principles of broadband impedance matching using multisection quarter wave transformers with differing (tapered) characteristic impedances. Except for our case, the dipole is the illuminating source that needed to be matched to the EBG surface underneath it.

It was observed that with an increasing taper i.e. when the metasurface started with smaller patch sizes and interelement distances at the center and then grew radially outward, the outcome was not desirable meaning that dipole antenna bandwidth actually degraded. Conversely, when the metasurface started with larger patch sizes and interelement distances at the center and then decreased radially, the outcome was broad dipole antenna bandwidth. An experimental prototype fabricated and tested clearly show that the proposed metasurface plus antenna concept can provide one octave pattern and gain bandwidth with a total thickness of $0.05\lambda_0$. This was achieved without any magnetic material loading or frequency reconfiguration using electronic devices. Using a scaled and refined version of the NUA EBG surface designed for UHF range, a thin high-gain EBG-based pattern reconfigurable array design is presented for 2.4 GHz wireless application. The effects of array thickness on its performance are investigated and the thickness limits have been determined for several types of reflectors. With a non-uniform planar EBG structure the array thickness can be reduced by more 50% of that of an array on conductive ground plane. With a thickness of only $0.04\lambda_0$, the array can steer its beam in three distinct directions in the azimuth plane. The array peak gain is 8.4 dBi, average beamwidth is 60° and F/B is 30 dB.

Finally, the design of a varactor controlled bidirectional series-fed array is presented. A phase shifter was designed with varactor controlled unequal line length branchline coupler. Simulation data show beam steering from -25° to 25° with 10.2 dBi peak gain. The array beamwidth in the steering plane is narrow: $25^\circ - 30^\circ$. A fabric based design was presented which can be integrated with clothing of emergency personnel. Experimental results show promises for the applicability of the

phase shifter.

7.2 FUTURE WORK

The beam steering MIMO array for handheld devices investigated in Chapter 3 contains four subarrays. By increasing the number of subarrays, higher gain and lower elevation plane beamwidth can be obtained. The array can be made more compact by following multiple strategies such as using folded dipoles as driven elements, using dielectric filler materials inside the cavity of the array, optimizing antenna element dimensions using advanced algorithms such as genetic algorithm, particle swarm optimization, etc. The losses in array gain and deviation in pattern can be reduced by adopting some useful techniques such as building the antenna elements on low-loss substrates, using lumped element baluns, making dc bias traces from materials with high sheet resistance which would reduce field interaction with bias network, and by using voltage controlled devices such as varactor diodes, MEMS switches, or Field Effect Transistors (FET) as they draw minimal current, have very low insertion loss and high isolation. For this array, performance near human body was not studied in our work. This can be a very important future work.

In Chapter 4, array design and optimization were performed using simulation tool. Building full-scale prototypes of the array using several fabric materials and measuring their S parameters, gain and patterns would be the next step to do. Array fabrication with fabric materials requires several important aspects to be taken into consideration. Attaching fabric layers need to be done carefully with glue or stitching, as accumulation of glue can change dielectric property of fabric by introducing heterogeneity and stitching can cause the antenna and ground layer to be shorted with by pulling conductive threads. [109]. Circuit components needs to be connected with fabrics using conductive epoxy as fabric thread might not withhold high temperatures while soldering. To secure the circuit from getting damaged by bending and washing,

the bias circuits and baluns should be covered with a non-conductive silicone-based epoxy. The fabric based array is supposed to be worn on the body which has its own curves at different locations. For example, the back is almost flat (radius of curvature around 160-200 mm) where the wrist is cylindrical (radius of curvature ≈ 25 -80 mm). These curvatures might change the effective length of the antenna and a frequency shift and gain degradation might occur. Also, the curvatures might be changed for different postures of the human body. Once fabricated, the flexible antenna can be measured by placing it on different parts of the human body for different postures, to observe the effect of curvature. The effect of humidity can be investigated by placing the array in a controlled humidity chamber and measuring its performance. Robustness of the antenna can be analyzed by measuring its parameter after exposing it to extreme conditions such as very high and low temperatures, or placing it in a washing machine. The SAR performance of the array in proximity to human body can be studied experimentally.

In Chapter 5, first we have presented a wideband antenna-EBG system for UHF band. Future research on this topic should focus on the development of the systematic theory and design guidelines for broadband metasurface. Instead of simple geometrical progression, more complex profiling such as binomial distribution can be investigated for tapering. Lightweight antenna-EBG systems can be designed and built using high dielectric thin substrates. Later in Chapter 5, a switched beam parasitic array was proposed above the NUA EBG surface based on simulation results. Further numerical studies can be performed incorporating more directors to find if the array gain can be enhanced and array beams can be further reconfigured. The preliminary simulation model has a single driven element. Similar to the arrays presented in Chapters 3 and 4, a collinear arrangement can be made with multiple subarrays and thus the gain can be enhanced more. The array with EBG can be modeled with conductive and non-conductive fabric materials and thus a flexible array-EBG system

can be developed for wearable applications. Prototype of the antenna-EBG system can be fabricated and measured for S parameter, gain, and radiation pattern.

The series fed array proposed in Chapter 6 was built on a rigid TMM4 substrate with foam spacers. Flexible arrays can be designed by using fabric materials. As it is a series fed array where there is a phase shifter between every two driven element input, the current magnitude gets tapered in driven antenna inputs as it flows from input to load. It means that if there are many subarrays, little or no radiation will be generated by the last driven element. This poses a restriction in the number of subarrays which can be analyzed through detailed analytical or numerical studies. Further optimization of the array can be performed using advanced algorithms. The array can be modeled near human body phantom to observe SAR performance. For operation at mm-wave frequencies such as 38, 60 GHz, varactor devices, bias network, and antenna elements can be monolithically designed together on a single substrate.

The concepts presented in this dissertation can be extended to design circularly polarized beam steering antenna arrays using cross dipole elements which will be useful for applications such as GPS, satellite phone etc. Finally, the two techniques namely, the switched beam parasitic arrays and varactor controlled series-fed phased arrays can be combined together to achieve beam steering with narrow beams and defined nulls simultaneously in both azimuth and elevation planes.

BIBLIOGRAPHY

- [1] “Samsung 5G vision.” Available online: <http://www.samsung.com/global/business-images/insights/2015/Samsung-5G-Vision-2.pdf>. Accessed: 2016-07-11.
- [2] A. Diallo, C. Luxey, P. Le Thuc, R. Staraj, and G. Kossiavas, “Study and Reduction of the Mutual Coupling Between Two Mobile Phone PIFAs Operating in the DCS1800 and UMTS Bands,” *IEEE Transactions on Antennas and Propagation*, vol. 54, pp. 3063–3074, Nov. 2006.
- [3] Y. J. Ren, “Ceramic Based Small LTE MIMO Handset Antenna,” *IEEE Transactions on Antennas and Propagation*, vol. 61, pp. 934–938, Feb. 2013.
- [4] H. T. Chattha, M. Nasir, Q. H. Abbasi, Y. Huang, and S. S. AlJa’afreh, “Compact Low-Profile Dual-Port Single Wideband Planar Inverted-F MIMO Antenna,” *IEEE Antennas and Wireless Propagation Letters*, vol. 12, pp. 1673–1675, 2013.
- [5] J. Park, J. Choi, J. Y. Park, and Y. S. Kim, “Study of a T-Shaped Slot With a Capacitor for High Isolation Between MIMO Antennas,” *IEEE Antennas and Wireless Propagation Letters*, vol. 11, pp. 1541–1544, 2012.
- [6] R. Karimian, H. Oraizi, S. Fakhte, and M. Farahani, “Novel F-Shaped Quad-Band Printed Slot Antenna for WLAN and WiMAX MIMO Systems,” *IEEE Antennas and Wireless Propagation Letters*, vol. 12, pp. 405–408, 2013.
- [7] N. Herscovici, C. Christodoulou, E. Rajo-Iglesias, O. Quevedo-Teruel, and M. Sanchez-Fernandez, “Compact Multimode Patch Antennas for MIMO Applications [Wireless Corner],” *IEEE Antennas and Propagation Magazine*, vol. 50, pp. 197–205, Apr. 2008.
- [8] H. Zhang, Z. Wang, J. Yu, and J. Huang, “A compact MIMO antenna for wireless communication,” *IEEE Antennas and Propagation Magazine*, vol. 50, pp. 104–107, Dec. 2008.
- [9] P. Vainikainen, J. Holopainen, and M. Kyro, “Antennas for Digital Television Receivers in Mobile Terminals,” *Proceedings of the IEEE*, vol. 100, pp. 2341–

2348, July 2012.

- [10] M. S. Sharawi, A. B. Numan, M. U. Khan, and D. N. Aloï, "A Dual-Element Dual-Band MIMO Antenna System With Enhanced Isolation for Mobile Terminals," *IEEE Antennas and Wireless Propagation Letters*, vol. 11, pp. 1006–1009, 2012.
- [11] M. S. Sharawi, M. U. Khan, A. B. Numan, and D. N. Aloï, "A CSRR Loaded MIMO Antenna System for ISM Band Operation," *IEEE Transactions on Antennas and Propagation*, vol. 61, pp. 4265–4274, Aug. 2013.
- [12] S. H. Kim, J. Y. Lee, T. T. Nguyen, and J. H. Jang, "High-Performance MIMO Antenna With 1-D EBG Ground Structures for Handset Application," *IEEE Antennas and Wireless Propagation Letters*, vol. 12, pp. 1468–1471, 2013.
- [13] J. M. Lee, K. B. Kim, H. K. Ryu, and J. M. Woo, "A Compact Ultrawideband MIMO Antenna With WLAN Band-Rejected Operation for Mobile Devices," *IEEE Antennas and Wireless Propagation Letters*, vol. 11, pp. 990–993, 2012.
- [14] J. F. Li, Q. X. Chu, and T. G. Huang, "A Compact Wideband MIMO Antenna With Two Novel Bent Slits," *IEEE Transactions on Antennas and Propagation*, vol. 60, pp. 482–489, Feb. 2012.
- [15] D. A. Ketzaki and T. V. Yioultis, "Metamaterial-Based Design of Planar Compact MIMO Monopoles," *IEEE Transactions on Antennas and Propagation*, vol. 61, pp. 2758–2766, May 2013.
- [16] L. Liu, S. W. Cheung, and T. I. Yuk, "Compact MIMO Antenna for Portable Devices in UWB Applications," *IEEE Transactions on Antennas and Propagation*, vol. 61, pp. 4257–4264, Aug. 2013.
- [17] J. F. Li, Q. X. Chu, Z. H. Li, and X. X. Xia, "Compact Dual Band-Notched UWB MIMO Antenna With High Isolation," *IEEE Transactions on Antennas and Propagation*, vol. 61, pp. 4759–4766, Sept. 2013.
- [18] X. Zhou, X. Quan, and R. Li, "A Dual-Broadband MIMO Antenna System for GSM/UMTS/LTE and WLAN Handsets," *IEEE Antennas and Wireless Propagation Letters*, vol. 11, pp. 551–554, 2012.
- [19] S. C. Fernandez and S. K. Sharma, "Multiband Printed Meandered Loop Antennas With MIMO Implementations for Wireless Routers," *IEEE Antennas*

and *Wireless Propagation Letters*, vol. 12, pp. 96–99, 2013.

- [20] A. Krewski, W. L. Schroeder, and K. Solbach, “2-Port DL-MIMO Antenna Design for LTE-Enabled USB Dongles,” *IEEE Antennas and Wireless Propagation Letters*, vol. 12, pp. 1436–1439, 2013.
- [21] C. G. Christodoulou, Y. Tawk, S. A. Lane, and S. R. Erwin, “Reconfigurable Antennas for Wireless and Space Applications,” *Proceedings of the IEEE*, vol. 100, pp. 2250–2261, July 2012.
- [22] Y. Zhou, R. S. Adve, and S. V. Hum, “Design and Evaluation of Pattern Reconfigurable Antennas for MIMO Applications,” *IEEE Transactions on Antennas and Propagation*, vol. 62, pp. 1084–1092, Mar. 2014.
- [23] I. Locher, M. Klemm, T. Kirstein, and G. Trster, “Design and Characterization of Purely Textile Patch Antennas,” *IEEE Transactions on Advanced Packaging*, vol. 29, pp. 777–788, Nov. 2006.
- [24] M. Grilo and F. Salete Correra, “Parametric study of rectangular patch antenna using denim textile material,” in *Microwave Optoelectronics Conference (IMOC), 2013 SBMO/IEEE MTT-S International*, pp. 1–5, Aug. 2013.
- [25] Y. Senbokuya and H. Tsunoda, “A study on the circular patch antennas using conductive non-woven fiber fabrics,” in *IEEE Antennas and Propagation Society International Symposium, 2002*, vol. 1, pp. 782–784 vol.1, 2002.
- [26] S. Sankaralingam and B. Gupta, “A textile antenna for WLAN applications,” in *International Conference on Emerging Trends in Electronic and Photonic Devices Systems, 2009. ELECTRO '09*, pp. 391–394, Dec. 2009.
- [27] K. Kwon, J. Tak, and J. Choi, “A practical study of textile TM₀₁ mode circular patch antenna for wireless body area network applications,” in *2014 International Conference on Electronics, Information and Communications (ICEIC)*, pp. 1–2, Jan. 2014.
- [28] F. Declercq, A. Georgiadis, and H. Rogier, “Wearable aperture-coupled shorted solar patch antenna for remote tracking and monitoring applications,” in *Proceedings of the 5th European Conference on Antennas and Propagation (EU-CAP)*, pp. 2992–2996, Apr. 2011.
- [29] C. Hertleer, A. Tronquo, H. Rogier, L. Vallozzi, and L. Van Langenhove,

- “Aperture-Coupled Patch Antenna for Integration Into Wearable Textile Systems,” *Antennas and Wireless Propagation Letters*, vol. 6, no. 11, pp. 392–395, 2007.
- [30] T. Kennedy, P. Fink, A. Chu, N. Champagne, G. Lin, and M. Khayat, “Body-Worn E-Textile Antennas: The Good, the Low-Mass, and the Conformal,” *IEEE Transactions on Antennas and Propagation*, vol. 57, pp. 910–918, Apr. 2009.
- [31] P. Salonen, M. Keskilammi, J. Rantanen, and L. Sydanheimo, “A novel Bluetooth antenna on flexible substrate for smart clothing,” in *2001 IEEE International Conference on Systems, Man, and Cybernetics*, vol. 2, pp. 789–794 vol.2, 2001.
- [32] C. H. Lin, Z. Li, K. Ito, M. Takahashi, and K. Saito, “A small tunable and wearable planar inverted-F antenna (PIFA),” in *2012 6th European Conference on Antennas and Propagation (EUCAP)*, pp. 742–745, Mar. 2012.
- [33] C. Cibin, P. Leuchtman, M. Gimersky, R. Vahldieck, and S. Mosciroda, “A flexible wearable antenna,” in *IEEE Antennas and Propagation Society International Symposium, 2004*, vol. 4, pp. 3589–3592 Vol.4, June 2004.
- [34] P. J. Soh, G. A. E. Vandenbosch, S. L. Ooi, and N. H. M. Rais, “Design of a Broadband All-Textile Slotted PIFA,” *IEEE Transactions on Antennas and Propagation*, vol. 60, pp. 379–384, Jan. 2012.
- [35] J.-S. Roh, Y.-S. Chi, J.-H. Lee, Y. Tak, S. Nam, and T. J. Kang, “Embroidered Wearable Multiresonant Folded Dipole Antenna for FM Reception,” *IEEE Antennas and Wireless Propagation Letters*, vol. 9, pp. 803–806, 2010.
- [36] T. Kellomaki, J. Heikkinen, and M. Kivikoski, “Wearable antennas for FM reception,” in *First European Conference on Antennas and Propagation, 2006. EuCAP 2006*, pp. 1–6, Nov. 2006.
- [37] S. Kumari, V. Gupta, A. Agarwal, A. Kumar, and A. Raj, “Microstrip loop antenna for wearable applications,” in *2012 1st International Conference on Recent Advances in Information Technology (RAIT)*, pp. 813–815, Mar. 2012.
- [38] T. Maleszka and P. Kabacik, “Bandwidth properties of embroidered loop antenna for wearable applications,” in *Wireless Technology Conference (EuWIT), 2010 European*, pp. 89–92, Sept. 2010.

- [39] T. Watanabe and H. Iwasaki, "Wearable Finger dual band antenna for BAN," in *2012 IEEE-APS Topical Conference on Antennas and Propagation in Wireless Communications (APWC)*, pp. 51–54, Sept. 2012.
- [40] C. Vigneshwaran, Z. C. Alex, and K. Shambavi, "Design and analysis of spiral wearable antenna," in *2014 International Conference on Green Computing Communication and Electrical Engineering (ICGCCEE)*, pp. 1–4, Mar. 2014.
- [41] H. Lee, M. M. Tentzeris, and J. Geiger, "Flexible spiral antenna with microstrip tapered infinite balun for wearable applications," in *Proceedings of the 2012 IEEE International Symposium on Antennas and Propagation*, pp. 1–2, July 2012.
- [42] M. Ur-Rehman, Q. Abbasi, M. Kamran, and X. Yang, "Design of a compact wearable single-arm spiral antenna for satellite communications," in *RF and Microwave Conference (RFM), 2013 IEEE International*, pp. 318–321, Dec. 2013.
- [43] H. J. Visser and A. C. F. Reniers, "Textile Antennas, a Practical Approach," in *The Second European Conference on Antennas and Propagation, 2007. EuCAP 2007*, pp. 1–8, Nov. 2007.
- [44] S. Bashir, M. Hosseini, R. Edwards, M. Khattak, and L. Ma, "Bicep mounted low profile wearable antenna based on a non-uniform EBG ground plane - flexible EBG inverted-l (FEBGIL) antenna," in *Antennas and Propagation Conference, 2008. LAPC 2008. Loughborough*, pp. 333–336, Mar. 2008.
- [45] S. Velan, E. Sundarsingh, M. Kanagasabai, A. Sharma, C. Raviteja, R. Sivasamy, and J. Kizhekke pakkathillam, "Dual-Band EBG Integrated Monopole Antenna Deploying Fractal Geometry for Wearable Applications," *IEEE Antennas and Wireless Propagation Letters*, vol. PP, no. 99, pp. 1–1, 2014.
- [46] S. Kim, Y. J. Ren, H. Lee, A. Rida, S. Nikolaou, and M. M. Tentzeris, "Monopole Antenna With Inkjet-Printed EBG Array on Paper Substrate for Wearable Applications," *IEEE Antennas and Wireless Propagation Letters*, vol. 11, pp. 663–666, 2012.
- [47] Z. Duan, D. Linton, W. Scanlon, and G. Conway, "Improving wearable slot antenna performance with EBG structures," in *Antennas and Propagation Conference, 2008. LAPC 2008. Loughborough*, pp. 173–176, Mar. 2008.

- [48] S. Zhu and R. Langley, "Dual-Band Wearable Textile Antenna on an EBG Substrate," *IEEE Transactions on Antennas and Propagation*, vol. 57, pp. 926–935, Apr. 2009.
- [49] J. Vardaxoglou, R. M. Edwards, A. Chauraya, and S. Bashir, "Compact and flexible surfaces using electromagnetic band gap (EBG)," in *Proceedings of the Fourth European Conference on Antennas and Propagation*, pp. 1–4, Apr. 2010.
- [50] S. Bashir, A. Chauraya, R. Edwards, and J. Vardaxoglou, "A flexible fabric metasurface for on body communication applications," in *Antennas Propagation Conference, 2009. LAPC 2009. Loughborough*, pp. 725–728, Nov. 2009.
- [51] N. Chahat, M. Zhadobov, R. Sauleau, and K. Mahdjoubi, "Improvement of the on-body performance of a dual-band textile antenna using an EBG structure," in *Antennas and Propagation Conference (LAPC), 2010 Loughborough*, pp. 465–468, Nov. 2010.
- [52] J. S. Colburn, Y. Rahmat-Samii, M. A. Jensen, and G. J. Pottie, "Evaluation of personal communications dual-antenna handset diversity performance," *IEEE Transactions on Vehicular Technology*, vol. 47, pp. 737–746, Aug. 1998.
- [53] M. G. Douglas, M. Okoniewski, and M. A. Stuchly, "A planar diversity antenna for handheld PCS devices," *IEEE Transactions on Vehicular Technology*, vol. 47, pp. 747–754, Aug. 1998.
- [54] B. M. Green and M. A. Jensen, "Diversity performance of dual-antenna handsets near operator tissue," *IEEE Transactions on Antennas and Propagation*, vol. 48, pp. 1017–1024, July 2000.
- [55] S. C. K. Ko and R. D. Murch, "Compact integrated diversity antenna for wireless communications," *IEEE Transactions on Antennas and Propagation*, vol. 49, pp. 954–960, June 2001.
- [56] C. B. Dietrich, K. Dietze, J. R. Nealy, and W. L. Stutzman, "Spatial, polarization, and pattern diversity for wireless handheld terminals," *IEEE Transactions on Antennas and Propagation*, vol. 49, pp. 1271–1281, Sept. 2001.
- [57] Y. Ding, Z. Du, K. Gong, and Z. Feng, "A Novel Dual-Band Printed Diversity Antenna for Mobile Terminals," *IEEE Transactions on Antennas and Propagation*, vol. 55, pp. 2088–2096, July 2007.

- [58] M. Z. Azad and M. Ali, "A New Class of Miniature Embedded Inverted-F Antennas (IFAs) for 2.4 GHz WLAN Application," *IEEE Transactions on Antennas and Propagation*, vol. 54, pp. 2585–2592, Sept. 2006.
- [59] A. T. M. Sayem, S. Khan, and M. Ali, "A Miniature Spiral Diversity Antenna System With High Overall Gain Coverage and Low SAR," *IEEE Antennas and Wireless Propagation Letters*, vol. 8, pp. 49–52, 2009.
- [60] D. Ehyaie, *Novel Approaches to the Design of Phased Array Antennas*. PhD Dissertation, University of Michigan, Ann Arbor, 2011.
- [61] J. H. Winters, "Smart antennas for wireless systems," *IEEE Personal Communications*, vol. 5, pp. 23–27, Feb. 1998.
- [62] N. H. Chamok and M. Ali, "A 5 ghz beam steering array for portable wireless mimo application," in *2014 IEEE Antennas and Propagation Society International Symposium (APSURSI)*, 2014.
- [63] N. H. Chamok, M. Yilmaz, H. Arslan, and M. Ali, "High-Gain Pattern Reconfigurable MIMO Antenna Array for Wireless Handheld Terminals," *IEEE Transactions on Antennas and Propagation*, 2016.
- [64] M. Ali and N. H. Chamok, "Beam Steering High Gain MIMO Antenna Array for Handheld Wireless Terminals," *USC IP Office, USC- 1114, US Provisional patent application number: 61/998,513*, 2014.
- [65] N. H. Chamok and M. Ali, "A high-gain beam steering fabric-based array for body-worn wireless applications," in *2015 IEEE International Symposium on Antennas and Propagation USNC/URSI National Radio Science Meeting*, pp. 2221–2222, July 2015.
- [66] M. Ali and N. H. Chamok, "Wearable High-Gain Beam-Steering E-Textile Antenna Array," *USC IP Office, USC- 1114, US Provisional patent application number: 61/998,513*, 2014.
- [67] N. H. Chamok, M. Ali, and S. Weiss, "A broadband UHF antenna on a non-uniform aperiodic (NUA) EBG surface," in *2013 IEEE Antennas and Propagation Society International Symposium (APSURSI)*, pp. 268–269, July 2013.
- [68] N. H. Chamok, M. Ali, T. Anthony, and S. J. Weiss, "Ultra-Thin UHF Broadband Antenna on a Non-Uniform Aperiodic (NUA) MetaSurface," *IEEE An-*

tennas and Propagation Magazine, vol. 57, pp. 167–180, April 2015.

- [69] N. H. Chamok and M. Ali, “Broadband directional antenna on an EBG structure for body-centric wireless communication,” in *Applied Computational Electromagnetics (ACES), 2015 31st International Review of Progress in*, pp. 1–2, March 2015.
- [70] N. H. Chamok and M. Ali, “A thin switched beam parasitic antenna array on planar EBG for 2.4 GHz wireless application,” in *2016 IEEE International Symposium on Antennas and Propagation USNC/URSI National Radio Science Meeting*, June 2016.
- [71] S. Cheng, E. Ojefors, P. Hallbjorner, and A. Rydberg, “Compact reflective microstrip phase shifter for traveling wave antenna applications,” *IEEE Microwave and Wireless Components Letters*, vol. 16, pp. 431–433, July 2006.
- [72] C. A. Balanis, *Antenna theory: analysis and design*. John Wiley & Sons, 2016.
- [73] H. Yagi, “Beam transmission of ultra short waves,” *Proceedings of the IEEE*, vol. 85, pp. 1864–1874, Nov 1997.
- [74] S. Uda, “High angle radiation of short electric waves,” *Proceedings of the Institute of Radio Engineers*, vol. 15, pp. 377–385, May 1927.
- [75] R. Harrington, “Reactively controlled directive arrays,” *IEEE Transactions on Antennas and Propagation*, vol. 26, pp. 390–395, May 1978.
- [76] H. Kawakami and T. Ohira, “Electrically steerable passive array radiator (ESPAR) antennas,” *IEEE Antennas and Propagation Magazine*, vol. 47, pp. 43–50, Apr. 2005.
- [77] D. Gesbert, M. Shafi, D. shan Shiu, P. J. Smith, and A. Naguib, “From theory to practice: an overview of MIMO space-time coded wireless systems,” *IEEE Journal on Selected Areas in Communications*, vol. 21, pp. 281–302, Apr 2003.
- [78] A. F. Molisch and M. Z. Win, “MIMO systems with antenna selection,” *IEEE Microwave Magazine*, vol. 5, pp. 46–56, Mar 2004.
- [79] A. YavanoÅşlu and . ErtuÅş, “On the capacity analysis of IEEE802.11n MIMO-OFDM WLAN systems using sub-optimal mimo detectors and compact space-

- multimode antenna arrays,” in *2011 3rd International Congress on Ultra Modern Telecommunications and Control Systems and Workshops (ICUMT)*, pp. 1–6, Oct. 2011.
- [80] Q. Li, X. E. Lin, J. Zhang, and W. Roh, “Advancement of MIMO technology in WiMAX: from IEEE 802.16d/e/j to 802.16m,” *IEEE Communications Magazine*, vol. 47, pp. 100–107, June 2009.
- [81] E. Kurniawan, A. S. Madhukumar, and F. Chin, “Performance Analysis of MIMO Enabled Broadband Wireless Access System for Mobile Multimedia Applications,” in *2005 5th International Conference on Information Communications Signal Processing*, pp. 941–945, 2005.
- [82] G. Liu, J. Zhang, P. Zhang, Y. Wang, X. Liu, and S. Li, “Evolution map from TD-SCDMA to FuTURE B3g TDD,” *IEEE Communications Magazine*, vol. 44, pp. 54–61, Mar. 2006.
- [83] K.-L. Wong, “Planar antennas for wireless communications,” *Microwave Journal*, vol. 46, no. 10, pp. 144–145, 2003.
- [84] K. L. Virga and Y. Rahmat-Samii, “Low-profile enhanced-bandwidth PIFA antennas for wireless communications packaging,” *IEEE Transactions on Microwave Theory and Techniques*, vol. 45, no. 10, pp. 1879–1888, 1997.
- [85] M. Abedin and M. Ali, “Modifying the ground plane and its effect on planar inverted-F antennas (PIFAs) for mobile phone handsets,” *IEEE Antennas and Wireless Propagation Letters*, vol. 2, no. 1, pp. 226–229, 2003.
- [86] C.-T. Lee and K.-L. Wong, “Uniplanar printed coupled-fed PIFA with a band-notching slit for WLAN/WiMAX operation in the laptop computer,” *IEEE Transactions on Antennas and Propagation*, vol. 57, no. 4, pp. 1252–1258, 2009.
- [87] M. Ali, G. J. Hayes, H.-S. Hwang, and R. A. Sadler, “Design of a multiband internal antenna for third generation mobile phone handsets,” *IEEE Transactions on Antennas and Propagation*, vol. 51, no. 7, pp. 1452–1461, 2003.
- [88] K. M. Shams and M. Ali, “Study and design of a capacitively coupled polymeric internal antenna,” *IEEE transactions on antennas and propagation*, vol. 53, no. 3, pp. 985–993, 2005.
- [89] L. Vallozzi, P. Van Torre, C. Hertleer, H. Rogier, M. Moeneclaey, and J. Ver-

- haevert, “Wireless Communication for Firefighters Using Dual-Polarized Textile Antennas Integrated in Their Garment,” *IEEE Transactions on Antennas and Propagation*, vol. 58, pp. 1357–1368, Apr. 2010.
- [90] K. K. Kishor and S. V. Hum, “A pattern reconfigurable chassis-mode mimo antenna,” *IEEE Transactions on Antennas and Propagation*, vol. 62, pp. 3290–3298, June 2014.
- [91] P. Y. Qin, Y. J. Guo, A. R. Weily, and C. H. Liang, “A pattern reconfigurable u-slot antenna and its applications in mimo systems,” *IEEE Transactions on Antennas and Propagation*, vol. 60, pp. 516–528, Feb 2012.
- [92] C. Rhee, Y. Kim, T. Park, S. s. Kwoun, B. Mun, B. Lee, and C. Jung, “Pattern-Reconfigurable MIMO Antenna for High Isolation and Low Correlation,” *IEEE Antennas and Wireless Propagation Letters*, vol. 13, pp. 1373–1376, 2014.
- [93] I. Khan, I. Ullah, and P. Hall, “Transmit-receive diversity for 2 x 2 multiple-input multiple-output channel in body area networks,” *IET microwaves, antennas & propagation*, vol. 5, no. 13, pp. 1589–1593, 2011.
- [94] M. Qaraqe, Q. H. Abbasi, A. Alomainy, and E. Serpedin, “Experimental Evaluation of MIMO Capacity for Ultrawideband Body-Centric Wireless Propagation Channels,” *IEEE Antennas and Wireless Propagation Letters*, vol. 13, pp. 495–498, 2014.
- [95] S. Shoaib, I. Shoaib, N. Shoaib, X. Chen, and C. G. Parini, “Design and performance study of a dual-element multiband printed monopole antenna array for MIMO terminals,” *IEEE Antennas and Wireless Propagation Letters*, vol. 13, pp. 329–332, 2014.
- [96] M. R. Islam and M. Ali, “Ground Current Modification of Mobile Terminal Antennas and Its Effects,” *IEEE Antennas and Wireless Propagation Letters*, vol. 10, pp. 438–441, 2011.
- [97] Y. Cui, R. Li, and P. Wang, “Novel Dual-Broadband Planar Antenna and Its Array for 2g/3g/LTE Base Stations,” *IEEE Transactions on Antennas and Propagation*, vol. 61, pp. 1132–1139, Mar. 2013.
- [98] Y. Liu, H. Yi, F.-W. Wang, and S.-X. Gong, “A Novel Miniaturized Broadband Dual-Polarized Dipole Antenna for Base Station,” *IEEE Antennas and Wireless Propagation Letters*, vol. 12, pp. 1335–1338, 2013.

- [99] M. V. Varnoosfaderani, D. V. Thiel, J. Lu, and M. Kanesan, "Dual mode switched parasitic antenna for on/off body communication channels," in *Antenna Technology: "Small Antennas, Novel EM Structures and Materials, and Applications" (iWAT), 2014 International Workshop on*, pp. 25–28, March 2014.
- [100] J. J. Luther, S. Ebadi, and X. Gong, "A microstrip patch electronically steerable parasitic array radiator (ESPAR) antenna with reactance-tuned coupling and maintained resonance," *IEEE Transactions on Antennas and Propagation*, vol. 60, no. 4, pp. 1803–1813, 2012.
- [101] M. R. Islam, N. H. Chamok, and M. Ali, "Switched Parasitic Dipole Antenna Array for High-Data-Rate Body-Worn Wireless Applications," *IEEE Antennas and Wireless Propagation Letters*, vol. 11, pp. 693–696, 2012.
- [102] M. R. Islam and M. Ali, "Body-wearable beam steering antenna array for 5.2 GHz WLAN applications," in *2012 7th International Conference on Electrical Computer Engineering (ICECE)*, pp. 447–449, Dec. 2012.
- [103] M. R. Islam and M. Ali, "A 900 MHz Beam Steering Parasitic Antenna Array for Wearable Wireless Applications," *IEEE Transactions on Antennas and Propagation*, vol. 61, pp. 4520–4527, Sept. 2013.
- [104] D. Anagnostou, G. Zheng, S. Barbin, M. Chryssomallis, J. Papapolymerou, and C. Christodoulou, "An X-band reconfigurable planar dipole antenna," in *2005 SBMO/IEEE MTT-S International Conference on Microwave and Optoelectronics*, pp. 654–656, July 2005.
- [105] J. Thaysen and K. B. Jakobsen, "Envelope correlation in (n, n) mimo antenna array from scattering parameters," *Microwave and optical technology letters*, vol. 48, no. 5, pp. 832–834, 2006.
- [106] S. Blanch, J. Romeu, and I. Corbella, "Exact representation of antenna system diversity performance from input parameter description," *Electronics letters*, vol. 39, no. 9, pp. 705–707, 2003.
- [107] C. Votis, G. Tatsis, and P. Kostarakis, "Envelope correlation parameter measurements in a mimo antenna array configuration," *International Journal of Communications, Network and System Sciences*, vol. 3, no. 4, p. 350, 2010.
- [108] P. S. Hall and Y. Hao, eds., *Antennas and propagation for body-centric wireless communications*. Artech House antennas and propagation series, Boston:

Artech House, 2nd ed ed., 2012.

- [109] J. W. S. Hearle and W. E. Morton, *Physical Properties of Textile Fibres*. Elsevier, Oct. 2008.
- [110] B. Gupta, S. Sankaralingam, and S. Dhar, “Development of wearable and implantable antennas in the last decade: A review,” in *2010 10th Mediterranean Microwave Symposium*, pp. 251–267, Aug. 2010.
- [111] “Flectron.” Available online: <http://www.lairdtech.com/product-categories/emi-shields-gaskets/metalized-conductive-fabrics>.
- [112] “Shielding and Conductive Fabrics.” Available online: <http://www.lessemf.com/fabric4.html>.
- [113] S. Sankaralingam and B. Gupta, “Determination of Dielectric Constant of Fabric Materials and Their Use as Substrates for Design and Development of Antennas for Wearable Applications,” *IEEE Transactions on Instrumentation and Measurement*, vol. 59, pp. 3122–3130, Dec. 2010.
- [114] D. M. Pozar, *Microwave engineering*. John Wiley & Sons, 2009.
- [115] E. Yablonovitch, “Inhibited Spontaneous Emission in Solid-State Physics and Electronics,” *Physical Review Letters*, vol. 58, pp. 2059–2062, May 1987.
- [116] S. John, “Strong localization of photons in certain disordered dielectric superlattices,” *Physical Review Letters*, vol. 58, pp. 2486–2489, June 1987.
- [117] K. M. Ho, C. T. Chan, and C. M. Soukoulis, “Existence of a photonic gap in periodic dielectric structures,” *Physical Review Letters*, vol. 65, pp. 3152–3155, Dec. 1990.
- [118] E. Yablonovitch, T. J. Gmitter, and K. M. Leung, “Photonic band structure: The face-centered-cubic case employing nonspherical atoms,” *Physical Review Letters*, vol. 67, pp. 2295–2298, Oct. 1991.
- [119] K. M. Ho, C. T. Chan, C. M. Soukoulis, R. Biswas, and M. Sigalas, “Photonic band gaps in three dimensions: New layer-by-layer periodic structures,” *Solid State Communications*, vol. 89, pp. 413–416, Feb. 1994.

- [120] E. ĀŪzbay, A. Abeyta, G. Tuttle, M. Tringides, R. Biswas, C. T. Chan, C. M. Soukoulis, and K. M. Ho, “Measurement of a three-dimensional photonic band gap in a crystal structure made of dielectric rods,” *Physical Review B*, vol. 50, pp. 1945–1948, July 1994.
- [121] P. S. Kildal, “Artificially soft and hard surfaces in electromagnetics,” *IEEE Transactions on Antennas and Propagation*, vol. 38, pp. 1537–1544, Oct. 1990.
- [122] D. Sievenpiper, *High-Impedance Electromagnetic Surfaces*. PhD Dissertation, University of California, Los Angeles, 1999.
- [123] D. Sievenpiper, L. Zhang, R. F. J. Broas, N. G. Alexopolous, and E. Yablonovitch, “High-impedance electromagnetic surfaces with a forbidden frequency band,” *IEEE Transactions on Microwave Theory and Techniques*, vol. 47, pp. 2059–2074, Nov. 1999.
- [124] F.-R. Yang, K.-P. Ma, Y. Qian, and T. Itoh, “A uniplanar compact photonic-bandgap (UC-PBG) structure and its applications for microwave circuit,” *IEEE Transactions on Microwave Theory and Techniques*, vol. 47, pp. 1509–1514, Aug. 1999.
- [125] F.-R. Yang, *Novel Periodic Structures for Applications to Microwave Circuits*. PhD Dissertation, University of California, Los Angeles, 2000.
- [126] A. DellaVilla, V. Galdi, F. Capolino, V. Pierro, S. Enoch, and G. Tayeb, “A Comparative Study of Representative Categories of EBG Dielectric Quasi-Crystals,” *IEEE Antennas and Wireless Propagation Letters*, vol. 5, pp. 331–334, Dec. 2006.
- [127] F. Yang and Y. Rahmat-Samii, *Electromagnetic band gap structures in antenna engineering*. Cambridge university press Cambridge, UK, 2009.
- [128] M. Veysi, M. Kamyab, S. M. Mousavi, and A. Jafargholi, “Wideband Miniaturized Polarization-Dependent HIS Incorporating Metamaterials,” *IEEE Antennas and Wireless Propagation Letters*, vol. 9, pp. 764–766, 2010.
- [129] J. McVay, N. Engheta, and A. Hoorfar, “High impedance metamaterial surfaces using Hilbert-curve inclusions,” *IEEE Microwave and Wireless Components Letters*, vol. 14, pp. 130–132, Mar. 2004.
- [130] S. Clavijo, R. E. Diaz, and W. E. McKinzie, “Design methodology for Sieven-

- piper high-impedance surfaces: an artificial magnetic conductor for positive gain electrically small antennas,” *IEEE Transactions on Antennas and Propagation*, vol. 51, pp. 2678–2690, Oct. 2003.
- [131] O. Luukkonen, M. G. Silveirinha, A. B. Yakovlev, C. R. Simovski, I. S. Nefedov, and S. A. Tretyakov, “Effects of Spatial Dispersion on Reflection From Mushroom-Type Artificial Impedance Surfaces,” *IEEE Transactions on Microwave Theory and Techniques*, vol. 57, pp. 2692–2699, Nov. 2009.
- [132] R. Coccioli, F.-R. Yang, K.-P. Ma, and T. Itoh, “Aperture-coupled patch antenna on UC-PBG substrate,” *IEEE Transactions on Microwave Theory and Techniques*, vol. 47, pp. 2123–2130, Nov. 1999.
- [133] J. S. Colburn and Y. Rahmat-Samii, “Patch antennas on externally perforated high dielectric constant substrates,” *IEEE Transactions on Antennas and Propagation*, vol. 47, pp. 1785–1794, Dec. 1999.
- [134] R. Gonzalo, P. D. Maagt, and M. Sorolla, “Enhanced patch-antenna performance by suppressing surface waves using photonic-bandgap substrates,” *IEEE Transactions on Microwave Theory and Techniques*, vol. 47, pp. 2131–2138, Nov. 1999.
- [135] R. F. J. Broas, D. F. Sievenpiper, and E. Yablonovitch, “A high-impedance ground plane applied to a cellphone handset geometry,” *IEEE Transactions on Microwave Theory and Techniques*, vol. 49, pp. 1262–1265, July 2001.
- [136] S. K. Sharma and L. Shafai, “Enhanced performance of an aperture-coupled rectangular microstrip antenna on a simplified unipolar compact photonic band gap (UC-PBG) structure,” in *IEEE Antennas and Propagation Society International Symposium, 2001*, vol. 2, pp. 498–501 vol.2, July 2001.
- [137] F. Yang and Y. Rahmat-Samii, “Microstrip antennas integrated with electromagnetic band-gap (EBG) structures: a low mutual coupling design for array applications,” *IEEE Transactions on Antennas and Propagation*, vol. 51, pp. 2936–2946, Oct. 2003.
- [138] D. Pavlickovski and R. B. Waterhouse, “Shorted microstrip antenna on a photonic bandgap substrate,” *IEEE Transactions on Antennas and Propagation*, vol. 51, pp. 2472–2475, Sept. 2003.
- [139] J. Liang and H. Y. D. Yang, “Microstrip Patch Antennas on Tunable Electro-

- magnetic Band-Gap Substrates,” *IEEE Transactions on Antennas and Propagation*, vol. 57, pp. 1612–1617, June 2009.
- [140] J. Y. Park, C. C. Chang, Y. Qian, and T. Itoh, “An improved low-profile cavity-backed slot antenna loaded with 2d UC-PBG reflector,” in *IEEE Antennas and Propagation Society International Symposium, 2001*, vol. 4, pp. 194–197 vol.4, July 2001.
- [141] A. Neto, N. Llombart, G. Gerini, and P. D. Maagt, “On the optimal radiation bandwidth of printed slot antennas surrounded by EBGs,” *IEEE Transactions on Antennas and Propagation*, vol. 54, pp. 1074–1083, Apr. 2006.
- [142] F. Yang and Y. Rahmat-Samii, “A low-profile circularly polarized curl antenna over an electromagnetic bandgap (EBG) surface,” *Microwave and Optical Technology Letters*, vol. 31, pp. 264–267, Nov. 2001.
- [143] J. M. Bell and M. F. Iskander, “A low-profile Archimedean spiral antenna using an EBG ground plane,” *IEEE Antennas and Wireless Propagation Letters*, vol. 3, pp. 223–226, Dec. 2004.
- [144] F. Erkmen, C. C. Chen, and J. L. Volakis, “UWB magneto-dielectric ground plane for low-profile antenna applications,” *IEEE Antennas and Propagation Magazine*, vol. 50, pp. 211–216, Aug. 2008.
- [145] H. Nakano, K. Kikkawa, N. Kondo, Y. Iitsuka, and J. Yamauchi, “Low-Profile Equiangular Spiral Antenna Backed by an EBG Reflector,” *IEEE Transactions on Antennas and Propagation*, vol. 57, pp. 1309–1318, May 2009.
- [146] Z. Li and Y. Rahmat-Samii, “PBG, PMC and PEC ground planes: a case study of dipole antennas,” in *IEEE Antennas and Propagation Society International Symposium, 2000*, vol. 2, pp. 674–677 vol.2, July 2000.
- [147] R. C. Hansen, “Effects of a high-impedance screen on a dipole antenna,” *IEEE Antennas and Wireless Propagation Letters*, vol. 1, no. 1, pp. 46–49, 2002.
- [148] F. Yang and Y. Rahmat-Samii, “Reflection phase characterizations of the EBG ground plane for low profile wire antenna applications,” *IEEE Transactions on Antennas and Propagation*, vol. 51, pp. 2691–2703, Oct. 2003.
- [149] M. F. Abedin and M. Ali, “Application of EBG substrates to design ultra-thin wideband directional dipoles,” in *IEEE Antennas and Propagation Society*

International Symposium, 2004, vol. 2, pp. 2071–2074 Vol.2, June 2004.

- [150] M. F. Abedin and M. Ali, “Designing ultra-thin printed dipole arrays based on EBG reflection phase profile,” in *The 2005 IEEE Annual Conference Wireless and Microwave Technology, 2005.*, pp. 20–20, Apr. 2005.
- [151] M. F. Abedin and M. Ali, “Effects of a smaller unit cell planar EBG structure on the mutual coupling of a printed dipole array,” *IEEE Antennas and Wireless Propagation Letters*, vol. 4, pp. 274–276, 2005.
- [152] M. F. Abedin and M. Ali, “Effects of EBG reflection phase profiles on the input impedance and bandwidth of ultrathin directional dipoles,” *IEEE Transactions on Antennas and Propagation*, vol. 53, pp. 3664–3672, Nov. 2005.
- [153] L. Akhoondzadeh-Asl and P. S. Hall, “Wideband dipoles on electromagnetic bandgap ground planes,” in *Wideband and Multi-band Antennas and Arrays, 2005. IEE (Ref. No. 2005/11059)*, pp. 41–45, Sept. 2005.
- [154] M. F. Abedin, M. Z. Azad, and M. Ali, “Wideband Smaller Unit-Cell Planar EBG Structures and Their Application,” *IEEE Transactions on Antennas and Propagation*, vol. 56, pp. 903–908, Mar. 2008.
- [155] M. Z. Azad and M. Ali, “Novel Wideband Directional Dipole Antenna on a Mushroom Like EBG Structure,” *IEEE Transactions on Antennas and Propagation*, vol. 56, pp. 1242–1250, May 2008.
- [156] S. R. Best and D. L. Hanna, “Design of a broadband dipole in close proximity to an EBG ground plane,” *IEEE Antennas and Propagation Magazine*, vol. 50, pp. 52–64, Dec. 2008.
- [157] Sanchez, Victor C. and III, William E. McKinzie and Diaz, Rodolfo E., “Broadband antennas over electronically reconfigurable artificial magnetic conductor surfaces,” *US Patent 6917343 B2*, 2005.
- [158] F. Costa, A. Monorchio, S. Talarico, and F. M. Valeri, “An Active High-Impedance Surface for Low-Profile Tunable and Steerable Antennas,” *IEEE Antennas and Wireless Propagation Letters*, vol. 7, pp. 676–680, 2008.
- [159] D. Cure, T. M. Weller, and F. A. Miranda, “Study of a Low-Profile 2.4-GHz Planar Dipole Antenna Using a High-Impedance Surface With 1-D Varactor Tuning,” *IEEE Transactions on Antennas and Propagation*, vol. 61, pp. 506–

515, Feb. 2013.

- [160] A. I. Zaghoul, S. Palreddy, and S. J. Weiss, “A concept for a broadband electromagnetic band gap (EBG) structure,” in *Proceedings of the 5th European Conference on Antennas and Propagation (EUCAP)*, pp. 383–387, Apr. 2011.
- [161] L. Li, B. Li, H.-X. Liu, and C.-H. Liang, “Locally resonant cavity cell model for electromagnetic band gap structures,” *IEEE Transactions on Antennas and Propagation*, vol. 54, pp. 90–100, Jan. 2006.
- [162] R. Afzalzadeh, “Dielectric constant measurements of finite-size sheet at microwave frequencies by pseudo-Brewster’s angle method,” *IEEE Transactions on Microwave Theory and Techniques*, vol. 46, pp. 1307–1309, Sept. 1998.
- [163] H. H. Xie, Y. C. Jiao, S. M. Ning, and Y. Song, “A pattern-reconfigurable Yagi antenna based on EBG ground plane,” in *2010 International Symposium on Signals, Systems and Electronics*, vol. 2, pp. 1–3, Sept. 2010.
- [164] C. Toker, M. Saglam, M. Ozme, and N. Gunalp, “Branch-line couplers using unequal line lengths,” *IEEE Transactions on Microwave Theory and Techniques*, vol. 49, pp. 718–721, Apr. 2001.